1980

Behavior of composite steel deck diaphragms

James E. Bolluyt
Iowa State University

Behavior of composite steel deck diaphragms

by

James Edward Bolluyt

A Thesis Submitted to the

Graduate Faculty in Partial Fulfillment of the

Requirements for the Degree of

MASTER OF SCIENCE

Department: Civil Engineering
Major: Structural Engineering

Approved:

_____

_____
In Charge of Major Work

_____
For the Major Department

_____
For the Graduate College

Iowa State University
Ames, Iowa

1980

TABLE OF CONTENTS

LIST OF TABLES

LIST OF FIGURES

LIST OF SYMBOLS

a	Length of the diaphragm
a'	Effective width of the edge zone perpendicular to the corrugations
A_s	Area of the steel deck, $in.^2$
b	Width of the diaphragm or width of the pushout specimen or plate
b'	Effective width of the edge zone parallel to the corrugations
b_b	Average measured width, in.
c	Concrete cover above the up corrugation, in.
C_{st}	Internal compressive force due to the stud load, KIPs
d	Distance from the extreme compressive fiber to the centroid of the longitudinal tension reinforcement, in.
d_a	Effective weld diameter of an arc spot weld, in.
D_{avg}	Average composite depth, in.
e	Eccentricity between applied and resisting stress resultants, in.
E_c	Modulus of elasticity of the concrete, ksi
E_s	Modulus of elasticity of steel, ksi
f'_c	Compressive strength of the concrete, psi
f_{crs}	Shear stress in a flat plate at buckling
f_t	Tensile stress in the concrete
f_y	Yield strength of the steel, ksi
F_i	Component force on an edge connector
G_c	Shear stiffness of the concrete, ksi
G_s	Shear stiffness of steel, ksi
h	Effective thickness of the concrete ($=t_e$), in.

I_c Moment of inertia of the composite web, $in.^4$

I_s Moment of inertia of the framing beams, $in.^4$

k_p Linear stiffness of the edge zone parallel to the corrugations, KIPs/in./in.

k_p' Linear stiffness perpendicular to the corrugations corresponding to q_p', KIPs/in./in.

k_s Buckling shear coefficient for flat plate

k_t Linear stiffness of the edge zone perpendicular to the corrugations, KIPs/in./in.

k_t' Linear stiffness parallel to the corrugations corresponding to q_t', KIPs/in./in.

K Measured initial stiffness of the diaphragm, KIPs/in.

K_b Bending stiffness of the diaphragm, KIPs/in.

K_s Shear stiffness of the diaphragm, KIPs/in.

K_T Total calculated diaphragm stiffness, KIPs/in.

K_Z Diaphragm stiffness due to the deformation of the edge zone, KIPs/in.

ℓ_c Length of edge zone contributing to force on stud(s)

ℓ_p $(b^2 + 3bb' - 2b'^2)/6a$

ℓ_p' $(b^2 + 4bb' - 4b'^2)/4a$

ℓ_t $a' - (2a'^2/3a)$

ℓ_t' $2a' - (2a'^2/a)$

L Out-to-out length, in.

L' Shear span, in.

M_u Ultimate moment, in.-KIPs

n Modular ratio of elasticity $(= E_s/E_c)$

n_a Number of edge connectors along length a

n_a' Number of edge connectors along length a'

n_b Number of edge connectors along length b

n_c Number of edge connectors along length ℓ_c

n_s Modular ratio of rigidity (= G_s/G_c)

p Arc spot weld capacity, KIPs

P Total force applied to the diaphragm, KIPs

P_{sb} Shear-bond load contribution, KIPs

P_{st} Stud load contribution, KIPs

P_u Maximum total shear force applied to the diaphragm, or ultimate recorded vertical load, KIPs

q_p Interfacial shear force parallel to the corrugations, KIPs/ft

q'_p q_p force that occurs along edges perpendicular to corrugations, KIPs/ft

q_t Interfacial shear force perpendicular to the corrugations, KIPs/ft

q'_t q_t force that occurs along edges parallel to corrugations, KIPs/ft

Q Calculated stud load, KIPs

Q_p Ultimate strength value of q_p, KIPs/ft

Q'_p Ultimate strength value of q'_p, KIPs/ft

Q_t Ultimate strength value of q_t, KIPs/ft

Q'_t Ultimate strength value of q'_t, KIPs/ft

Q_u Ultimate connector strength, KIPs

Q_{up} Ultimate strength of a stud shear connector with the deck parallel to the edge member, KIPs

Q_{ut} Ultimate strength of a stud shear connector with the deck perpendicular to the edge member, KIPs

t_a Average thickness of the concrete, in.

t_e Effective thickness of the diaphragm (= $t_a + n_s t_s$), in.

t_n	Net thickness of the steel deck, in.
t_s	Thickness of the steel deck, in.
V	Applied shear force on the slab (= P), KIPs
V_{corr}	Shear strength with shoring correction, KIPs
V_i	Shear force at embossment i, KIPs
V_u	Ultimate shear force, KIPs
$V_{u_{LL}}$	Ultimate shear strength due to live load, KIPs
x_o	Point of zero embossment shear force, in.
x_u	Point where embossment shear force is at ultimate, in.
y_{sb}	Distance from deck centroid to bottom of deck, in.
α	Slope of regression line
β	Intercept of regression line
δ	Relative displacement at deck-to-concrete interface, in.
δ_{sb}	Shear-bond end-slip, in.
δ_{st}	Stud end-slip, in.
δ_{u_i}	Relative displacement corresponding to ultimate shear capacity, embossment i, in.
Δ_{actual}	Actual displacement of diaphragm, in.
Δ_b	Net bending deflection of the diaphragm, in.
Δ_{max}	Maximum diaphragm displacement at a specified yield load, in.
$\Delta_{nominal}$	Nominal displacement of diaphragm, in.
Δ_p	Edge zone displacement in the longitudinal direction, in.
Δ_s	Net shear deflection of the diaphragm, in.
Δ_t	Edge zone displacement in the transverse direction, in.
Δ_y	Diaphragm displacement corresponding to yield load, in.
Δ_z	Net deflection of the diaphragm due to deformation of the edge zone, in.

Δ_T	Total diaphragm deflection, in.
θ	Rotation of the concrete about the center point of the diaphragm
μ	Coefficient of friction between the steel deck and concrete
ρ	Percentage steel content
σ_{ult}	Ultimate stress capacity of steel
ω	Composite slab dead weight, psi

PREFACE

The investigation of the behavior of composite steel deck diaphragms which is described herein was sponsored by the National Science Foundation, Grant No. ENV75-23625. Guidance was provided by a National Science Foundation Advisory Panel.

This investigation was administered through the Engineering Research Institute of Iowa State University. Dr. M. L. Porter served as principal investigator. Drs. L. F. Greimann and C. E. Ekberg, Jr., served as co-investigator and principal consultant, respectively.

V. E. Arnold, research assistant, and G. L. Krupicka, lab technician and research assistant, were primarily responsible for the design and construction of the full-scale test facility. V. E. Arnold was also responsible for the first two full-scale tests (Slabs 1 and 2) and associated data summarized herein, and G. L. Krupika for the vertical load tests and analysis summarized in Appendix A. D, J. Brangwin, research assistant, was responsible for the construction and testing of Slabs 3 through 6, the second series of pushout tests summarized in Appendix B, and the initial work on analyzing and predicting the interfacial shear mode of failure. This author, serving as research assistant, was primarily responsible for the construction and testing of Slabs 7, 8, and 9 and the third series of pushout tests discussed in Appendix B. The author was also responsible for the revision and additional development of the proposed predictive equations and their application to Slabs 1 through 9. D. L. Wood, lab technician, assisted in summarizing much of the written material and data for Slabs 1 through 6, in the preparation of Specimen

Slabs 7, 8, and 9, and in the testing of the pushout specimens. R. H. Day assisted in the horizontal pushout specimens discussed in Appendix A. Aziz Sabri was responsible for the finite element analysis discussed in Section 4.

1. INTRODUCTION

1.1. General

In the past 10-15 years, cold-formed, metal deck, composite floor slab systems have become increasingly more popular. This type of floor system not only saves on the cost of form work and shoring, but also reduces field labor costs and permits a minimum floor thickness, which increases material savings. The form work is provided by the steel deck and, after the concrete is poured and cured on top of the deck, the two materials act together as a composite structural system, with the steel deck providing the principal positive bending tension reinforcement. Enclosing the cells on the bottom of the steel deck (in which case the section is called cellular deck) will also provide passageways for electrical wiring, heating and air conditioning ducts, as well as other utilities. Figure 1* shows a typical composite floor system.

The interlocking mechanism between the steel and concrete is provided by mechanical devices such as embossments and/or indentations, holes located in the steel deck, transverse wires attached to the deck, and the chemical bonding of the concrete to the steel surface. This composite slab is connected to the support beams by means of arc spot welds or shear connectors, such as studs, welded through the deck to the beam. If shear connectors are used, composite action is also developed between the slab and support beams.

---

*The figures are grouped together at the end of this report in Section 11.

A floor slab system designed to resist in-plane forces, along with the vertical live and dead loads, is referred to as a diaphragm. In-plane forces result from lateral loads as typically produced by earthquakes and/or wind. These lateral forces are transferred through the diaphragm into the vertical shear-resisting elements of the structure, and finally into the foundation as horizontal shear. The distribution of these loads throughout a structure depends on the diaphragm's stiffness and ultimate strength.

1.2. Failure Modes

Table 1* lists potential failure modes for composite steel deck diaphragms subjected to in-plane shear. This list is based on a literature survey of research done by A. H. Nilson and A. A. Ammar [1-5], L. D. Luttrell [6-7], T. V. Apparao [8], C. W. Pinkham,† M. L. Porter and C. E. Eckberg [9-15], as well as the test results from this project. The major parameters involved in these failure modes are shear connections (arc spot welds, studs), concrete qualities (strength, depth), diaphragm configuration (orientation, plan dimensions, and thickness) and loading history (cyclic and monotonic). To clearly understand the relative importance of these parameters and to arrive at possible design criteria, the failure modes must be studied and understood.

---

*The tables can be found in Section 10 of this report.

†C. W. Pinkham, S. B. Barnes and Associates, Los Angeles, California. Personal visit to Iowa State University, April 7, 1977.

1.2.1. Composite Diaphragm Failures

Composite diaphragm failures occur when, at the time of maximum load, the system acts as a composite unit. A diagonal tension failure (Failure Mode 1a-1 in Table 1) is an example of this type of failure. This failure mode occurs when the concrete stress reaches its tensile limit and is characterized by diagonal cracks (at an approximate 45^{o} angle) across the slab (Fig. 2). After this crack forms, the steel deck begins to act as shear reinforcement, transferring the forces across the crack.

Another type of composite diaphragm failure is a direct shearing of the concrete along a line parallel to the deck corrugations (Failure Mode 1a-2). If the concrete covering is thin, this will most likely occur over an up corrugation with the ultimate strength depending on the shear strength of the concrete.

Two other failure modes, stability and localized (Failure Modes 1b and 1c), are also possible. A stability failure is typical for metal deck diaphragms with large width-to-thickness ratios. However, in composite diaphragms, the concrete effectively prevents out-of-plane buckling for in-plane loads. All of the tests presented in this report consist of composite diaphragms of moderate span lengths with only in-plane loading, so the stability failure mode did not occur. Combined in-plane and vertical (gravity) loading may necessitate a consideration of this failure mode. A localized failure would occur when there is a nonuniform shear distribution in the diaphragm and, consequently, discrete regions of high stress. This failure is restricted to a

small area and created by concentrated loads or reactions and/or flexible edge beams.

1.2.2. Deck/Concrete Interface

If the composite deck does not make use of shear connectors (e.g., studs), all of the diaphragm force must be transferred to the concrete by forces at the interface between the steel deck and concrete, i.e., by interfacial shear forces. Failure by interfacial shear (Failure Mode 2) can occur either parallel or perpendicular to the deck corrugations. Interfacial shear failure parallel to the corrugations (Failure Mode 2a) is similar in character to the shear-bond failure experienced in vertically loaded specimens [14] (see Appendix A).

When failure occurs in the direction perpendicular to the steel deck corrugations, the concrete bears against the inclined face of the cell. Two types of behavior may occur. If the corrugations are stiff enough, the concrete may actually ride up and over them (Failure Mode 2b-1). If they are flexible, the concrete will flatten out the corrugations, a type of behavior comparable to that of a horizontally loaded simple frame (Failure Mode 2b-2). Which mode occurs is dependent upon the stiffness of the deck corrugations and the relative interfacial shear strength in both the transverse and longitudinal directions.

1.2.3. Diaphragm/Edge Member Interface

Edge connections are frequently made with arc spot welds or studs. With the arc spot welds, the load is transferred through the steel deck. Failure at these points could be a direct shearing of the weld (Failure Mode 3a-1), or a buckling and/or tearing of the deck around

the weld (Failure Mode 3a-2). With arc spot welds or short studs that do not extend above the up corrugation, a direct shearing of the concrete rib, resembling an unreinforced corbel, could occur (Failure Mode 3b).

With studs that extend above the up corrugation of the steel deck, the shear force is transferred directly into the concrete above the deck profile. Failure of this form of connection may be a result of stud shear (Failure Mode 3c-1) or concrete failure around the stud (Failure Mode 3c-2). This second form is usually the result of an inadequate amount of concrete in the down corrugation and/or at the edges.

1.3. Objective

The objective of this research is to determine the behavioral and strength characteristics of composite steel deck floor slab diaphragms. Principal characteristics to be investigated include maximum load, ductility, stiffness, and failure mode.

The entire research program is divided into six phases as follows.

1. Designing a full-scale research facility for in-plane loading of composite slab diaphragms and conducting two pilot tests.
2. Testing of full-scale composite slabs with in-plane loading only.
3. Testing of one-way slab elements with vertical loads to determine the influence of stud shear connectors on shear-bond strength.

4. Developing an analytical model using finite-element analyses and determining the pertinent parameters to be used in design equations.
5. Testing of full-scale composite slabs with in-plane and vertical (gravity) loading.
6. Studying the effects that neighboring slab panels have on the continuity of the system.

The first three phases have been completed and are summarized in this report. Phase 4 is in its initial stages. A preliminary study of Phase 5 has been made with the hope that research will continue in this direction. The way in which Phase 6 will be incorporated in future study will depend upon the results of the first five phases.

2. EXPERIMENTAL TESTING AND SETUP

2.1. Test Specimens

Slabs 1-9 were all nominal 15-ft^2 composite steel deck diaphragms. Centerline-to-centerline distances between the framing beams were 15 ft, while the actual out-to-out dimensions of the concrete slab were 15 ft 4 in. × 15 ft 4 in. Slabs 1-4 and 7-9 used five nominal 36 in. × 15 ft 4 in. steel deck panels. Slabs 5 and 6 used six nominal 30 in. × 15 ft 4 in. panels. The composite slab was attached to the test frame by one of two methods: 1) by studs measuring a nominal 3/4 in. × 4 1/2 in. after burnoff, or 2) by arc spot welds, 3/4-in. in diameter, using class E-60s-3 or E-70s-3 (Ms-21G) welding wire. The deck panels were attached to each other by 1/8 in. × 1 1/2 in. seam welds, spaced 30 in. on center using 3/32-in. E7018 electrodes. The concrete was purchased from a local ready-mix plant. During casting, the concrete was compacted with an electric vibrator, covered with wet burlap under a plastic cover, and wet cured for 7-14 days.

Slabs 1 and 2 were pilot tests. They were constructed using 20-gage, 3-in. deep, embossed composite-type steel deck (Deck Type 1, see Fig. 3) stud welded to the test frame (Fig. 4). The number of studs used in these pilot tests was purposely selected as approximately twice the amount required to develop full slab strength for two reasons:

- To check the test frame behavior, especially the supports, by producing a large force.
- To achieve a failure mode involving the composite slab (Failure Mode 1 in Table 1) rather than a failure at the edge connection.

Arc spot welds were used as edge connections for Slabs 3-7 and 9. For Slabs 3, 4, 6, 7, and 9, 240 of these welds were distributed around the perimeter, and for Slab 5, approximately 120 welds were used (see Figs. 5-7). For Slab 8, 20 stud shear connectors were distributed around the perimeter as shown in Fig. 8. The same kind of deck, Deck Type 1, was used for Slabs 3, 4, and 8 as was used for Slabs 1 and 2. A 16-gage, 1 1/2-in. deep, steel deck (Deck Type 2) was used for Slabs 5 and 6 (see Fig. 9). The deck used for Slab 7, Deck Type 3, had the same profile as Deck Type 1 (Fig. 3) but was 16-gage instead of 20-gage. Slab 9 was the only one of the slabs constructed using a cellular deck, Deck Type 4. This deck type consisted of a fluted portion like Deck Type 3 welded to a 16-gage flat sheet. Table 2 gives a summary of test parameters for Slabs 1-9.

2.2. Test Facility

A preliminary choice of a test frame was made by reviewing former tests and by qualitatively comparing new test frame configurations. To compare the relative frame stiffnesses, load capacities, boundary conditions and diaphragm stress distributions of the proposed frame arrangements, a linear finite-element analysis computer program, SAP IV, was used to analyze the proposed frame arrangements [16].

A cantilever diaphragm test frame with a fixed edge was chosen as the final design. The fixed edge of the diaphragm models an attachment of the slab to a very stiff adjoining panel. In most buildings using composite floor systems, an adjacent slab exists on at least one side,

which provides in-plane restraint against deformation. Also, the fixed edge approximately models a continuously attached shear wall. The free edge would model a structural steel frame in which the in-plane forces are transferred into the diaphragm along the horizontal member. Stiff edge beams were used because they produce a more uniform shear stress distribution in the test diaphragm than do flexible support beams.

2.2.1. Test Frame

The test frame facility consisted of three large reinforced concrete reaction blocks (for the fixed edge), two hydraulic cylinder loading devices with supports (on the free edge), and three perimeter framing beams (see Fig. 10). The frame was designed with a working load of ±400 KIPs and a displacement capability of ±6 in.

The three large reinforced concrete reaction blocks were used to support one edge of the diaphragm. An embedded steel plate, simulating a rigid beam flange, was used to attach the steel deck to the concrete blocks. The blocks were anchored to the laboratory floor with 2-in. diameter high-strength bolts, each post-tensioned to 240 KIPs.

The edge beams for the test frame were made from 24 × 76 wide-flange (W) steel beams. Web stiffeners were added to prevent the top flange from rotating during large displacements. Friction-type bolted connections were used to join the framing beams together. These bolted connections consisted of flexible "T"-shaped elements instead of pins or hinges. The flexible "T" connections provided a constant "frictional" restraint during testing.

Two hydraulic double-acting cylinders were used to apply the force to the test frame. These actuators were front-trunnion mounted and

capable of pushing or pulling 200 KIPs each, giving the total test frame a 400 KIP capacity. The force was directly measured by a specially fabricated 200-KIP load cell attached in series to the cylinder rod shaft. Pressure gages located at the cylinder ports were used as an indirect measure of the load and served as a visual aid during testing.

2.2.2. Test Instrumentation--Typical

A schematic layout of the servo-hydraulic control system, test instrumentation, and data acquisition system (DAS) is shown in Fig. 11. The instrumentation was designed to measure applied loads, in-plane displacements, out-of-plane (vertical) displacements, concrete strains, steel deck strains, relative slips between concrete and steel deck, and strains in the perimeter framing beams. Crack histories were recorded by photographs of crack markings directly on the slab, and by a tape recorder.

2.2.2.1. Load Cells

Axial load cells of 200 KIP capacity were connected in series with each of the hydraulic cylinder rods. The load cells were designed and fabricated from 3 1/2-in. diameter aluminum rods and instrumented with a complete strain gage bridge consisting of two longitudinal and two transverse gages. This assembly was calibrated in the laboratory 400-KIP Satec test machine.

2.2.2.2. Displacements

Electrical direct current differential transducers (DCDT's) and mechanical dial gages were used to measure in-plane (horizontal) and out-of-plane (vertical) displacements (Figs. 12 and 13). Two DCDT's

located at the ends of the main loading beam were used to measure the primary deformation of the diaphragm (in-plane movement). The signal output from the DCDT located at the northeast corner of the slab was used as the displacement control feedback to the MTS servo-controller on all tests.

2.2.2.3. Concrete and Steel Deck Strains

A combination of single- and three-gage rosette strain gages was used to measure the strains on the steel deck and concrete surfaces (see Fig. 14). For all but Slabs 1 and 2, the gages on the outside surface of the steel deck had a mirror image on the inside surface so that the in-plane forces in the steel deck could be isolated.

There were three different types of gages used to measure concrete strains. Two types measured surface strains while the third measured internal strains. First, single- and three-gage rosette concrete strain gages were placed directly on the concrete surface above the steel deck strain gages. Second, to measure large strains in the concrete after cracking, clip gages were also mounted to the surface. The third type of strain gage used was an embedment gage. They also were positioned above the steel deck gages. The various positions of these gages on individual slabs will be discussed later in Section 2.2.3.

2.2.2.4. Concrete Slip Relative to Steel Deck

Slip gages and mechanical dial gages were used to measure the slip (in a direction parallel to the deck corrugations) between the steel deck and the concrete. On the north and south sides of Slabs 1, 2, and 3 the slip gages were attached in pairs, one from the edge beam to the

concrete and the other one from the edge beam to the deck (located on a down corrugation). This same setup was used on the east and west edges of Slab 4. The net slippage between the deck and concrete was determined by subtracting the readings of each pair. Slippage transverse to the deck corrugations was measured by four slip gages mounted from the framing beams to the concrete at the four corners.

Mechanical dial gages were also used to measure concrete slippage. The dial gages were mounted on either a rod embedded in the concrete with the stem resting on a steel block attached to the steel deck, or on a rod attached to the framing beam with the stem resting on the concrete. Typical positions of these gages are illustrated in Fig. 15.

2.2.2.5. Photographs

The top of the concrete slab was painted white and marked with a rectangular grid system. Cracks were marked with black markers. Pictures were taken from a camera mounted approximately 30 ft above the slab to qualitatively detect surface deformation and to record crack propagation and failure history. Close-up photographs were also taken of the steel deck deformations, slab cracking, and local failure zones throughout the test.

2.2.2.6. Data Collection

A 100-channel data acquisition system (DAS) was used to record strain gage and DCDT signals at various load points throughout the test. A teletype was used to print the data on paper and to record the data on paper-punch tape. Dial gage readings were recorded manually and later punched onto computer cards. These data were later reduced on a digital

computer. Digital voltmeters provided a continuous display of the loads and displacements.

2.2.2.7. Closed-Loop Control

Displacements during the test were controlled by an MTS closed-loop control system. The feedback signal was taken from DCDT 8 located in the northeast corner (Fig. 12). A servo-valve, which controlled the hydraulic actuators, was used to complete the loop. Diaphragm displacements were controlled by manually operating the set point on the MTS servo-controller. The gain in the signal from the DCDT 8 was selected such that ±1-in. displacement gave a ±10 volt (d.c.) signal and loop stability was within 0.001 in. An electrically operated four-way valve was installed as a backup hydraulic control unit. Flow check and control valves were incorporated into the backup unit to regulate the flow rate of the hydraulic fluid.

2.2.3. Test Instrumentation--Specific

Figures 14 and 15 show typical locations of strain and slip instrumentation for the slabs. Locations remained essentially the same with slight modifications made as data from the preceding slabs were accumulated.

Slabs 1 and 2 (pilot tests) used rosettes uniformally placed on the east half of the slab on both the deck and concrete. The strain gages on the deck were positioned directly below those on the concrete. Clip-gage rosettes (on the concrete surface) were located in the four corners of each specimen to measure gross concrete strains over a large area. Slip gages were also positioned around the slab to detect slip

parallel and perpendicular to the corrugations. Dial gages and DCDT's were used to measure the vertical or out-of-plane deflections. For Slabs 3 and 4, the locations of the strain gages remained the same, but gages were placed on both sides of the deck directly opposite each other (see Section 2.2.2.3). Half of the rosettes were replaced by uniaxial gages to allow enough DAS channels for the addition of the inside surface gages. The concrete gages were all uniaxial except for a rosette in the center. The clip gages were changed from rosettes to uniaxial oriented at 45^{o} with respect to the edges of the slab. A combination of clip and dial gages was used to measure the in-plane displacements. Dial gages and DCDT's were used to measure out-of-plane displacements. For Slabs 5 and 6 a rosette strain gage was added in the southwest corner (Fig. 14).

Clip gages were not used on the surface of the concrete for Slabs 7, 8, or 9. Both rosette and uniaxial gages were used on the surface of the concrete for Slab 7, but only rosettes were used on Slabs 8 and 9 (Fig. 14). In addition, concrete embedment gages were used for Slabs 7 and 8 to indicate the strain distribution through the cross section of the slab at selected locations (see Figs. 14 and 16). For Slab 8, slip and dial gages were used to measure the movement of the concrete near each stud with respect to each framing member (and presumably, therefore, the stud deformation) in two perpendicular directions (parallel and transverse to the corrugations).

2.3. Load Program

For each slab, a test program was established from the anticipated working and maximum loads and the estimated displacements. The program was monitored by displacement control, which was held constant at various increments while instrumentation readings were being recorded, cracks marked and labeled, and photographs taken. A load point (LP) was assigned to each displacement increment where readings were taken. A typical test program is shown in Fig. 17. Data readings were taken at each load point up to a maximum of ±1 in. At this time all vertical displacement DCDT's, slip gages, and dial gages were removed from the slab. The loading cycle was subsequently continued to ±5 in. in order to observe the complete failure breakdown of the composite slab.

A comparison of the results from Slabs 1 and 2 was used to determine which type of loading program, cyclic or monotonic, was best suited for this study. A cyclic loading program with progressively increasing displacement limits was selected for the remaining tests (Slabs 3-9). The cyclic loading program was considered more severe. Strength and stiffness of the slabs deteriorated after each loading reversal in the nonlinear range.

The initial cyclic limit was selected at a displacement in the working load range of the slab. The limits were approximately doubled until a 1-in. displacement was achieved. At each displacement limit a minimum of three complete displacement cycle reversals were taken. After a third cycle, if the load did not reach 95% of the previous cycle's load, additional cycles were taken at this displacement limit

until the system had stabilized, after which the test proceeded to the next displacement limit. Two extra cycles were the most ever required for any of the slabs.

3. EXPERIMENTAL RESULTS

3.1. General Behavior and Failure Modes

3.1.1. Slab 1

The test program for Slab 1 consisted of three initial loading reversals at ±40 KIPs, followed by a monotonic load increase to the maximum. Following maximum load, the slab was further displaced into the nonlinear region to investigate the strength, ductility, failure mode, and degradation of the system. After achieving maximum displacement, the slab was unloaded and again subjected to load reversals at approximately one-fourth of the ultimate load in order to investigate the behavior of the damaged specimen. The slab was next loaded monotonically in the opposite direction until a maximum load was reached. The slab was likewise displaced further followed by an unloading and then cycled again at ±40 KIPs.

The first major cracking occurred at a load of 120 KIPs (load point (LP) 21 in Fig. 18). Diagonal cracks formed in the northeast and southwest corners of the slab as a result of diagonal tension stresses (Fig. 19(a)). Upon further loading a large diagonal crack occurred in the southwest corner of the slab parallel to the initial diagonal cracks (LP 24). A maximum load of 168 KIPs was achieved immediately before LP 30. The displacement at the maximum load was approximately 0.16 in. At the point of maximum load a large diagonal crack developed across the center of the slab in the southeast-northwest direction. The primary failure mode was that of shear in the concrete due to diagonal tension stresses.

The steel deck corrugations deformed downward (below) the concrete cell openings as the specimen was displaced beyond the maximum load into the nonlinear region. This bending of the corrugations occurred inward from the slab edge for only three to four feet along each panel. The deformation did not extend beyond the major diagonal crack. This behavior seemed to be caused by relative motion of the concrete across the major diagonal tension crack.

A crack parallel to the deck corrugations (approximately 8 in. in from the edge) in the thin portions of the concrete above the first flute began to develop at LP 34. As the slab was further displaced to 1.00 in., the crack continued to propagate and a similar parallel crack developed in the opposite corner (Figs. 19(b) and 19(c)). The slab was then loaded in the opposite direction until a maximum load of 122 KIPs occurred, just before LP 53. A large diagonal crack occurred across the center of the slab from the northeast to southwest corners. After load removal, a final series of loading reversals at approximately one-fourth of the ultimate load was performed to observe the final stiffness and stability of the hysteretic loops (LP 57 to LP 64, see Fig. 18). Figure 19(d) shows the final crack pattern.

3.1.2. Slab 2

Slab 2 was subjected to cyclic loading with progressively increasing displacement limits. These limits were increased following a series of three cycles of displacement reversals of the slab at each limit. Fig. 20 shows the final load-displacement diagram.

Generally, the crack pattern for Slab 2 was similar to that of Slab 1. Slab 2 developed the diagonal cracks in all four corners instead of

just two, as in Slab 1 (Fig. 21(a)). A maximum positive load of 186 KIPs occurred just prior to LP 38, and a maximum negative load of 165 KIPs occurred between LP 41 and LP 42. The primary failure mode in both cases was diagonal tension cracking resulting from shear forces (Figs. 21(b) and (c)). The displacement of the slab at maximum positive load was about 0.20 in.

The slab was subjected to additional displacement reversals in the nonlinear region. Following LP 42, the steel deck corrugations again began to bend out-of-plane as in Slab 1. At LP 48, north-south cracks parallel to the deck corrugations developed, similar to those of Slab 1. Propagation of the cracks continued until, at LP 91, the cracks transversed the full width of the diaphragm (Fig. 21(d)). A chevroning crack pattern developed in the concrete in the north central portion of the slab. This cracking resulted from friction and aggregate interlocking along the cracks (Fig. 21(d)).

3.1.3. Slab 3

Slab 3 had the same deck type and concrete thickness as the pilot tests, Slabs 1 and 2. The difference between Slab 3 and the pilot tests was that the edge fasteners around the framing beams were arc spot welds instead of studs. The purpose of Slab 3, as well as Slabs 4-7, was to study the interfacial shear strength of composite slab diaphragms. The deck corrugations were oriented so as to span the north-south direction, which was perpendicular to the direction of loading. Just prior to LP 20, a maximum load of approximately 97.8 KIPs was achieved. This load point corresponded to a 0.1-in. displacement (Fig. 22). When

maximum load was reached, there was a sudden drop in load of approximately 7 KIPs. The mode of failure was interfacial shear perpendicular to the corrugations. Further displacement of the slab into the nonlinear range caused deck fold-over as shown in Figs. 23(a) and (b). This fold-over allowed the concrete to override the corrugations.

3.1.4. Slab 4

As previously stated, the deck orientation for Slab 4 was in the east-west direction instead of the north-south configuration of Slab 3. This oriented the deck parallel to the direction of loading. The purpose of this test was to ascertain the effects of the deck orientation with respect to the direction of loading.

The maximum positive load of 87.7 KIPs was reached at a displacement of 0.1 in. (Fig. 24). A sudden drop of approximately 10 KIPs occurred after reaching the maximum load. The primary mode of failure was again interfacial shear perpendicular to the corrugations. Deck fold-over occurred only along the east edge during the nonlinear load-displacement range. This is in contrast with Slab 3 where both ends folded over. The corrugations along the west edge of Slab 4 showed very little deformation or separation.

The crack patterns for Slabs 3 and 4 were very similar. There were two significant crack patterns: (1) diagonal cracks that formed on the vertical edges at each deck seam, near the maximum load (see Fig. 25), and (2) top surface cracks that occurred near the edges and parallel to the corrugations (see Fig. 26). The deck seam at each overlapping connection between deck panels forms a ridge that prevents

the concrete from slipping on one side of the seam. Thus, when the concrete slab slipped perpendicular to the deck corrugations, a diagonal crack formed at each deck seam. A secondary failure mechanism, i.e., folding over of the steel deck corrugations, formed as the displacements continued into the nonlinear range. Resistance to this folding over (which occurred in both Slabs 3 and 4) established a secondary defense plateau. The existence of defense plateaus in the composite floor diaphragm means that the diaphragm is still able to dissipate energy after ultimate load. These secondary plateaus were 64 KIPs and 50 KIPs for Slabs 3 and 4, respectively, which amounted to decreases from the maximum loads of 34% and 43%.

3.1.5. Slab 5

Slab 5 was made from Deck Type 2. The deck for this slab was placed so that the smaller width corrugations were up (Fig. 9). This deck placement made the up corrugations much stiffer and prevented the fold-over action that occurred in Slabs 3 and 4.

A maximum load of 115.6 KIPs occurred during the first cycle at 0.1-in. displacement. Figure 27 shows the load-displacement curve for Slab 5. During the second cycle, a diagonal crack (Fig. 28(a)) occurred in the southwest corner. The previous maximum load of 115.6 KIPs had not been reached when this crack formed. Further displacement into the nonlinear range caused the arc spot welds to begin failing along the east edge of the slab. Later observation indicated that the welds did not have proper penetration into the base metal. By the end of the 1-in. displacement cycles, most of the east side welds had failed and

the test was stopped. The severe flattening of the load-displacement curve (Fig. 27) at the 1-in. displacement increment was due to the weld failures. Fortunately, the welds held until the first failure mechanism had formed; thus, the ultimate load and subsequent strength analysis for Slab 5 was not affected by the edge fastener failure.

The failure mode of this slab was a diagonal tension failure of the composite diaphragm. No sudden slippage occurred at the maximum load; therefore, the slab was still considered composite when the diagonal crack occurred. As the slab was cycled further into the nonlinear range, additional diagonal cracks formed across the slab as shown in Fig. 28(b) and slippage between the concrete and steel deck occurred.

3.1.6. Slab 6

3.1.6.1. In-Plane Loading of Slab 6

Slab 6 was similar to Slab 5, except the thickness of the slab was increased to 7 in. to make diagonal tension failure less likely to occur. This test furnished a normal upper bound to the thickness of composite slabs found in most applications in practice, whereas Slab 5 provided a lower bound.

The maximum load for Slab 6, 146.8 KIPs, was reached at a 0.1-in. displacement. The load-displacement curve is shown in Fig. 29. The mode of failure for this slab was interfacial shear parallel to the corrugations. The most significant observation to make about this slab is that no cracks formed on the top surface of the concrete throughout the entire test. The concrete simply slipped parallel to the corrugations and rotated about a vertical axis as the frame was cycled back and forth. A very high secondary defense plateau formed at 107 KIPs,

after the maximum load (Fig. 29). The load-carrying mechanism in the nonlinear range was frictional interference between the steel deck and concrete. This frictional force was caused by a conflict between the displaced shapes of the steel deck and concrete, i.e., a warpage of the deck cells against the concrete cells.

3.1.6.2. Vertical Loading of Slab 6

Because the failure mechanism for Slab 6 indicated no apparent signs of distress on the top surface of the concrete, a gravity-type load was applied to observe the load-carrying capacity and crack patterns after the previous failure.

The system used to apply the load consisted of a simple frame made from W 24 × 76 framing members. The system was positioned so as to span the slab. The frame was fastened to the structural load floor. Two 25-ton capacity hydraulic cylinders were attached to the loading frame with each cylinder applying a load to a 12 × 53 H.P. spreader beam providing a four-point loading to the slab. Figure 30 shows the test setup.

The maximum total load achieved was 12.2 KIPs, i.e., approximately 3 KIPs at each load point. The initial crack appeared at the east edge of the slab and projected perpendicular to the steel deck corrugations. Further loading formed a second crack at approximately the center of the north edge and progressed parallel to the steel deck corrugations. Cracks parallel to the deck at the third points of the south edge also formed. The last crack to form was on the west edge and propagated across the slab and eventually met the initial crack. The final crack pattern is shown in Fig. 31.

As expected, the slab failed in a manner similar to flexure of a plain concrete section. Testing of composite floor diaphragm systems with combined vertical and in-plane loading is recommended for further study since most floor slabs are subjected to this type of combined loading.

3.1.7. Slab 7

Deck Type 3 (Fig. 3) was used for Slab 7. This deck was similar to the ones used in Slabs 1-4, except that it was 16-gage rather than 20-gage. The deck for Slab 7 was oriented in the north-south direction and fastened to the edge beams by arc spot welds. Nominal slab thickness was 5 1/2 in.

A maximum load of 136.8 KIPs was reached at a displacement of 0.175 in. (Fig. 32). At this point the load dropped 6 KIPs, immediately followed by a drop of 14 more KIPs before stabilizing. The immediate cause of the drop in load was localized failure of the concrete at the northeast corner (Fig. 33(a)). A continued decrease in load capacity was due to interfacial shear failure perpendicular to the corrugations. Further displacement into the nonlinear range caused the concrete to begin overriding the deck along the north side. The resulting uplifting of the concrete caused the north one-sixth of the slab to crack off along an east-west line (Fig. 33(b)), after which the deck began to tear around the welds on the north edge beam. By the time testing was terminated, the deck along the north side had completely separated from the support beam (Fig. 34).

3.1.8. Slab 8

Slab 8 was similar to Slab 2 except that fewer studs were used per side and no arc spot welds were used as edge connectors. Six studs were used on each of the east and west sides and four studs on each of the north and south edges (Fig. 8). This quantity was chosen as an approximate lower bound for the minimum number of studs required to develop the shear capacity of the slab. The number was chosen to give an expected failure of the studs and/or concrete around the studs, which could be contrasted to the diagonal tension failure that occurred in Slab 2.

Slab 8 reached a maximum load of 54.4 KIPs at a displacement of about 0.1 in. (Fig. 35). Failure was not sudden or dramatic and the decrease in load-carrying capacity was gradual. The resulting load pattern reflected the continuing deterioration of the concrete around the studs. This concrete/shear connector interface failure began around the studs nearest the corners on the north and south edges considerably prior to the ultimate load (Fig. 36(a)). After cracking around these outside studs and/or diagonal cracking had taken place across the corners (Fig. 36(b)), the concrete began to fail similarly around the inner two studs on the north and south edges. Further displacements caused cracks to propagate across the slab, parallel to the corrugations, dividing the slab into three approximately equal pieces (Fig. 37). The concrete also continued to crack and deteriorate around the studs, resulting in the eventual exposure of the studs. At very large displacements some of the studs were actually sheared off near their bases.

3.1.9. Slab 9

Slab 9 was similar in many respects to both Slabs 3 and 7, but the deck was a cellular deck, i.e., the deck consisted of a 16-gage fluted portion (Deck Type 3, see Fig. 3) spot welded to a 16-gage flat sheet. The edge fasteners, deck orientation, and overall nominal thickness were the same as for Slabs 3 and 7.

The maximum load of 220 KIPs carried by Slab 9 was the greatest of all slabs tested. The first major sign of distress in the slab was a diagonal crack across the southwest corner at +0.05-in. displacement (Fig. 38(a)). A similar crack occurred across the northwest corner at a displacement of -0.1 in. As cycling continued, an even larger crack developed across the northeast corner (see Figure 38(b)). When this crack occurred, motion was stopped (+0.149-in. displacement) and readings were taken (LP 46). Upon further displacement, however, the slab continued to pick up load and reached a maximum of 220 KIPs just prior to LP 47 (0.2-in. displacement, see Fig. 39). The load dropped about 10 KIPs before stabilizing.

This pattern of diagonal cracks in both directions continued throughout the test (Fig. 38(c)). Increasing cyclic displacements caused first the corner pieces and then those pieces closer to the middle to slip out parallel to the corrugations. At very large displacements, the deck sections began to slip noticeably relative to one another (seam slip) and some of the spot welds along the north edge failed.

3.2. Measured Results

The general behavioral trends indicated by the data (gathered from the instrumentation described in Section 2.2.2) for strains, slips and displacements are presented in the following subsections. Any strain gage data presented is plotted as strain versus load point. The data from rosette gages were reduced and transformed to a global x-y coordinate system (see Fig. 12).

3.2.1. Slab Strain Gages

Various combinations of uniaxial and rosette surface gages and concrete embedment gages were used to record the in-plane shear strain distributions across the diaphragm throughout each test (see Fig. 14). The results helped to define the load transfer mechanisms both before and after ultimate load.

Concrete strains typically reflected the cyclic loading of the slabs as illustrated in Fig. 40. Maximum top surface tensile concrete strains of about 180 μin./in. were recorded for Slabs 2 and 9. Concrete strains decreased significantly after ultimate load, especially in those slabs in which substantial cracking occurred (see Section 3.1). The embedment gages (see Figs. 14 and 16) in Slabs 7 and 8 indicate that strains are constant through the thickness of the slab in the initial linear range but not near and not after ultimate.

3.2.2. Deck Strain Gages

Strain gages corresponding in type (uniaxial or rosette) and location to the slab top surface gages were also used on the steel deck (Fig. 14). These deck gages were placed on both the top (except

Slabs 1 and 2) and bottom of the steel thickness so that the bending and axial effects could be isolated. These measured deck strains were typically quite small in both the x and y directions until after ultimate load, i.e., until after significant cracking of the concrete and/or slip between the concrete and deck had occurred (see Fig. 41). In the central part of the diaphragm, the largest strains occurred in the direction parallel to the corrugations. Due to the geometry of the steel deck, little force was transferred perpendicular (x direction) to the corrugations. The ε_y strains near the center of the slab did not exceed 900 μin./in. Near the edges of the slab, however, the largest recorded strains usually occurred parallel to the closest framing member. The strains in the deck and concrete were of similar magnitude in the initial linear range. After ultimate, however, the deck strains typically increased while the concrete strains decreased. At large displacements, the deck strains near the edge often exceeded the yield strain.

3.2.3. Slip Gages

Slip gages were used to detect relative slip between the steel deck and concrete. Determining the slip between the steel deck and concrete (in those slabs without stud connectors) was helpful in analyzing the interfacial shear mode of failure (see Sections 1.2, 3.1, and 4.2). Measured slips between the deck and concrete at load points immediately before and after ultimate load are listed in Table 3. There was little slip either before or after ultimate load in Slabs 1 and 2, due to the large number of stud connectors that confined the concrete both before and after cracking [17]. In Slabs 3, 4, 5, 7, and 9, the slip

perpendicular to the corrugations was four to six times greater than that parallel to the corrugations before ultimate, and continued to be considerably greater after ultimate. In Slab 6, the measured slips perpendicular and parallel to the corrugations were of the same magnitude before ultimate; after ultimate, however, the most significant slip occurred parallel to the corrugations. For Slab 8, the slip gages, used primarily to measure slip between the concrete and stud shear connectors, indicated that some of the studs had reached their maximum capacity prior to ultimate load (see Section 4.3.2).

3.2.4. Vertical Displacements

Dial gages and/or DCDT's were used to measure out-of-plane (vertical) deflections (Fig. 13). Vertical displacements along the main load beam (north side) followed an expected cyclic pattern. The eccentricity between the applied load and the centroid of the composite diaphragm caused the northeast corner of the diaphragm to lift upward (and the northwest corner, downward) as the diaphragm was displaced to the east. Conversely, the northeast corner moved downward (and northwest upward) as the frame was displaced to the west. This cyclic pattern is illustrated in Fig. 42.

Vertical displacement patterns near the center of the diaphragms varied from slab to slab. The centers of Slabs 1, 2, 3, 4, and 7 moved downward or cycled up and down before ultimate and moved upward after ultimate. Slab 5 gradually moved downward throughout the test. Slab 6 cycled up and down before ultimate and moved downward after ultimate. The centers of Slabs 8 and 9 cycled up and down before ultimate, moved

upward after ultimate, and downward again at maximum displacements (1.0 in.).

3.2.5. Framing Beam Strain Gages

The strain gages attached to the webs of the W 24 × 76 framing beams were used to determine the axial forces and moments at various cross sections along the beams (see Fig. 43). If the shear forces are transferred uniformly from the beams to the slab, as is assumed in Section 4.2, the axial forces along the beams should vary linearly. Data from the beam gages indicated that the force transfer was approximately uniform before ultimate load, but became nonuniform after ultimate load. The post-ultimate distribution, however, has no effect on the analysis in Section 4.2.

3.3. Summary of Behavioral Characteristics

3.3.1. Ultimate Loads and Failure Modes

The ultimate loads and failure modes are given in Table 4. The ultimate loads should be considered somewhat approximate since they were determined by visual observation of a digital voltmeter connected to Load Cell 1. The three slabs that carried the highest loads (1, 2, and 9) all failed in diagonal tension, which is Failure Mode 1 described in Section 1.2. Both Slabs 1 and 2 had a large number of studs with sufficient load transfer capacity to force the failure of the concrete. The cellular deck (Type 4) used for Slab 9 apparently had sufficient interfacial shear strength and stiffness to force a similar failure of

that slab. Slab 5 also failed in diagonal tension but at a much lower ultimate load because it had a thinner concrete slab (see Section 3.1.5).

Four of the slabs failed in interfacial shear, or Failure Mode 2. Of these four, Slab 6 carried the highest load. It was the only slab that failed in interfacial shear parallel to the corrugations. Slabs 3, 4, and 7 all failed by interfacial shear perpendicular to the corrugations. Slab 7 was made with a thicker gage deck and carried a significantly higher load than Slabs 3 and 4. Slab 8 was the only slab for which the ultimate capacity was limited, at least in part, by Failure Mode 3, connector failure.

3.3.2. Experimental Stiffnesses

3.3.2.1. Initial Stiffnesses

The experimental initial stiffnesses are listed in Table 4. Since the test program was based on displacement control rather than load control, the experimental stiffness was taken as the slope of a line through the origin and the point on the load-displacement curve corresponding to the first nominal displacement to 0.025 in. That is,

$$K_{initial} = \frac{P \text{ @ } \Delta_{nominal} = 0.025 \text{ in.}}{\Delta_{actual}}$$

where the actual displacement was taken as the average of the values given by the two DCDT's at the ends of the main loading beam (see Section 2.2.2.2). In all but one case (Slab 9) the load corresponding to 0.025-in. nominal displacement was between 0.32 P_u and 0.43 P_u. The choice of a common displacement (rather than a selection of 0.4 P_u)

provided for a consistent stiffness comparison for the same cycle of loading.

3.3.2.2. Cyclic Stiffnesses

At large cyclic displacements into the nonlinear region, the shear stiffness and strength typically degraded rapidly. To compare this degradation of stiffness, an average cyclic stiffness was determined by calculating the slope of a line extending between the maximum positive and negative load values of the third cycle hysterisis loop at each displacement increment as illustrated in Fig. 44 [17,18]. The stiffness degradation for Slabs 2-9 is illustrated in Fig. 45 by a plot of the average cyclic stiffness versus the nomimal cyclic displacement. The stiffness of all the slabs degraded quite rapidly under reversed cyclic loading. However, Slab 2 (heavily studded, see specimen descriptions in Section 2), Slab 7 (Deck Type 3), and Slab 9 (Deck Type 4) maintained noticeably higher cyclic stiffnesses into the nonlinear range than did the other specimens. At 0.1-in. displacement, for example, the cyclic stiffnesses of Slabs 2, 7, and 9 had decreased by 30, 34, and 32%, respectively; whereas the cyclic stiffnesses of Slabs 3, 4, 5, 6, and 8 had decreased by 50, 49, 52, 64, and 63%, respectively. Even though Slab 6 had the highest initial stiffness, it had a lower stiffness than Slabs 2, 7, and 9 at a cyclic displacement of 0.1 in. Slab 8 (minimum edge connector) had the lowest cyclic stiffness at all displacement increments. The stiffnesses at a displacement of 1.0 in. were very small for all of the slabs.

3.3.3. Ductility

A schematic drawing showing a typical load-displacement envelope for the nine composite slabs is given in Fig. 46. The slabs did not exhibit elastic-perfectly-plastic behavior, as can be seen from the figure. They did, however, develop a secondary defense plateau, although the load maintained at this level was significantly less than that at the initial defense plateau [19]. As the cyclic displacements increased, this secondary capacity deteriorated slowly at first, but more rapidly at large displacements (> 1.0 in.) or after another failure mechanism formed. Slab 5, for example, failed initially in diagonal tension. A secondary defense plateau then formed and was maintained until some of the arc spot welds failed. This secondary failure was followed by a drop in load and significant degradation of the load-displacement envelope.

To define the ductility of the composite diaphragm, an "equivalent" elastoplastic system was used. The load-displacement curve for this equivalent system and the superimposed curve representing the real system are shown in Fig. 46 [19]. The figure was drawn such that the indicated areas are equal, i.e., the equivalent system represents the same energy capacity as the real one. The ductility factor, defined as the ratio of the maximum displacement to the yield displacement, Δ_{max}/Δ_y, can be calculated for any Δ_{max} desired. As mentioned in Section 3.2.2.2, the third, "stabilized" cycle for each displacement increment was used to define the load-displacement envelope. The relationships between the ductility factors and the yield loads for Slabs 2-9 are plotted in Fig. 47.

Figure 47 should be used for comparison only, however, because the use of a ductility factor is not totally reliable as an index of satisfactory performance under cyclic loading [19,20]. Ductility as defined herein does not reflect the decrease in stiffness or load capacity that occurs with an increasing number of cycles. In addition, because of the test program used, ductility does not adequately describe the energy dissipation capacity of the slabs. The idealized elastoplastic envelope, for which the concept of ductility was originally developed, overestimates the energy dissipation capacity that is actually present under cyclic loading. Measuring this capacity accurately requires that the area within each hysterisis loop be calculated. This, in turn, requires either a continuous recording of the load-displacement curve or numerous load points for each cycle.

4. ANALYTICAL INVESTIGATION

This section discusses methods for predicting the stiffnesses and ultimate strengths of steel deck reinforced concrete slabs. The first subsection reviews a method developed and used previously. The second subsection discusses an alternate method and describes the development of the proposed equations. In the last subsection, the experimental results are compared to the predictions of each of the methods.

4.1. Previous Technique

The Tri-Service design manual, "Seismic Design of Buildings" [21], published by the Department of Defense, gives empirical formulas for predicting the stiffness and strength of concrete-filled steel deck diaphragms. These formulas are based on the capacity of the edge connections (arc spot welds) and were designed to fit available test data. A guided cantilever concept was used in the equation development (see Reference 17).

These equations, however, do not seem to reflect the actual behavior of a composite diaphragm [19]. The overall diaphragm appears to function more as a unit than as individual "guided cantilever" beams connected at the seams. In addition, the slip between the steel deck and concrete, as well as other possible failure modes, is not characterized in these equations. Therefore, an alternate method is proposed in the following section.

4.2. Proposed Predictive Method

4.2.1. Linear Analysis

4.2.1.1. Edge Zone Concept

The stiffness (and ultimate load) of steel deck reinforced concrete slabs is dependent upon the contribution made by the concrete slab. When shear connectors are not used, the contribution made by the concrete is solely dependent upon the capacity of the steel deck to transfer forces from the framing members to the concrete slab. The following analysis is based in part on the assumption that this transfer of forces from frame to slab effectively takes place within a relatively narrow band along the lengths of the framing members (see Fig. 48).

There is considerable evidence to support this "edge zone" concept. Interfacial shear failure (i.e., failure at the deck/concrete interface) and/or localized failure of the concrete within the edge zone was evident in all the tests in which diagonal tension failure did not control.

In addition, a full-scale slab was analyzed using a general purpose computer program (SAP 6). The framing beams and concrete reaction block were incorporated in the analysis and spring elements (special beam elements with an assumed stiffness of 30 KIPs/in./in.) were used to idealize the flexibility of the connection of the slab to the framing members. The concrete slab was idealized as a thick plate using three-dimensional, 20-node, isoparametric, solid elements.

As part of this analysis, a segment of unit width along the slab centerline was isolated as indicated in Fig. 49. The stress resultants (based on plate theory, see Reference 22) on this segment at the edge of

the slab are represented in Fig. 50. The analysis indicated that components Q_x and N_x (and, therefore, reactions q_z and q_x), N_y, M_y, and M_{yx} are all essentially zero (see Fig. 51). As could be expected from plate theory and statics, Q_y and M_{xy} are nonzero near the edge due to the eccentricity of the applied load with respect to the slab cross section. However, at a small distance in from the edge, these stress resultants also go to zero, which means, in effect, that the interfacial shear stresses between the steel deck and the concrete go to zero. Based on this analysis, the significant edge zone forces are those shown in Fig. 52.

Since the interfacial shear forces have significant magnitude only near the edge, they can be characterized in a relatively simple test specimen which represents an isolated portion of the edge zone. As shown in Fig. 53, a slice at the bottom of the edge zone is visualized as representing the steel deck. If it is also assumed that the concrete portion of the slab is rigid, all the internal stress resultants shown in Fig. 52 can be replaced by a statically equivalent force, q_y, shown on the left in Fig. 53. With the above assumptions, the interfacial shear stresses associated with Fig. 53 are approximately equal to those in Fig. 52 and, hence, those in Fig. 49.

A similar conclusion could be reached based on St. Venant's principle, which states that, "if the forces acting on a small portion of the surface of an elastic body are replaced by another statically equivalent system of forces acting on the same portion of the surface, this redistribution of loading produces substantial changes in stresses

locally but has negligible effect on the stresses at distances which are large in comparison with the linear dimensions of the surface on which the forces are changed." (See References 19 and 23.) At large (relative to the slab thickness) distances from the edge, the in-plane shear force N_{xy} is the only significant internal force. Therefore, interfacial shear stresses are zero outside the "edge zone." Inside the "edge zone," these stresses will be approximately equal to those existing in Fig. 53. The above analysis has been based on an isotropic composite slab. The equation development in Sections 4.2.1.2 and 4.2.2.2 assumes that the orthotropic character of the steel deck/concrete system does not significantly affect the preceding arguments.

In effect, the equivalent force system in Fig. 53 shows that the shear stiffness and strength of steel deck reinforced concrete slabs is dependent upon the stiffness and capacity of the steel deck in transferring forces from frame to concrete and that this force transfer occurs primarily in a relatively narrow "edge zone." To determine the stiffness and force transfer characteristics of the various types of deck used in the full-scale tests, a series of pushout tests were designed based on Fig. 53. These specimens were fabricated and tested to determine stiffnesses and interfacial shear strengths both parallel and perpendicular to the corrugations (see Figs. 54 and 55). The results of these pushouts are listed in Table 5. In this table, Q_p and Q_t are the ultimate strengths of the pushout specimens parallel and transverse to the corrugations, respectively. The values of the parallel and transverse stiffnesses, k_p and k_t, are the slope (from

linear regression) of a straight line through the load-slip data up to a slip of 0.005 in. Appendix B gives more details on the pushout tests. Their incorporation into the slab analysis is discussed in the following section.

The finite-element analysis also predicted the distribution of the frame-to-slab forces around the perimeter of the slab. The results are shown in Fig. 56, where q_t and q_t' are forces transverse to the corrugations and q_p and q_p' are forces parallel to the corrugations (similar to q_y and q_x in Fig. 50). This distribution and the edge zone concept are used in the following sections in the development of equations to predict the initial stiffness and ultimate strength of composite diaphragms.

4.2.1.2. Stiffness

In calculating the in-plane shear deflections for steel deck diaphragms (no concrete), the diaphragm with the edge beams is idealized as a plate grider [17,7,24]. The total deflection is then given by

$$\Delta_T = \Delta_b + \Delta_s \qquad (4\text{-}1)$$

where Δ_b is the bending deflection of the plate girder and Δ_s is the shear deflection of the web (i.e., steel deck). This idealization of the diaphragm as a plate girder was also used for the composite slabs. In addition, the stiffness of the edge connections and the bending stiffness of the composite slab were taken into account. The total deflection, Δ_T, of the composite diaphragm then becomes

$$\Delta_T = \Delta_b + \Delta_s + \Delta_z \qquad (4\text{-}2)$$

where Δ_b is the bending deflection of the plate girder (including the beams and composite slab), Δ_s is the shear deflection of the composite web, and Δ_z is the deflection due to the deformation of the edge zone, which includes the effects of connector deformations.

The bending deflection, Δ_b, at the free end of the cantilevered composite girder is

$$\Delta_b = \frac{Va^3}{3(E_c I_c + E_s I_s)} = \frac{V}{K_b} \qquad (4\text{-}3)$$

where a is the length of the cantilever as shown in Fig. 57. The moment of inertia of the composite web, I_c, is based on the average thickness of the concrete, taking into account the variation in thickness due to the corrugations plus n times the thickness of the deck where $n = E_s/E_c$. It should be noted that the above expression assumes that the slab is totally effective in resisting bending deformation. This is not completely true because of the flexibility of the edge zone at the fixed support (see Fig. 58 and the associated discussion below). Thus, an extreme upper bound on the bending deflection can be obtained by neglecting I_c in the above equation. However, slips along the fixed edge in the initial linear range were typically quite small and, therefore, including I_c was assumed to give a more realistic value than excluding it would.

The shear deflection Δ_s, is given by

$$\Delta_s = \frac{Va}{G_c t_e b} = \frac{V}{K_s} \qquad (4\text{-}4)$$

where G_c is the modulus of rigidity of the concrete, t_e is the average thickness of the concrete plus n_s times the thickness of the deck where $n_s = G_s/G_c$, and b is the depth of the cantilevered girder.

The deflection due to the deformation of the edge zone, Δ_z, was based on the results of the pushout tests. In order to develop an equation to predict this contribution, the edge zone force distribution predicted by the finite-element analysis (Fig. 56) was idealized as that shown in Fig. 59. The corresponding forces on the framing members are shown in Fig. 60. In the linear range the stiffness of the edge zone was idealized by a series of springs, K_t, K_t', K_p, and K_p' as shown in Fig. 58. The forces in Fig. 59 can then be written as

$$q_p = K_p \Delta_p$$

$$q_p' = K_p' \Delta_p$$

$$q_t = K_t \Delta_t$$

$$q_t' = K_t' \Delta_t \qquad (4\text{-}5)$$

where Δ_p and Δ_t are the edge zone displacements in the parallel and transverse directions, respectively. These displacements can be visualized as the relative displacements between the framing members and a rigid slab as illustrated in Fig. 61.

An equation giving the diaphragm deflection, Δ_z, due to deformation of the edge zone can be developed by first summing forces along the north framing beam represented in Fig. 60. This summation gives

$$V = q_t b + \frac{a' q_t'}{3a} (3a - 2a') \tag{4-6}$$

or, with substitutions for q_t and q_t' and letting $\ell_t = a' - 2a'^2/3a$,

$$V = [K_t b + k_t' \ell_t] \Delta_t \tag{4-7}$$

Similarly, from the summation of moments on the south reaction block,

$$V = \frac{q_p' b^2}{6a} + q_p b + \frac{b' q_p'}{6a} (3b - 2b') \tag{4-8}$$

or, with substitutions for q_p and q_p' and letting $\ell_p = (b^2 + 3bb' - 2b'^2)/6a$

$$V = [K_p b + K_p' \ell_p] \Delta_p \tag{4-9}$$

Figure 61 shows the relationships involving Δ_t, Δ_p, and Δ_z which, assuming small displacements, are

$$\Delta_t = \frac{\Delta_z}{2} + \frac{\theta a}{2} \tag{4-10}$$

and

$$\Delta_p = - \frac{\theta b}{2} \tag{4-11}$$

where θ is the rotation of the concrete about the center point of the slab. These relationships are also based on the assumption that the slab is rigid and does not crack.

Substituting for Δ_t and Δ_p in Equations (4-7) and (4-9) and eliminating θ gives

$$V = \left[\frac{1}{\frac{2}{K_t b + K_t' \ell_t} + \frac{2a}{K_p b^2 + K_p' b \ell_p}} \right] \Delta_z \qquad (4\text{-}12)$$

or

$$V = K_z \Delta_z \qquad (4\text{-}13)$$

where K_z is the stiffness contribution of the edge zone and is equal to the term within the brackets in Equation (4-12). The values of K_p and K_p' are assumed to be equal, as are the values of K_t and K_t'. (These assumed equalities have not been verified since no pushout specimens corresponding to K_p' or K_t' were tested.) Making use of these equalities in Equation (4-12) gives

$$K_z = \frac{1}{\frac{2}{K_t (b + \ell_t)} + \frac{2}{K_p (b^2 + b \ell_p)}} \qquad (4\text{-}14)$$

The stiffness factors K_p and K_t were obtained from the pushout tests (see Section 7) and are listed in Table 5. The values of a' and b' were taken as b/12 and a/12, respectively, using the American Institute of Steel Construction (AISC) Specifications Section 1.11.1 as a guide [25], even though this article was not intended to apply necessarily to in-plane loading. Equation (4-14) was used to calculate the edge zone stiffness, K_z.

No pushouts were tested to determine the stiffnesses of studded connections. Therefore, the values of K_t and K_p for the studded slabs (1, 2, and 8) were calculated using two empirical equations developed by Ollgaard, Slutter, and Fisher [26]. The first of these gives the ultimate load capacity of a stud as

$$Q_u = 1.106\ A_s f_c'^{0.3}\ E_c^{0.44} \qquad (4\text{-}15)$$

where A_s is the cross-sectional area of the stud and f_c' and E_c are the concrete compressive strength and modulus of elasticity, respectively. These values of Q_u were modified by AISC reduction formulas 1.11-8 and 1.11-9 for stud shear connectors with formed steel deck [25].

For each value of Q_u, the load-slip curve for slips from 0.0 in. to 0.005 in. (in intervals of 0.0005 in.) was calculated using the equation

$$Q = Q_u(1 - e^{-18\Delta})^{2/5} \qquad (4\text{-}16)$$

from Reference 26. A linear regression was performed on each of these sets of load-slip data to determine the stiffness values per stud. Finally, the values of K_t and K_p as listed in Table 5 were determined from dividing by the number of stud spaces.

An equation for the stiffness of the composite diaphragm can be developed based on Equation (4-2). Substituting for the individual deflections gives

$$\frac{V}{K_T} = \frac{V}{K_b} + \frac{V}{K_s} + \frac{V}{K_z} \qquad (4\text{-}17)$$

where

K_T = total diaphragm stiffness

K_b = bending stiffness of the composite girder (Equation (4-3))

K_s = shear stiffness of the composite web (Equation (4-4))

K_z = edge zone stiffness (Equation (4-14))

Solving for K_T gives

$$K_T = \frac{1}{\frac{1}{K_b} + \frac{1}{K_s} + \frac{1}{K_z}} \tag{4-18}$$

where K_T is the total initial stiffness of the composite diaphragm.

4.2.2. Ultimate Load

The ultimate load capacity of steel deck reinforced concrete slabs can be limited primarily by one of three things: the shear capacity of the concrete, the interfacial shear strength of the deck, or the strength of the edge fasteners (see Section 1). Each of these will be discussed individually in the following subsections.

4.2.2.1. Composite Slab--Diagonal Tension Failure

The ultimate strength based on the shear failure of the concrete can be calculated using the shear wall equation from the American Concrete Institute (ACI) Code 318-77 [27]. Assuming there are no axial loads (i.e., N_u = zero), ACI Equation 11-33 gives

$$V = 3.3\sqrt{f'_c}\ hd \tag{4-19}$$

In applying this equation, h is taken as the effective concrete thickness, t_e, where $t_e = t_a + n_s t_s$ (see discussion of Equation (4-4)). The

average thickness of the concrete (t_a) was used since the diagonal crack length is large relative to the corrugation width [19,28]. The ratio n_s (= G_s/G_c) times the thickness of the steel was included because when diagonal tension failure controls, the steel deck is presumably still acting integrally with the concrete, i.e., the interfacial shear strength of the edge zone has not been exceeded and, hence, there is still composite action occurring throughout the diaphragm. The value of d in Equation (4-19) is taken as the full-panel width instead of 0.8 times the full width [19]. For the tests in this project, therefore, Equation (4-19) can be written

$$V = 3.3\sqrt{f'_c}\, t_e b \qquad (4\text{-}20)$$

4.2.2.2. Interfacial Shear Failure

In order to develop equations to predict the ultimate strength of composite diaphragms based on interfacial shear capacity, the edge zone force distribution shown in Fig. 59 was assumed to approach that shown in Fig. 62 at ultimate load. This assumption requires that the edge zone behavior be ductile. Though this is not exactly true, the distribution is assumed to adequately represent the actual behavior. This distribution also presumes that the concrete portion of the slab has not failed. The corresponding forces on the framing members are shown in Fig. 63. Summing forces on the north framing beam gives

$$V = q_t b + \frac{2a'q'_t}{a}(a - a') \qquad (4\text{-}21)$$

or, letting $\ell_t' = 2a' - 2a'^2/a$

$$V = q_t b + q_t' \ell_t' \tag{4-22}$$

Summing moments on the south reaction block gives

$$V = q_p b + \frac{q_p' b^2}{4a} + \frac{b' q_p'}{a} (b - b') \tag{4-23}$$

or, letting $\ell_p' = (b^2 + 4bb' - 4b'^2)/4a$

$$V = q_p b + q_p' \ell_p' \tag{4-24}$$

At ultimate load, the maximum values of q_t and q_t' were taken as Q_t, the maximum load from the transverse pushout tests. Similarly, the limiting value of q_p was taken as Q_p, based on the parallel pushout tests (see Table 5). Based on Coulomb's friction theory, the maximum value of q_p', identified as Q_p', was taken as the sum of two forces (see Reference 19). The first of these two forces is the mechanical/chemical bond between the steel and concrete, or cohesion force, taken as Q_p. The second is a frictional force equal to the normal force against the up corrugation, q_t, times the coefficient of friction between the steel deck and concrete, i.e.,

$$Q_p' = Q_p + \mu q_t \tag{4-25}$$

or, from Equation (4-22), with $q_t = q_t'$

$$Q_p' = Q_p + \frac{\mu V}{b + \ell_t'} \tag{4-26}$$

Making these substitutions in Equations (4-22) and (4-24) gives

$$V = \text{minimum} \begin{cases} Q_t(b + \ell_t') & (4\text{-}27) \\ Q_p \left[\dfrac{(b + \ell_p')(b + \ell_t')}{b + \ell_t' - \mu\ell_p'} \right] & (4\text{-}28) \end{cases}$$

A value of 0.7 was assumed for μ based on ACI 318-77, 11.7.5 [27].

4.2.2.3. Edge Fastener Failure

In all but one (Slab 8) of the tests conducted under this research program an exaggerated number of edge connections was used in order to eliminate the edge fastener failure mode. However, equations to predict the ultimate load based on edge connector capacity can be developed by again assuming the force distribution in Fig. 62. With this distribution, the edge connections near the corners may control the ultimate capacity because of the vector addition of the perpendicular forces q_p' and q_t or q_t' and q_p. Assuming the force distribution in Fig. 64 (from Fig. 62), the component forces (Fig. 65) on the typical corner connector at "A" can be written as

$$F_1 = \frac{q_t b}{n_b} \qquad (4\text{-}29)$$

and

$$F_2 = \frac{q_p' \ell_c}{n_c} \qquad (4\text{-}30)$$

where n_b and n_c are the numbers of connectors along lengths b and ℓ_c, respectively. The length ℓ_c is taken as b' or the distance from the edge of the slab to a point halfway between the connectors (or groups of connectors) at "A" and "C", whichever is less. If the ultimate strength of a connector is Q_u, then Q_u can be related to the components F_1 and F_2 by

$$Q_u = \left[(F_1)^2 + (F_2)^2\right]^{1/2} = \left[\left(\frac{q_t b}{n_b}\right)^2 + \left(\frac{q'_p \ell_c}{n_c}\right)^2\right]^{1/2} \qquad (4\text{-}31)$$

From Equations (4-22) and (4-24), assuming that $q_t = q'_t$ and $q_p = q'_p$

$$q_t = \frac{V}{b + \ell'_t} \qquad (4\text{-}32)$$

$$q'_p = \frac{V}{b + \ell'_p} \qquad (4\text{-}33)$$

Substituting for q_t and q'_p in Equation (4-31) and solving for V gives

$$V = \frac{Q_{ut}}{\left[\left(\frac{b}{(b + \ell'_t)n_b}\right)^2 + \left(\frac{\ell_c}{(b + \ell'_p)n_c}\right)^2\right]^{1/2}} \qquad (4\text{-}34)$$

where Q_{ut} is the ultimate strength of a stud with the deck perpendicular to the edge member.

Along the edge where connector "B" is located (see Figs. 62 and 64), either the corner connectors or the middle connectors (those within length a minus those within lengths a') might control, depending upon the relative numbers of connectors within lengths a and a'. If the

corner connectors at "B" control, the ultimate capacity (following a procedure similar to that used to derive Equation (4-34) is given by

$$V = \frac{Q_{up}}{\left[\left(\frac{a}{(b + \ell'_p)n_a}\right)^2 + \left(\frac{a'}{(b + \ell'_t)n'_a}\right)\right]^{1/2}} \qquad (4\text{-}35a)$$

where n_a and n'_a are the numbers of connectors in legnths a and a', respectively, and Q_{up} is the ultimate strength of a stud with the deck parallel to the edge. If there are sufficient middle connectors to carry additional load after the corner connectors have failed, the ultimate capacity is given by

$$V = Q_{up}(n_a - 2n'_a) \qquad (4\text{-}35b)$$

The values of Q_{ut} and Q_{up} could be determined from pushouts similar to those used to determine interfacial shear strengths or from provisions in the AISC Specification. The ultimate strength based on edge connector capacity would then be determined by

$$V = \text{minimum} \begin{cases} \text{Equation (4-34)} \\ \text{maximum} \begin{cases} \text{Equation (4-35a)} \\ \text{Equation (4-35b)} \end{cases} \end{cases}$$

A similar approach could be used to predict the failure of arc spot welds along the edges. In this case Q_u (= Q_{ut} = Q_{up}) would represent the ultimate strength of one weld. This approach is now, at best, tentative. Failure of the connectors did not control the

ultimate capacity of any of the specimens (except, perhaps, Slab 8, see Section 4.3.2) and, therefore, no assessment can be made as to the validity of the assumptions or equations. A study of the influence of end-span studs on one-way acting steel deck reinforced composite slabs is presented in Appendix A.

4.3. Comparison of Experimental and Analytical Results

The main emphasis of the analytical work was to develop equations to predict the initial stiffness and ultimate load of steel deck reinforced concrete slabs. This section will discuss the application of the equations developed in Section 4.2 and compare the predictions based on those equations with the results of the actual tests.

4.3.1. Initial Stiffness

The experimental stiffnesses, the stiffnesses predicted by Equation (4-18), and those predicted by the Tri-Service equations are listed in Table 6. The values of K_b, K_s, and K_z used in Equation (4-18) were obtained from Equations (4-3), (4-4), and (4-14), respectively. To calculate K_z, values for K_t and K_p (i.e., the stiffness of the edge zone transverse and parallel to the corrugations) for the slabs are listed in Table 5. The value of K_T was quite sensitive to the value of K_z and, therefore, to the values of K_t and K_p. However, these results from the pushout tests were sometimes quite erratic (see Appendix B).

As shown in Table 6, the predicted stiffnesses for the studded specimens, especially Slabs 1 and 2, were considerably higher than the measured stiffnesses. There are two possible explanations for this.

First, the AISC reduction formulas for Q_u do not take into account the location of the studs relative to the edge of the slab. If the studs are near the edge, as in this case, lower values of Q_u (see Reference 29) and, hence, K_t and K_p, could be expected. Secondly, Equation (4-16) is based on load-slip characteristics of flat slabs with reinforcing around the studs. The stiffness of studs with steel deck and without reinforcing would presumably be lower than this equation predicts. More reasonable values of K_t and K_p, and, therefore, K_T could probably be obtained by testing studded pushout specimens (see Appendix B).

The predicted stiffnesses for the nonstudded specimens were generally in closer agreement with the experimental values. For two of these slabs (5 and 6), however, there was a significant difference in experimental and predicted values. As mentioned earlier, this is probably due to the erratic results of the pushout tests (see Appendix B). Further refinements in the design and testing of the pushout specimens would lead to more consistently reasonable stiffness predictions for both studded and nonstudded composite diaphragms.

4.3.2. Ultimate Load

Table 7 lists the experimental and the predicted ultimate loads based on both the proposed equations and the Tri-Service equations. The proposed method involves the prediction of the ultimate capacity for three possible failure modes (only two of these three apply to studded specimens). The three modes and the equations applying to each are discussed in Sections 1.2 and 4.2, respectively. The lowest of

the three (or two) values is the predicted ultimate strength of the composite diaphragm.

The values of Q_t and Q_p (i.e., the ultimate strength of the edge zone transverse and parallel to the corrugations) used in Equations (4-27) and (4-28) were obtained from the pushout tests and are listed in Table 5 (see Appendix B). The values of Q_u for the stud connectors used in Equations (4-34), (4-35a), and (4-35b) were calculated using Equation (4-15) and the appropriate AISC reduction formulas. The Q_u values for the arc spot welds were determined using the equation (from Reference 30)

$$P(= Q_u \text{ for spot weld}) = 2.2\, t_n d_a \sigma_{ult} \qquad (4\text{-}36)$$

where t_n = the net thickness of the deck (single or double sheet minus the thickness of any coatings), $d_a = d - t$ (single sheet) or $d - 2t$ (double sheet) where d is the diameter of the spot weld, and σ_{ult} is the ultimate tensile strength of the sheet steel. As mentioned previously, an exaggerated number of edge connectors were used in most of the tests; therefore, Mode 3 controlled the predicted strength only for Slab 8. For all the other slabs, the Mode 3 predicted strengths were considerably greater than the controlling values, as was expected.

The proposed equations gave good predicted strengths for the first five slabs. The failure modes predicted by the controlling values were also the actual failure modes, i.e., Slabs 1, 2, and 5 failed in diagonal tension (see Figs. 19, 21, and 38) and Slab 3 failed by interfacial shear perpendicular to the corrugation (see Fig. 23).

The deck for Slab 4 was oriented 90^{o} with respect to Slab 3. Therefore, the values of Q_t and Q_p should be interchanged when using Equations (4-27) and (4-28), which gives a predicted ultimate strength of 97.2 KIPs (10.8% error). Prior to ultimate, however, a crack formed above the up corrugation nearest the south edge of the slab. (See Fig. 26(b). Similar cracks occurred in Slab 3, but not before ultimate). This crack occurred presumably because of the force distribution along the reaction block (see Fig. 59). A tentative analysis to predict this pre-ultimate crack is based on the force system shown in Fig. 66. The line of action of the stress resultant q_t' is assumed to be a distance f above the down corrugation. The maximum tensile stress at the bottom surface of the concrete above the up corrugation is given by

$$f_t = q_t'\left(\frac{1}{c} + \frac{6e}{c^2}\right) \tag{4-37}$$

Because the deck for Slab 4 was oriented east-west instead of north-south, q_t' is given by

$$q_t' = \frac{V}{b + \ell_p} \tag{4-38}$$

from Equations (4-5) and (4-9). Substituting into Equation (4-37) and solving for V gives

$$V = \frac{f_t(b + \ell_p)c^2}{c + 6e} \tag{4-39}$$

For f of 0.75 in. (see discussion of last series of pushout tests in Appendix B), c = 2.5 in., and $f_t = f_r$ = 502 psi (from modulus of rupture tests), Equation (4-39) predicts that a load of about 29 KIPs would cause a tensile crack. The added strength of the deck would increase this value somewhat. Test data indicate that the crack occurred at a load somewhere between 31 and 68 KIPs.

If this crack is taken into account in predicting the ultimate strength of Slab 4, Equation (4-23) becomes

$$V = q_t b \qquad (4\text{-}40)$$

since q_t' goes to zero. Equation (4-40) gives the predicted ultimate load listed in Table 7. It should be emphasized that the preceding analysis is not intended to be part of the proposed method but rather to illustrate that localized failure of the concrete within the edge zone can significantly affect the capacity of composite diaphragms. Equations (4-27) and (4-28) were based, in part, on the assumption that the concrete portion of the slab does not fail (see Section 4.2.2). Since Slab 4 shows that such pre-ultimate, localized failure is possible, further research should be done to determine how to predict such failure and its effects on ultimate strength.

The results of the predictive equations for Slabs 6-8 were not as good as they were for Slabs 1-5. The predicted value for Slab 6 was controlled by Q_p and Equation (4-28). (Equation (4-27) gives V_u = 200 KIPs.) Further refinements in the pushout tests might give more representative values of Q_p and, thereby, a more accurate predicted strength for Slab 6.

No pushouts were tested using Deck Type 3 (Slab 7) due to a shortage of that deck type. Therefore, the predicted value listed for Slab 7 is based on the results of the pushouts for Deck Type 4. Initial expectations were that the values for Q_t and Q_p for both Deck Types 3 and 4 would be essentially the same, i.e., the addition of a bottom pan was not expected to significantly affect the interfacial shear strength of the deck. Final results suggest, however, that there may indeed be a difference. The error in the predicted strength for Slab 7 is, therefore, more likely to be a result of no corresponding pushout data than a reflection on the worth of the predictive equations.

An attempt was made in Slab 8 to force a failure of the shear connectors (Failure Mode 3) rather than of the concrete slab. Stud shear connectors were provided to carry approximately 75% of the diagonal tension failure load (see description of test specimens in Section 2.1). In the actual test, diagonal tension cracks occurred at both the northeast and northwest corners (see Fig. 35) prior to ultimate. As a result, the corner studs on the north edge were incapable of carrying much load and only the two middle studs on the north beam could contribute significantly to the total ultimate capacity. Consequently, the actual ultimate load was considerably less than that predicted. This localized diagonal tension failure deserves additional study.

Slab 9 was the only specimen that was constructed using a cellular deck consisting of both a fluted and a flat sheet portion (Deck Type 4). The strength of the flat sheet portion was assumed to add directly to

the strength of the diaphragm. Plate buckling theory was applied to the flat sheet. The shear stress at buckling in a flat sheet subjected to pure shear is given by

$$f_{crs} = \frac{K_s \pi^2 E}{12(1 - \mu^2)\left(\frac{b}{t}\right)^2} = \frac{26.2 \times 10^6 \, K_s}{(b/t)^2} \qquad (4\text{-}41)$$

if $f_{crs} < f_y/(2\sqrt{3})$ [31]. In this equation, b/t is the plate width-to-thickness ratio and K_s is a nondimensional plate buckling coefficient. The value of b was taken to be 9 in., the distance between the welds connecting the corrugated portion of the deck to the flat sheet portion. For long, narrow plates with simply supported edges, the value of K_s is given as 5.34 (from Reference 31). With t = 0.057 in. (see Table 2), Equation (4-41) gives a shear stress at buckling of 5610 psi, or for the entire area of the flat sheet, a buckling load of 57.6 KIPs. This value was added to the ultimate loads calculated using Equations (4-26) and (4-27) to obtain the values listed in Table 7. The displacement at ultimate of Slab 9 was much greater than the displacement corresponding to the buckling stress of 5610 psi. Therefore, the pan most likely reached this buckling stress despite some slip along the seams.

5. SUMMARY AND CONCLUSIONS

5.1. Summary

A facility was designed and constructed for testing composite steel deck diaphragms. Nine full-scale (15-ft square) diaphragms were tested using a cantilever-type test frame. The first specimen was used mainly to check the adequacy of the test frame and controls, instrumentation, and data acquisition system. These tests were conducted to study three possible failure modes of steel deck reinforced slabs. The three basic modes are diagonal tension failure, interfacial shear failure, and edge fastener failure. All slabs were constructed with normal weight concrete.

The tests followed a displacement program controlled by an MTS closed-loop system. A reverse cyclic displacement program with progressively increasing displacements was used for all slabs except the first pilot specimen, which was loaded monotonically. Instrumentation included load cells, displacement transducers, and strain, slip, clip, and dial gages. Data were recorded by a 100-channel data acquisition system and reduced on a digital computer.

Slabs 1 and 2 were identically constructed using 3-in. deep, 20-gage, composite-type steel deck. Large numbers of stud shear connectors were used to connect the diaphragms to the framing beams. The two slabs had similar crack patterns, ultimate loads, and stiffnesses. Both failed by diagonal tension cracking of the concrete.

Slabs 3 and 4 were made using the same type of deck as Slabs 1 and 2, but arc spot welds rather than studs were used as edge connectors.

Slab 3 was loaded perpendicular to the corrugations, Slab 4 parallel to them. Both slabs failed by interfacial shear perpendicular to the corrugations. The ultimate loads and stiffnesses were similar. At large displacements, the up corrugations along the edges folded over.

Slabs 5 and 6 were constructed using 1 1/2-in. deep, 16-gage, composite-type steel deck and arc spot welds as edge connectors. The only significant difference between the two was in overall thickness; Slab 5 had a nominal thickness of 3 1/2 in. while Slab 6 was 7 in. thick. Slab 5 failed by diagonal tension cracking of the concrete, Slab 6 by interfacial shear parallel to the corrugations.

Slab 7 was similar to Slabs 3 and 4 except that the deck used was 16-gage rather than 20-gage. Ultimate load and stiffness were significantly higher for Slab 7 than for Slabs 3 and 4, though the failure mode was the same.

Slab 8 was similar to Slabs 1 and 2 except that a much smaller number of stud shear connectors were used. Initial failure occurred in the concrete around the studs and was followed by diagonal tension cracks at two corners. The ultimate load and stiffness of Slab 8 were the lowest of all slabs.

Slab 9 was similar to Slab 7 except that the deck had a flat steel sheet welded to the bottom corrugations (cellular deck). Slab 9 failed in diagonal tension; diagonal tension cracks developed throughout the test. Slab 9 had the highest ultimate load and the second highest stiffness of all the slabs.

The ductilities of the slabs were determined by obtaining the yield load and displacement for an energy-equivalent, elastic-perfectly-plastic system. Cyclic stiffnesses were compared by calculating the stiffnesses from the third-cycle hysterisis loop at each displacement increment for each of Slabs 2-9.

Equations were developed to predict the ultimate load and initial stiffness of composite steel deck diaphragms. An important assumption made in the development of these equations is that the applied force is transferred from the edge beams to the concrete within a relatively narrow band around the perimeter of the diaphragm, defined as the edge zone.

The force transfer capacity and stiffness of the edge zones of the various types of deck were determined by conducting pushout tests. Pushout specimens to obtain values in both transverse and longitudinal directions were tested. Stiffnesses and ultimate capacities of stud shear connectors were determined using stud load-slip equations. These deck and connector values were used in the proposed predictive equations.

In the proposed method, the predicted stiffness was calculated using Equation (4-18). The predicted ultimate strength was calculated as the minimum of: (1) the ACI shear wall equation for diagonal tension (Equation (4-19)), (2) interfacial shear strength equations (Equations (4-27) and (4-28), and (3) edge fastener capacity equations (Equations (4-34), (4-35a), and (4-35b)). These predictions correspond to the three failure modes identified above.

Stiffnesses and strengths were also calculated using the Tri-Service Design Equations [21]. The results from these two procedures were compared to the experimental values.

5.2. Conclusions

The following conclusions are based on the results of the study summarized above.

1. The test facility performed very well.
2. The stiffness of composite steel deck diaphragms subjected to cyclic loading decreases rapidly, although the use of stud shear connectors and/or stiffer deck types affects the rate of decrease significantly. By the third cycle at a 1.0-in. displacement, the stiffness was less than 4% of the initial cyclic stiffness for all the diaphragms.
3. Composite steel deck diaphragms that fail by diagonal tension or interfacial shear can still carry significant load after ultimate. This secondary capacity decreases slowly at first, but rapidly at large displacements (1.0 in. and greater).
4. Based on the results of Slabs 3 and 4, a change in deck orientation does not greatly affect the initial stiffness or ultimate capacity of composite steel deck diaphragms.
5. The Tri-Service method gave good ultimate load predictions for Slabs 3, 4, and 7. Requirements for applying this method need further definition. The Tri-Service method does not give satisfactory predictions for certain failure modes.

6. The proposed method is a reasonable approach to predicting the initial stiffness and ultimate capacity of composite steel deck diaphragms and therefore has good potential as a design tool. However, the effects of such things as changes in slab dimensions, the use of other types of deck, and localized failures require further study before a finalized design method can be developed and proposed. The edge zone concept seems to effectively represent the actual behavior of such diaphragms.

5.3. Recommendations for Continued Study

1. Additional testing and/or analysis should be done to check the validity of the assumption that the pushouts adequately represent the edge zone of the diaphragms. This work should include the effects of pushout variables including concrete strength and thickness, effective length and width, and line of action of the applied load.
2. Refinements should be made in the design and testing of pushout specimens so that reasonably consistent and reliable results can be obtained for all types of deck.
3. Pushouts made with Deck Type 3 should be tested to obtain measured values for the stiffness and strength of that deck.
4. The assumed representation and magnitude (coefficient) of the frictional interlocking force should be further evaluated.

5. Additional specimens, which have been designed to fail in Mode 3 (edge connector failure), should be tested to evaluate Equations (4-34), (4-35a), and (4-35b).
6. Additional research should be conducted to analyze the post-ultimate behavior and energy dissipation capacity of composite steel deck diaphragms.
7. Further study should be done on the contribution of the bottom pan in cellular deck to the stiffness and strength of composite diaphragms.
8. Further analysis of the data from Slab 8 should be done to determine in what order various failure mechanisms formed and how they affected one another throughout the test.
9. The effects of localized failure within the edge zone should be further analyzed.
10. Additional potential modes of failure not formed in those tests should be investigated.
11. An analysis and experimental determination of in-plane diaphragm loads in combination with gravity (vertical) loads needs to be investigated. The interfacial shear strength under combined gravity and diaphragm loading needs to be determined.
12. Additional work may be needed to extend behavior and analytical results to include parameters not contained in this study.

6. APPENDIX A: VERTICAL LOAD TESTS

6.1. Introduction

The design of formed metal deck composite slabs for vertical loads is controlled by one-way action behavior, due to the large bending stiffness of the slab in the direction parallel to the longitudinal direction of the deck. Previous research at Iowa State University [9-15] resulted in design equations [13] for predicting the load capacity of one-way acting steel deck reinforced composite slabs without end-span studs. The most predominant mode of failure was found to be that of shear-bond. Due to the shear-bond mode of failure, the design equation for shear-bond capacity prediction was based on a modification of Equation 11-6 in the American Concrete Institute (ACI) Code [27].

For steel deck composite specimens with studs, the research [32-35] has concentrated on the composite action of the beam or girder. To determine the influence of end-span studs on one-way acting steel deck reinforced composite slabs, several specimens subjected to two-point loading (Fig. 67) were tested [36]. Identical slabs without end studs were tested to provide a basis for comparison.

By restraining the normally observed [14] end-span slippage, the studs were expected to provide an increase in load-carrying capacity. Three areas were investigated, namely:

1. Determining the percentage of load increase for studded versus nonstudded specimens.
2. Determining the behavioral characteristics for the studded specimens.

3. Developing an analysis procedure for the prediction of ultimate load of studded specimens.

6.2. Specimens

A total of 15 specimens were cast and tested. Each specimen was 3 ft wide, had an overall thickness of 5 1/2 in., and was reinforced with 3-in. deep deck, Deck Type 1 or 3 (Fig. 68). The fifteen specimens were divided into four groups, based on out-to-out length of the specimen and on deck gage (Table 8). Each group included two studded specimens together with either one or two nonstudded specimens. Each studded specimen contained two studs at each end, one in each down corrugation. The studs were welded through the deck to 0.5 in. × 6 in. × 36 in. steel plates using the same stud and burnoff height as those used in the diaphragm tests.

The loading apparatus was designed to provide a two-point line loading to a simply supported one-way slab element (Fig. 67). The load was applied using one or two hydraulic cylinders, mounted to a rigid overhead beam that was part of a frame tied down to the floor. The load from the cylinders was transferred to two wide-flange beams (W 10 × 45), each 3 ft long, which distributed the load across the width of the specimen as a line load.

The following three types of measurements, in addition to load, were recorded during testing: (1) vertical deflections, (2) end-slip displacements between the deck and concrete interface, and (3) specimen strains. Dial gages were placed underneath the specimen at the center

point and under the two load points to measure the vertical displacements. Dial gages were also used at each end of the specimens to measure any relative horizontal movement (end-slip) between the steel deck and the concrete interface. For the studded specimens, the end-slip measurements were recorded with respect to the base to which the studs were attached. This allowed the determination of potential slip between the concrete and the base plate, as well as between the deck and the concrete interfaces. Strain gages were placed at various positions along the top and bottom of the specimen to determine the surface strains in both the concrete and the steel deck (Fig. 69).

6.3. Analytical Results

The analysis of these vertical load specimens was directed toward the ultimate goal of predicting the failure load for a studded steel deck reinforced composite slab. Two procedures for analysis were utilized. The first was the shear-bond increase approach, which involved a direct relation between the studded and nonstudded results. The second procedure was the contributing forces approach, which was based on end-slip values recorded during testing.

6.3.1. Linear Regression Curves

The shear-bond increase approach utilized the linear regression curves for nonstudded composite slabs presented by Porter, Ekberg, Greimann, and Elleby [14]. The linear regression curves [13] were derived from the American Concrete Institute (ACI) formula

$$\frac{V_{u_{LL}}}{bd} = 1.9\sqrt{f'_c} + 2500\ \rho\ \frac{V_u d}{M_u} \qquad (6\text{-}1)$$

The incorporation of the regression variables α and β, the substitution of the statics relation $M_u = V_u L'$, and the overall division by $\sqrt{f'_c}$ gave

$$\frac{V_{u_{LL}}}{bd\sqrt{f'_c}} = \alpha\ \frac{\rho d}{\sqrt{f'_c}\ L'} + \beta \qquad (6\text{-}2)$$

where α and β are the slope and y-intercept values determined from a linear regression analysis, and $\rho d/\sqrt{f'_c}\ L'$ and $V_{u_{LL}}/bd\sqrt{f'_c}$ are the X and Y variables, respectively. In determining the X and Y variables, the parameters were taken from measured quantities where

$$\begin{aligned} b &= b_b \\ d &= D_{avg} - Y_{sb} \\ p &= A_s/bd \\ V_{u_{LL}} &= P_u/2 \end{aligned} \qquad (6\text{-}3)$$

A correction to the Y variable [13] was applied to take into account the continuous shoring conditions of these specimens

$$V_{corr} = V_{u_{LL}} + 1/2\ \omega\ b_b L \qquad (6\text{-}4)$$

where

$$\omega = 0.359 \text{ psi}$$

The results of these tests are shown in Figs. 70 and 71. It is seen that both the 16-gage and 20-gage nonstudded specimens did plot within a 15% variance interval of the line for the given α and β values. The regression line for the specimens containing 16-gage deck (from previous data [14]) could be slightly inaccurate because those specimens had shear spans greater than 40 in., and therefore did not include the 18-in. range.

The curves for the studded specimens were developed by assuming a mathematical relation between $V_{u_{LL}}$ and L'. The proposed line for specimens containing studs was developed by using a percentage increase the same as was found in this series of tests (Fig. 71). See Table 9 for test results. Figures 72 and 73 show the plotted results of the 20- and 16-gage studded specimens, respectively. In both cases the 60-in. shear span results plotted within a 10% change of the nonstudded regression line. The difference was not great enough to indicate the load increase observed for the studded specimens. The 18-in. shear spans, however, showed a sizeable load increase over the predicted value for the nonstudded specimen, indicating the additional load contribution of the stud.

Conceivably, the shear-bond regression approach could be utilized for each studded and nonstudded specimen series separately to obtain predicted strengths. Figure 74 indicates that the shear-bond approach also appears feasible for the studded specimens.

6.3.2. Contributing Forces Approach

The contributing forces approach examined the forces that restrained the shear span of the studded specimen from sliding out, as compared to

the slippage failure of the nonstudded specimens. This restraining force was assumed to be a combination of shear-bond force (P_{sb}) and stud force (P_{st}). These forces were considered as functions of the end slip.

The contributing forces approach was derived from examining the free body diagram of a shear span (Fig. 75(a)), breaking apart the elements, and separating out the shear-bond force and the stud force components (Fig. 75(b)). The force contribution of these two components was considered as a function of the corresponding end slips, δ_{sb} and δ_{st} (Fig. 75(c)). From experimental data, these end slips were related to the total vertical load (P), equal to twice the vertical shear load (V).

Equation (4-16) was used to develop the theoretical stud load versus end-slip deflection curve. For the studded specimens, δ was the recorded stud end-slip displacement (δ_{st}), and the resulting Q was the internal horizontal compressive force (C_{st} in Fig. 75(b)) due to the stud.

The C_{st} force was related to the vertical load (P_{st}) to permit the direct addition of the shear-bond and stud loads. This relation required the determination of the internal moment arm (C), see Fig. 75(d). From observations of flexural crack progression, at load points near ultimate, the concrete compression zone was approximately 1 in. deep, as measured from the top of the slab. This depth was also confirmed from the strain gage data. By summing moments about A (in Fig. 75(d)) and summing vertical forces

$$P_{st} = \frac{20.0}{L'} C_{st} \qquad (6\text{-}5)$$

To determine C_{st}, the ultimate shear load of the stud must also be calculated. The ultimate shear capacity of the stud was determined by Equation (4-15).

In general, there are two reductions which, in applicable situations, will decrease the ultimate shear capacity of the stud (Q_u), first, a reduction due to the distance of the stud from the free edge when the load is in the direction of the free edge [37]; secondly, an AISC [25] reduction due to the placement of the stud in a down corrugation when the shearing force is parallel to the longitudinal direction of the corrugation. These two reductions should also be considered in determining the C_{st} force from Equation (4-15).

By taking the shear-bond load (P_{sb}) from the load versus end-slip deflection curves for nonstudded specimens and the P_{st} load from Equation (6-5), the predicted ultimate load $P_{calc} = P_{sb} + P_{st}$ was calculated. The comparison of the calculated load to the actual load of the specimens is shown in Table 10 and can be seen as reasonably close.

6.4. Behavior

6.4.1. Crack Patterns

The crack patterns observed during testing were similar for all specimens. Initially, flexural cracks developed at uniform intervals along the length. At or near first recorded end slip, the cracks near the points of load began progressing diagonally towards the center of loading. After first recorded end slip, the cracks within the constant moment region stopped progressing, and the diagonal shear cracks

continued propagating towards the center of loading. As end slip continued to increase, the diagonal cracks also widened and, at test termination, were observed to be quite wide.

6.4.2. End-Slip Behavior

A typical load versus shear-bond end-slip curve (Fig. 76) shows that at an end-slip displacement corresponding to the maximum load of the studded specimen, the corresponding nonstudded specimens have generally not reached ultimate.

6.5. Shear Span Influence

6.5.1. General Remarks

The shear span influence was important in determining the behavior after ultimate load had been reached. For the 18-in. shear span, the drop of load after ultimate was relatively uniform. For the 60-in. shear span, there was a sharp drop in load, followed by a constant load level. Continued displacement resulted in a uniform decrease in load.

6.5.2. Pushout Tests--Beam Series

6.5.2.1. Description of Tests

To examine the effect of the shear span of the shear-bond mode of failure, a series of pushout tests were designed and tested (Fig. 77). The pushout specimens were made of 20-gage Deck Type 1 (Fig. 3). Several groups of specimens were cast using the combinations of three variables, i.e.,

- Length (22 in. and 63 in.).
- Number of deck corrugations (1 or 2).
- With or without studs.

Table 11 lists all pushout specimens of this series tested and their variables. Each specimen contained dial and strain gages spaced at certain intervals along the entire length. Loading was applied longitudinally. The specimen was clamped at one end and rested on a roller support at the other (see Fig. 77). Load was applied at the centroid of the composite section by a hydraulic ram. A load cell was used to record the loads with the hydraulic pressure readings used as a check.

6.5.2.2. Pushout Tests

All 60-in. (shear span) specimens exhibited a progressive wave action recorded by the dial gages and deck strain gages. Figure 78 shows a typical load-displacement graph for a nonstudded 60-in. specimen. The studded 60-in. specimens had similar load-displacement curves up to the point of shear-bond failure over the entire length of the specimen. The studded specimens achieved a higher load, which is also reflected in the vertical load testing. Slip occurred too rapidly in the 22-in. long specimens for the progressive shear-bond failure mechanism to be detected.

6.5.3. Incremental Contribution Along Shear Span

The vertically loaded one-way slab element tests indicated that the shear-bond force was related to the relative displacement (δ) between the deck and the concrete at the interface. The relative displacement at any cross section was noted to be a function of the deck and concrete strains at that cross section. The pushout series conducted in conjunction with

the vertically loaded slab elements indicated also an incremental force contribution along the shear span length.

At initial loading (Phase I in Fig. 77), the deck strains were the largest at end A and decreased to zero at X_o. Further loading led to Phase II where the relative displacements between end A and x_u were greater than δ_{ui}, which was the relative displacement at the maximum V_i, the individual embossment load. Between X_u and X_o, the embossments possessed increasing load potential since they had not reached their ultimate capacity. The section of the specimen between X_o and end B had not undergone any relative displacement and was not resisting any load. At Phase III, the ultimate load (V_u) had already been reached. The relative displacements were such that the ultimate capacity at each contributing embossment had been exceeded progressively towards end A. After the end embossments had reached their ultimate capacity, the load decreased gradually.

For the 18-in. shear span specimens, the embossments at the end of the shear span had already undergone sizeable relative displacements when the embossments near the point of loading reached their ultimate capacity. Therefore, the transition phase that occurred within the 60-in. shear span lengths did not occur in the 18-in. lengths.

6.6. Summary and Conclusions

Initial test results indicated that the addition of end studs increased the flexural load capacity of one-way steel deck reinforced slabs by 10 to 30%. The nonstudded specimens ultimately failed from

a loss of interfacial force in the shear span. The studded specimens ultimately failed with the tearing of the deck near the stud. An examination of the behavioral characteristics revealed that the load capacity increase was due to the additional stud resistance that developed as the concrete within the shear span attempted to override the deck embossments.

Two analysis procedures were utilized, a contributing forces approach and a shear-bond approach. The contributing forces approach was found to be a potential analysis procedure. Further development of the approach into useful design criteria would require: (1) a thorough understanding of the deck and concrete forces at the load corresponding to the deck tearing, and (2) a determination of internal horizontal force versus end-slip relationships for a nonstudded specimen.

The shear-bond increase approach assumed that, at the ultimate load of a studded specimen, the shear-bond load capacity is at a maximum. The results from the shear-bond increase approach indicated that the studded beam load capacity cannot be predicted directly from the load increase observed. Two types of shear-bond regression curves, one for studded and one for nonstudded, were found. The feasibility of utilizing a shear-bond approach for studded specimens was shown. However, further investigation is needed to develop design recommendations for this approach.

6.7. Recommendations

More pushout tests are needed for the further development of the contributing forces approach. These pushout tests would aid in developing the distribution of forces and displacement along the shear spans. Determining the relative displacements along the length of a pushout specimen, the additional relative displacements due to curvature of a one-way slab could be calculated from flexural beam theory and added to the pushout values. From the development of a general embossment load versus relative displacement curve, the horizontal force could be determined. The development of this load-displacement curve is recommended.

In addition, the shear-bond regression approach for studded specimens should be utilized on other slab types to verify the findings of this research. Final design recommendations are needed for the shear-bond strength of studded specimens.

7. APPENDIX B: PUSHOUT TESTS

7.1. Introduction

Based on the assumptions and analysis discussed in Section 4.2.1, pushout specimens were designed to simulate the transfer of forces from the framing members to the concrete within the edge zone. Two types of specimens were tested, one with the deck corrugations perpendicular to the direction of the load (see Fig. 55), the other with the corrugations parallel to the direction of the load (see Fig. 54). These two types gave the stiffness and interfacial shear strength transverse and parallel to the corrugations, respectively. The pushout specimens were assumed to adequately reproduce all of the critical forces occurring within the edge zone and as discussed in Section 4 (see Figs. 48-53).

7.2. Description of Pushout Specimens and Discussion of Results

Three series of pushout tests were conducted to obtain the stiffnesses and strengths for the various types of deck. The design and testing of the first series was based on pushouts of studded slabs done at Lehigh University [26]. In the Lehigh tests, two reinforced slabs, one studded to each flange of a W-shape column section, were tested simultaneously. The slabs were supported vertically and the W-shape was pushed axially downward to obtain the pushout strengths. The large ductility capacity and containment forces provided by the studs prevented gross deformations of the slabs. However, sufficient containment forces are not present in nonstudded specimens. Once measurable

slip had occurred in either of the nonstudded slabs, brittle behavior at the concrete/deck interface led to gross distortions, and further testing became meaningless. The first series is therefore not reported in any detail, though it proved useful in developing designs and testing procedures which eliminated some of these problems. For example, only one slab was tested at a time in the horizontal position in the second and third series. Table 12 lists the basic design and testing parameters of these two series.

The specimens for the second series (9 specimens) were made using Deck Types 1 and 2, and those for the third series (6 specimens), Deck Types 1 and 4. No pushouts were constructed using Deck Type 3 due to a shortage of that decking. The steel deck used in the pushouts was cut to various lengths and welded along one side to a steel plate to simulate the attachment of the slab to the framing members (see Figs. 54 and 55). The same weld pattern and welding process were used for the pushouts as were used for the slabs. Two pieces of deck panel welded side by side were used for the transverse specimens to include a seam within the specimen. Reinforcing bars were placed over the first up corrugation in each of the transverse specimens in order to strengthen the corner where the load was to be applied.

The concrete for the Series 2 specimens was wet cured for 14 days, due to low concrete strength. Testing was done between 22 and 26 days after casting. The Series 3 specimens were wet cured for 7 days and tested between 64 and 78 days after casting.

The specimens were bolted to the frame illustrated in Fig. 79 for testing. Instrumentation consisted of mechanical dial gages (see

discussion below) and a load cell connected to a data acquisition system (DAS). The DAS continuously displayed the load, which was applied using a hydraulic cylinder and hand pump. The load was applied near the edge of the specimen to simulate the loading condition in the edge zone of the slab.

The transverse pushout specimens in Series 2 made with Deck Type 1 were difficult to test. Cracking of the concrete over the up corrugation nearest the load occurred in every one of these transverse tests (Specimens 2-3, 2-7, and 2-8). This problem was eliminated in Specimens 3-1 and 3-2 (and also Specimen 3-5 and 3-6, presumably) by making the specimens thicker and by placing reinforcing bars near the top surface in the area where the crack had formed in the Series 2 specimens. These changes were assumed not to significantly affect the results.

Twisting of the concrete with respect to the deck and of the specimen with respect to the test frame occurred with varying degrees in all of the pushout tests. There was twisting both about a vertical axis and also about a horizontal axis perpendicular to the direction of the load. This was due to the eccentricities between the applied load and the line of action of the resisting forces. The twisting of the specimen about a horizontal axis (characterized by uplift of the corner nearest the load) was minimized by applying the load as near to the bottom of the specimen as was practical (typically about three-fourths of an inch), the position suggested in Fig. 53 (see Section 4.2.1.1). Vertical movements were measured using one (Series 2) or two (Series 3) mechanical dial gages.

An attempt was made in the Series 3 pushouts to minimize the twisting about a vertical axis as well. Two mechanical dial gages were used to measure the horizontal displacements near each side of the specimen and the point of load application was adjusted so that these displacements would remain approximately equal. This procedure was partially successful, although some twisting was evident. In neither Series 2 nor 3, however, was there substantial twisting until the maximum load had been reached, i.e., the line of action of the resisting forces did not move far vertically or horizontally from the centroid of the weld group until the interfacial shear strength had been exceeded. The twisting caused by the eccentricity in load application was assumed not to have any significant effect on the basic results (initial stiffness and maximum strength) of the pushout tests.

The initial stiffness and ultimate load of each of the tests are also listed in Table 12. The results were sometimes quite erratic. To follow a reasonably consistent pattern, the stiffness of a pushout was determined by doing a linear regression analysis on the load-slip data through 0.005 in. The value 0.005 in. was chosen because the slip in the full-scale tests did not typically exceed this in the initial linear range.

Since two pushout specimens were usually tested for each type of deck, the initial stiffnesses of similar tests were averaged using the formula

$$K_{average} = \frac{2}{\frac{1}{K_1} + \frac{1}{K_2}} \qquad (7\text{-}1)$$

where all the K's are in units of KIPs per inch per inch. The ultimate strength values, Q_p and Q_t, were obtained by using the formula

$$Q_{average} = \frac{Q_1 + Q_2}{2} \qquad (7\text{-}2)$$

where each Q value was obtained by dividing the maximum load of each specimen by the length (in feet) of that specimen. These average initial stiffnesses and ultimate strengths are listed in Table 5. Pushout Specimens 2-3, 2-7, and 2-8 were not included in the values given in Table 5 due to the premature cracking problem discussed earlier. Specimen 2-6 was also not included because the results of that test (compared to Specimen 2-5) suggested the specimen was too narrow to effectively represent the edge zone.

7.3. Recommendations

The predictive equations in Section 4 were developed under the assumption that reasonable values for initial stiffness and interfacial shear strength of a given type of deck could be obtained by testing appropriate pushout specimens. While preliminary results look promising, the values from individual tests were not always reasonably consistent. An attempt should be made to further refine the design and testing of the pushout specimens and thereby eliminate large variations in the values obtained. A specimen design that would allow application of the load closer to the bottom of the specimen might prove especially advantageous, as would a testing frame that allowed continuous adjustment

of the point of load application. Further testing should also be done to determine the effect of changing various specimen and testing parameters such as effective length, effective width, thickness, concrete strength, location of load, and any methods for controlling twisting and/or uplift that might be employed. A biaxial load condition for combined loading and a twisting strength determination for pushout specimens should also be explored.

8. ACKNOWLEDGMENTS

This investigation into the behavior of composite steel deck diaphragms was supported by the Engineering Research Institute of Iowa State University with funds provided by the National Science Foundation, Grant No. ENV75-23625. The author wishes to thank those manufacturers who supplied materials and technical assistance for this investigation. The following manufacturers are especially acknowledged: H. H. Robertson Company, Mac-Fab Products, Inc., Nelson Stud Welding Company (a United-Carr Division of TRW, Inc.), and The Fluorocarbon Company.

This author extends special thanks to his co-major professors, Drs. M. L. Porter and L. F. Greimann, for their encouragement, patience, and many helpful suggestions. A special thanks also goes to Doug Wood for all his help during this project. In addition, appreciation is expressed to V. E. Arnold, G. L. Krupicka, D. J. Brangwin, and Aziz Sabri for their contributions to this research, and also to the many hourly employees for their help during various phases of the project.

Very special thanks go to my wife, Karen, and daughters, Katherine and Rebecca, for their patience and continued love despite my absence from family life during a good portion of the past year.

9. REFERENCES

1. Nilson, A. H. "Shear Diaphragms of Light Gage Steel." Journal of the Structural Division, ASCE 86, No. ST11 (November 1960), 111-140.

2. Nilson, A. H. "Diaphragm Action of Light Gage Steel Construction." AISI Regional Technical Paper (1960).

3. Nilson, A. H. and Ammar, A. R. "Finite Analysis of Metal Deck Shear Diaphragms." Journal of the Structural Division, ASCE 100, No. ST4 (April 1974), 711-726.

4. Ammar, A. A. and Nilson, A. H. "Analysis of Light Gage Steel Shear Diaphragms, Part I." Department of Structural Engineering, Research Report 350, Cornell University (August 1972).

5. Ammar, A. A. and Nilson, A. H. "Analysis of Light Gage Steel Shear Diaphragms, Part II." Department of Structural Engineering, Research Report 351, Cornell University (August 1973).

6. Luttrell, L. D. "Strength and Behavior of Light Gage Steel Shear Diaphragms." Department of Structural Engineering, Cornell Engineering Research Bulletin No. 67-1, Cornell University (July 1967).

7. Luttrell, L. D. "Structural Performance of Light Gage Steel Diaphragms." Department of Structural Engineering, Research Report 319, Cornell University (August 1965).

8. Apparao, T. V. "Tests on Light Gage Steel Diaphragms." Department of Structural Engineering, Research Report 328, Cornell University, (December 1966).

9. Porter, M. L. and Ekberg, C. E., Jr. "Investigation of Cold-Formed Steel-Deck-Reinforced Concrete Floor Slabs." Proceedings of First Specialty Conference on Cold-Formed Steel Structures, Department of Civil Engineering, University of Missouri-Rolla (August 19-20, 1971).

10. Porter, M. L. and Ekberg, C. E., Jr. "Summary of Full-Scale Laboratory Tests of Concrete Slabs Reinforced with Cold-Formed Steel Decking." Preliminary Report, International Association for Bridge and Structural Engineering, Ninth Congress, Zurich, Switzerland (May 8-12, 1972).

11. Porter, M. L. Commentary on the Tentative Recommendations for the Design of Composite Steel Deck Slabs. Manual. Washington, D.C.: American Iron and Steel Institute (December 1974).

12. Porter, M. L. and Ekberg, C. E., Jr. "Design vs Test Results for Steel Deck Floor Slabs." Proceedings of Third International Specialty Conference on Cold-Formed Steel Structures, University of Missouri-Rolla (1975).

13. Porter, M. L. and Ekberg, C. E., Jr. "Design Recommendations for Steel Deck Floor Slabs." Journal of the Structural Division, ASCE 102, No. ST11, Proc. Paper 12528 (November 1976), 2121-2136.

14. Porter, M. L., Ekberg, C. E., Jr., Greimann, L. F. and Elleby, H. A. "Shear-Bond Analysis of Steel-Deck-Reinforced Slabs." Journal of the Structural Division, ASCE 102, No. ST12, Proc. Paper 12611 (December 1976), 2255-2268.

15. Porter, M. L. and Ekberg, C. E., Jr. "Behavior of Steel-Deck Reinforced Slabs." Journal of the Structural Division, ASCE 103, No. ST3, Proc. Paper 12826 (March 1977), 663-677.

16. Bathe, K. J., Wilson, E. L. and Peterson, F. E. "SAP IV Structure Analysis Program for Static and Dynamic Response of Linear Systems." Report No. EERC 73-11. University of California, Berkeley (April 1974).

17. Arnold, V. E., Greimann, L. F. and Porter, M. L. "Pilot Tests of Composite Floor Diaphragms." Engineering Research Institute, Iowa State University, Progress Report, ERI-79011, Ames, Iowa (September 1978).

18. Clough, R. W. and Oenzien, J. Dynamics of Structures. New York: McGraw-Hill, Inc. (1975).

19. Brangwin, D. J. "Interfacial Shear of Composite Floor Diaphragms." Unpublished Master's thesis. Iowa State University, Ames (1979).

20. Bresler, B. "Behavior of Structural Elements." In Building Practices for Disaster Mitigation, National Bureau of Standards Building Science Series 46. Washington, D.C.: U.S. Department of Commerce (February 1973), 286-351.

21. Department of the Army, Navy, and the Air Force. Seismic Design of Buildings. Army TM5-809-10. Washington, D.C.: U.S. Government Printing Office (April 1973).

22. Timoshenko, S. and Woinowsky-Krieger, S. Theory of Plates and Shells. 2nd Ed. New York: McGraw-Hill Book Company, Inc. (1959).

23. Timoshenko, S. and Goodier, J. N. Theory of Elasticity. 2nd Ed. New York: McGraw-Hill Book Company, Inc. (1951).

24. Ellifritt, D. S. and Luttrell, L. D. "Strength and Stiffness of Steel Deck Shear Diaphragms." Proceedings of First Specialty Conference on Cold-Formed Steel Structures, Department of Civil Engineering, University of Missouri-Rolla (August 19-20, 1971).

25. American Institute of Steel Construction, Inc. "Specification for the Design, Fabrication and Erection of Structural Steel for Building." New York: AISC (1978).

26. Ollgaard, J. G., Slutter, R. G. and Fisher, J. W. "Shear Strength of Stud Connectors in Lightweight and Normal-Weight Concrete." AISC Engineering Journal, American Institute of Steel Construction, 8, No. 2 (April 1971), 55-64.

27. American Concrete Institute. Building Code Requirements for Reinforced Concrete. (ACI Standard 318-77). Detroit, Michigan: American Concrete Institute (1977).

28. Cardenas, A. E., Hanson, J. M., Corley, W. G. and Hognestad, E. "Design Provisions for Shear Walls." Journal of the American Concrete Institute, Proceedings 70, No. 3 (March 1973), 221-230.

29. Grant, J. A., Fisher, J. W. and Slutter, R. G. "Composite Beams with Formed Steel Deck." AISC Engineering Journal, American Institute of Steel Construction, First Quarter (1977), 24-43.

30. Blodgett, O. W. "Report on Proposed Standards for Sheet Steel Structural Welding." Welding Journal, 57, No. 4 (April 1978), 15-24.

31. Brockenbrough, R. L. and Johnston, B. G. USS Steel Design Manual. Pittsburgh, Pennsylvania: United States Steel Corporation (1974).

32. Ellifritt, D. S. and Luttrell, L. D. "Strength and Stiffness of Steel Deck Subjected to In-Plane Loading." West Virginia University Civil Engineering Studies Report 2011, West Virginia University, Morgantown, West Virginia (1968).

33. Steel Deck Institute. Tentative Recommendations for the Design of Steel Deck Diaphragms. Westchester, Illinois: The Steel Deck Institute (October 1972).

34. Easley, J. T. "Buckling Formulas for Corrugated Metal Shear Diaphragms." Journal of the Structural Division, ASCE 101, No. ST7, Proc. Paper 11429 (July 1975), 1403-1417.

35. Davies, M. J. "Calculation of Steel Diaphragms Behavior." Journal of the Structural Division, ASCE 102, No. ST7 (July 1976), 1431-1445.

36. Krupicka, Gary L. "The Behavior and Analysis of Steel-Deck-Reinforced Concrete Slabs with End-Span Studs." Unpublished Master's Thesis, Iowa State University, Ames, (1979).

37. Bryan, E. R. The Stressed Skin Design of Steel Buildings. London, England: Crosly Lockwood Staples (1973).

10. TABLES

Table 1. Failure modes for composite diaphragms.

1. Composite Diaphragm
    a. Shear strength
        1. Diagonal tension
        2. Parallel to deck corrugations
    b. Stability failure
    c. Localized failure
2. Deck/Concrete Interface
    a. Interfacial shear parallel to the corrugations
    b. Interfacial shear perpendicular to the corrugations
        1. Pop up (overriding)
        2. Deck fold-over
3. Diaphragm/Edge Member Interface
    a. Arc spot welds
        1. Shearing of weld
        2. Tearing and/or buckling of deck around weld
    b. Concrete rib
    c. Studs (or other shear connectors)
        1. Shearing of stud
        2. Shear failure of concrete around stud

Table 2. Summary of parameters for slab specimens.

Slab Number	Concrete Parameters			Steel Deck Parameters				Connections Per Side
	Nominal Thickness (in.)	Actual Thickness[a] (in.)	f'_c (psi)	Deck Type[b]	Thickness (in.)	Yield Strength (ksi)	Ultimate Strength (ksi)	
1	5 1/2	5.38	5634	1	0.034	41.7	53.4	30 studs
2	5 1/2	5.50	5250	1	0.034	41.7	53.4	30 studs
3	5 1/2	5.65	4068	1	0.034	41.7	53.4	60 welds
4	5 1/2	5.28	3849	1	0.034	41.7	53.4	60 welds
5	3 1/2	3.53	2966	2	0.062	48.2	60.7	30 welds
6	7 1/2	7.44	4549	2	0.062	48.2	60.7	60 welds
7	5 1/2	5.40	5435	3	0.058	49.7	61.1	60 welds
8	5 1/2	5.47	3345	1	0.035	41.7	53.4	4 studs (each N-S side) 6 studs (each E-W side)
9	5 1/2	5.48	5412	4 4 (Pan)	0.058 0.057	51.8 52.4	63.2 64.9	60 welds

[a] Out-to-out thickness.

[b] See Section 2.1 and 3.1.

Table 3. Slips between deck and concrete at load points before and after ultimate.

Slab Number	Slip Perpendicular to Corrugations (in.)		Slip Parallel to Corrugations (in.)	
	Before Ultimate	After Ultimate	Before Ultimate	After Ultimate
1	0.004	0.003	0.005	0.012
2	0.005	0.005	0.002	0.011
3	0.009	0.027	0.001	0.002
4	0.011	0.013	0.001	0.002
5	0.009	0.018	0.002	0.002
6	0.011	0.015	0.006	0.010
7	0.026	0.059	0.004	0.005
8	0.009	0.051	0.003	0.003
9	0.021	0.041	0.004	0.010

Table 4. Summary of experimental results.

Slab Number	Initial Stiffness (KIPs/in.)	V_u (KIPs)	Failure Mode
1	1800	168	Diagonal tension
2	2000	186	Diagonal tension
3	1600	97.8	Interfacial shear
4	1300	87.7	Interfacial shear
5	1700	116	Diagonal tension
6	2600	147	Interfacial shear
7	1500	137	Interfacial shear
8	1100	54.4	Diagonal tension/ shear connector
9	1900	220	Diagonal tension

Table 5. Results from pushouts and stud calculations.

Pushouts

Deck Type	Q_t (KIPs/ft)	Q_p (KIPs/ft)	K_t (KIPs/in./in.)	K_p (KIPs/in./in.)
1	5.45	5.62	47	55
2	11.6	4.98	65	42
3	*	*	*	*
4	9.00	9.05	63	37

Stud Calculations

Slab Number	Q_{ut} (KIPs/Stud)	Q_{up} (KIPs/Stud)	K_t (KIPs/in./in.)	K_p (KIPs/in./in.)
1	19.5	19.5	199	179
2	18.8	18.8	192	173
8	21.1	14.9	29	30

*Values from Deck Type 4 used in calculations.

Table 6. Experimental versus predicted initial stiffness.

Slab Number	Experimental (K/in.)	From Proposed Equations (K/in.)	From Tri-Service Manual Equations (K/in.)
1	1800	3000	4500
2	2000	2900	4300
3	1600	1600	2900
4	1300	1500	2600
5	1700	1400	2100
6	2600	1900	5000
7	1500	1600	4600
8	1100	1100	3400
9	1900	1600	7000

Table 7. Experimental versus predicted ultimate load.

Slab Number	Experimental (KIPs)	Proposed Method[a]			% Error	Tri-Service Manual Equations	% Error
		Mode 1 (Eq. (4-20))	Mode 2 (Eqs. (4-27), (4-28))	Mode 3 (Eqs. (4-34), (4-35))			
1	168	<u>182</u>	---[c]	448	8.3	---	--
2	186	<u>181</u>	---	490	2.7	---	--
3	97.8	166	<u>94.2</u>	145	3.6	104	6.3
4	87.7	148	<u>81.8</u>[d]	145	6.7	93.0	6.0
5	116	<u>115</u>	124	182	0.8	86.9	25.0
6	147	295	<u>124</u>	290	16	204	38.8
7	137	186	<u>164</u>[e]	275	20	123	10.2
8	54.4	146	---	<u>79.7</u>[f]	46	---	--
9	220	247[b]	<u>213</u>[b]	261	3.2	146	33.6

[a] Controlling value is underlined.

[b] Includes strength added by pan; see Section 4.3.2.

[c] Does not apply (see text).

[d] Includes effect of pre-ultimate crack; see Section 4.3.2.

[e] See discussion in Section 4.3.2.

[f] Based on pushout values from pan deck; see Section 4.3.2.

Table 8. Specimen groups for vertical loading.

Group	Specimens	L	Deck Gage
I	1-4	184	20
II	5-8	92	20
III	9-12	73	16
IV	13-15	184	16

Table 9. Vertical loading test results.

Slab Number	L_c (in.)	L' (in.)	P_u (KIPs)	Average % Increase
1	178	60	6.47	9
2	178	60	6.11	
3	178	60	6.58	7.7
4	178	60	7.00	
5	86	18	17.73	
6	86	18	18.73	
7	86	18	28.25	32.5
8	86	18	25.75	
9	67	18	28.75	
10	67	18	28.50	
11	67	18	40.75	30.5
12	67	18	41.50	
13	178	60	9.06	
14	178	60	12.18	24.5
15	178	60	11.68	

Table 10. Comparison of predicted loads to actual loads for vertical loading.

Specimen	P_{calc} (KIPs)	P^{a}_{actual} (KIPs)
3	8.01	8.78
4	8.61	9.20
7	28.77	27.86
8	27.29	26.36
11	48.08	41.37
12	47.68	41.12
14	13.26	14.23
15	12.42	13.75

[a]Dead weight correction has been added to P_u to obtain P_{actual} (see Equation (2)).

Table 11. Pushout specimens tested for vertical loading.

Specimen Number	Composite Length (in.)	Number of Corrugations	Nelson Studs	Number of Dial Gages	Number of Strain Gages
1	63	1	Yes	7	3
2	63	1	Yes	7	3
3	63	1	No	7	3
4	63	1	Yes	7	3
5	63	1	No	7	3
6	63	1	No	7	3
7	63	2	No	7	3
8	63	2	No	7	3
9	22	1	Yes	3	1
10	22	1	No	3	1
11	22	1	Yes	3	1
12	22	1	No	3	1
13	22	1	No	3	1
14	22	1	No	3	1
15	22	1	Yes	3	1
16	22	1	Yes	3	1

Table 12. Design and testing parameters and results of pushout specimens.

Specimen Number	Deck Type	Dimensions (in.)		Load Direction	Thickness (in.)	f'_c	K KIPs/in./in.	P_u (KIPs)
		Parallel	Perpendicular					
2-1	1	36	36	Parallel	5 1/2	2950	168	14.6
2-2	2	30	30	Parallel	7	2950	∞	13.4
2-3	1	36	36	Perpendicular	5 1/2	2950	--[a]	7.8[b]
2-4	1	36	36	Parallel	5 1/2	2950	33	19.1
2-5	2	30	30	Parallel	7	2950	21	11.5
2-6	2	15	30	Parallel	7	2950	45	6.9
2-7	1	18	36	Perpendicular	5 1/2	3197	26	9.5
2-8	1	36	36	Perpendicular	5 1/2	3197	36	13.8
2-9	2	30	30	Perpendicular	7	3197	65	28.9
3-1	1	36	36	Perpendicular	7 1/4	6250	53	16.5
3-2	1	36	36	Perpendicular	7 1/4	6250	43	16.2
3-3	4	36	36	Parallel	7 1/4	6250	35	21.5[b]
3-4	4	36	36	Parallel	7 1/4	6250	39	32.8
3-5	4	36	36	Perpendicular	7 1/4	6250	60	25.5
3-6	4	36	36	Perpendicular	7 1/4	6250	66	28.5

[a]No value calculated.

[b]Premature bearing failure.

11. FIGURES

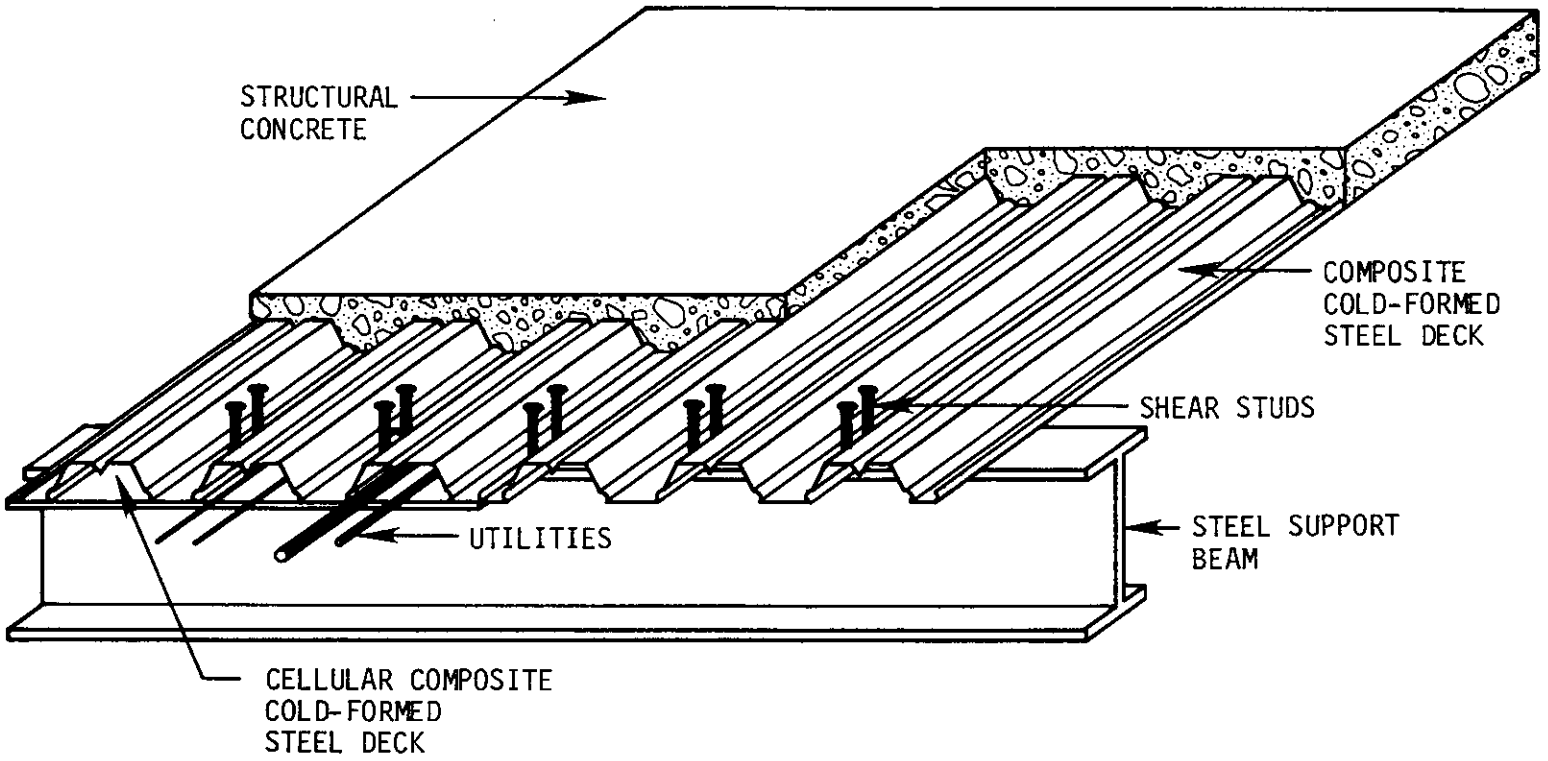

Fig. 1. Typical construction utilizing cold-formed steel decking with composite support beams.

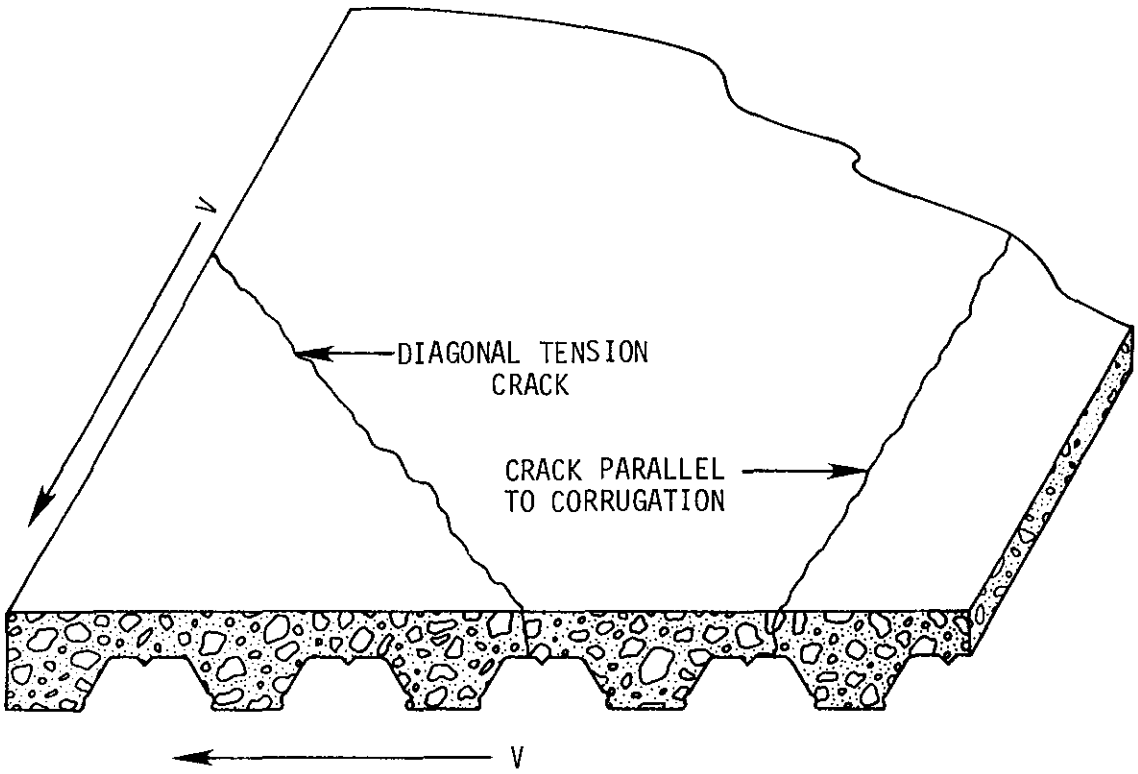

Fig. 2. Failure by shearing of the concrete in a) diagonal tension and b) cracks parallel to the corrugations (Failure Mode 1a-1 and 1a-2 in Table 1).

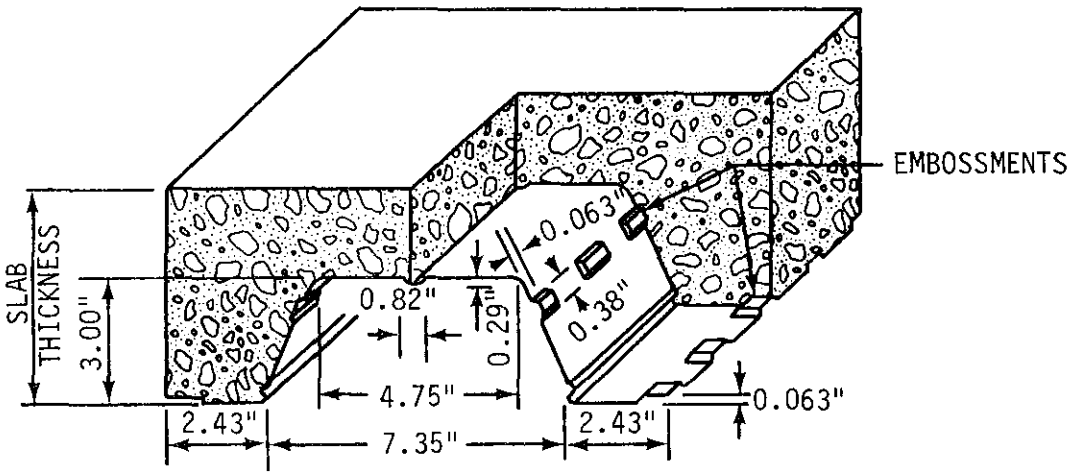

Fig. 3. Typical view of Deck Type 1.

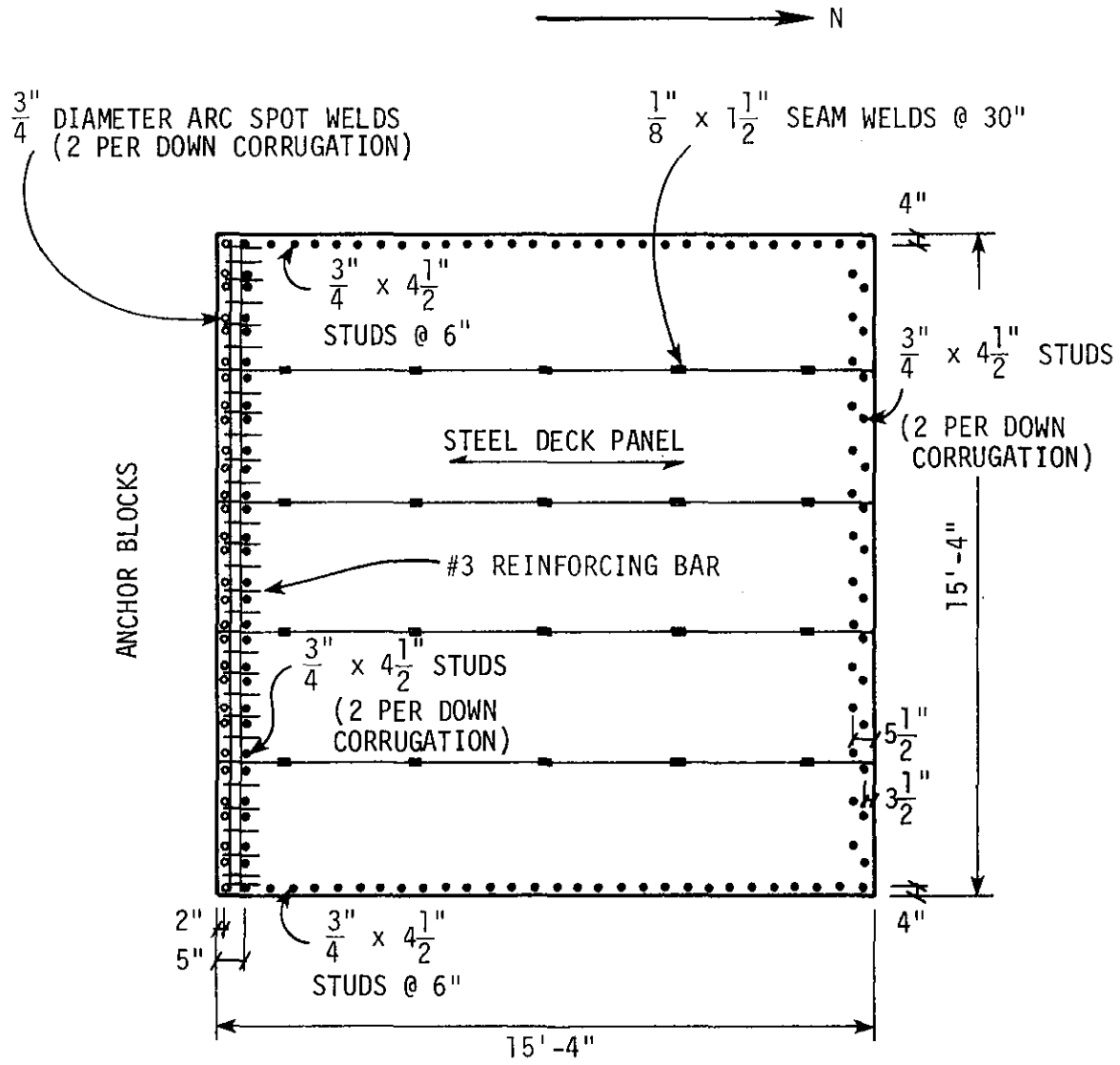

Fig. 4. Detailed plan view of pilot test Specimens 1 and 2.

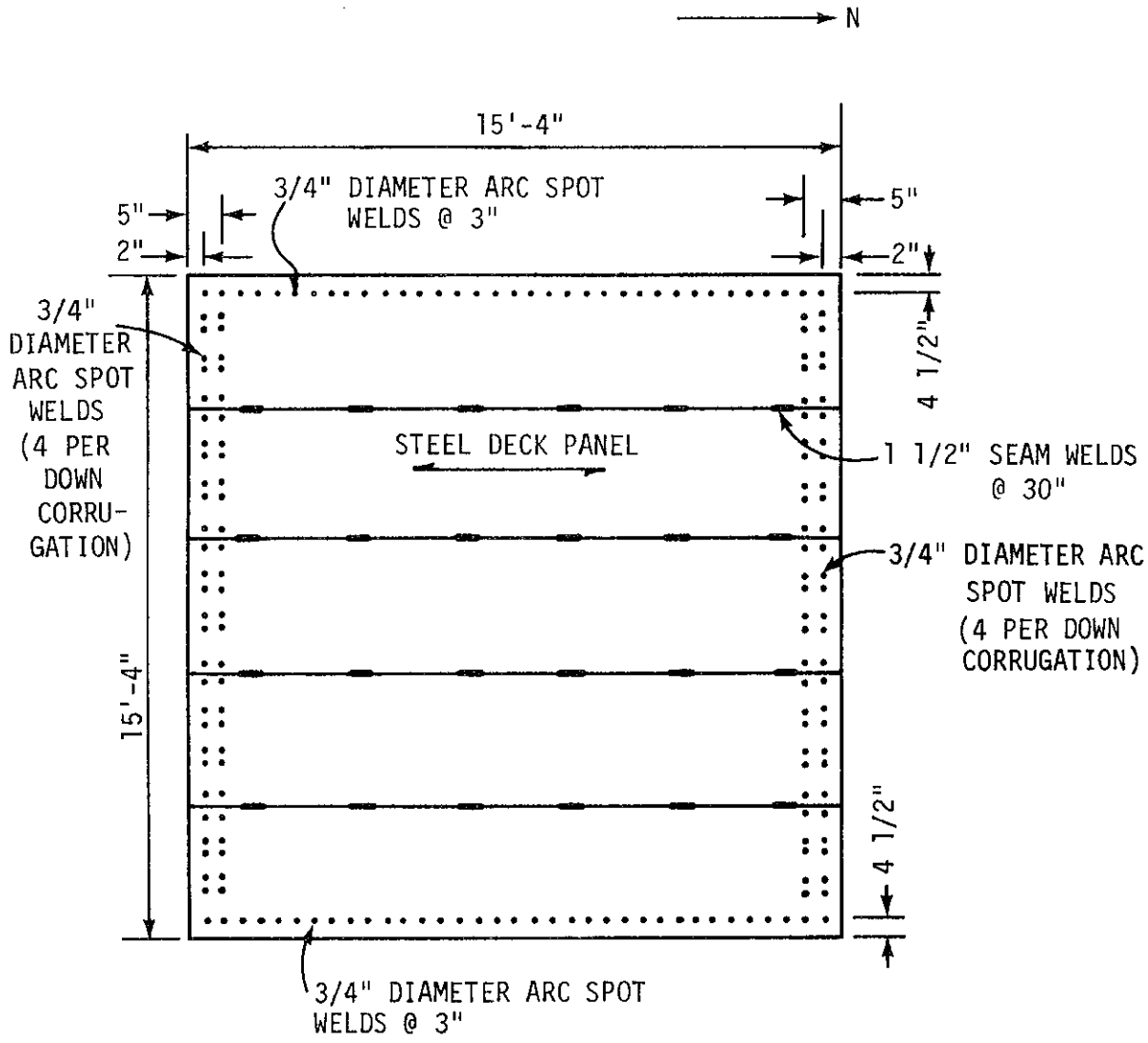

Fig. 5. Plan view of edge fastener layout for Slabs 3, 4, 7 and 9 (Note: decking for Slab 4 is oriented 90 degrees to direction indicated.)

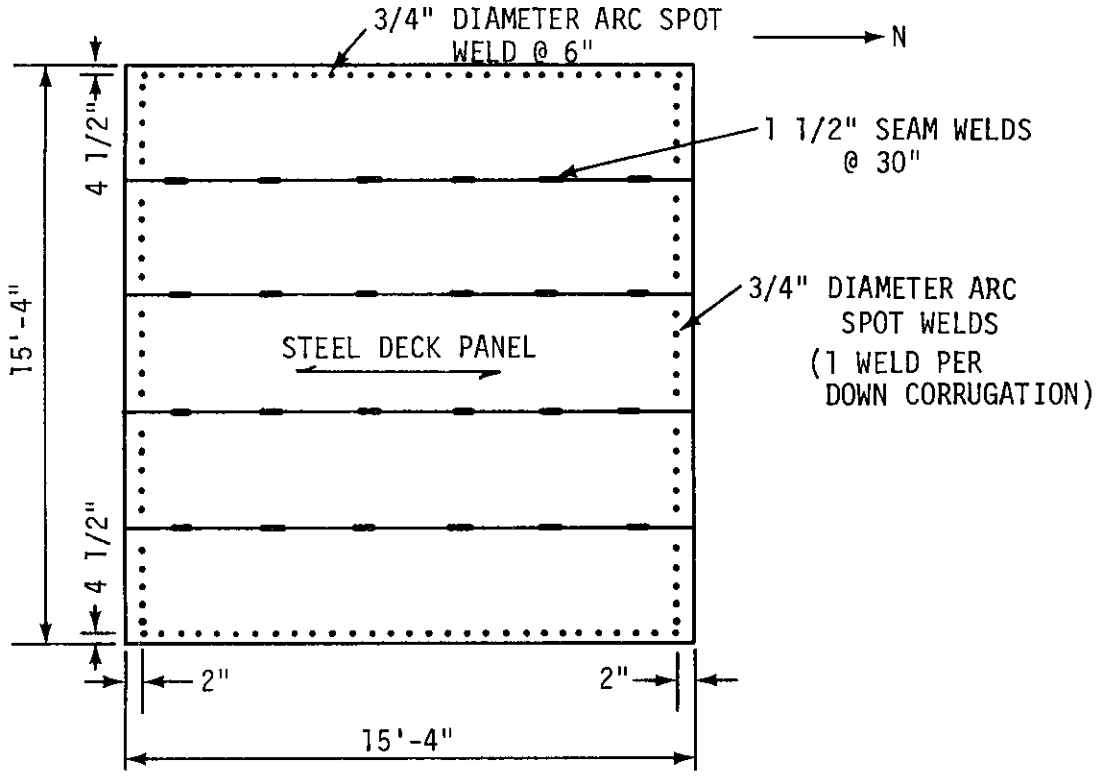

Fig. 6. Plan view of edge fastener layout for Slab 5.

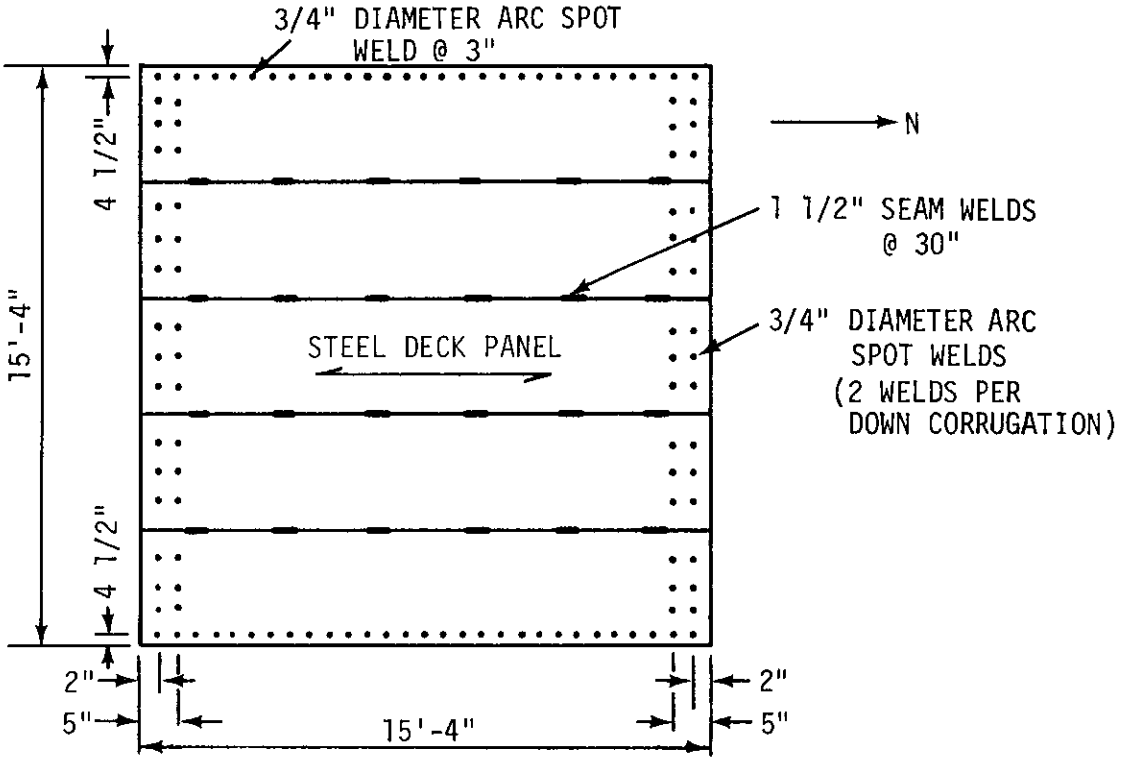

Fig. 7. Plan view of edge fastener layout for Slab 6.

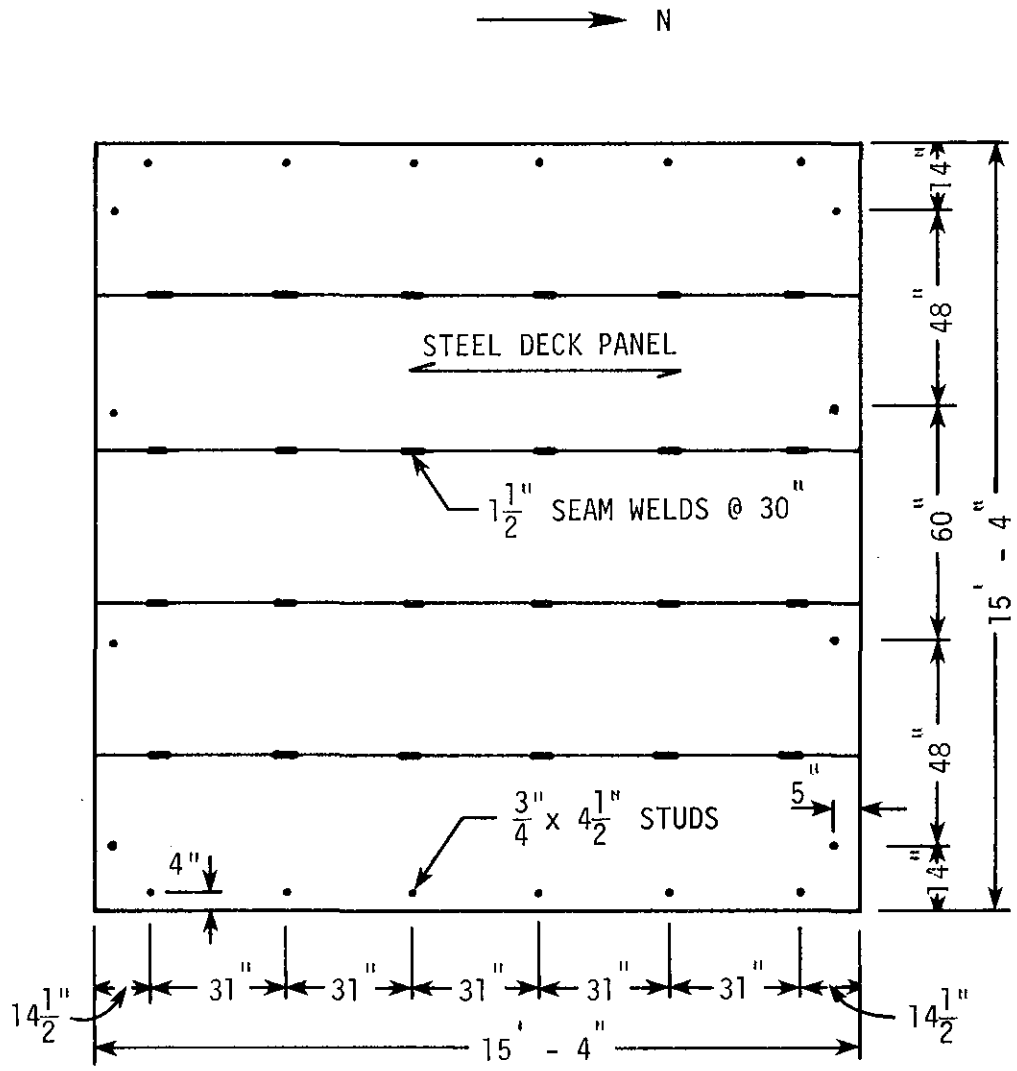

NOTE: STUD SPACING ALONG SOUTH SIDE SAME AS NORTH; SPACING ALONG WEST SAME AS EAST.

Fig. 8. Stud shear connector layout for Slab 8.

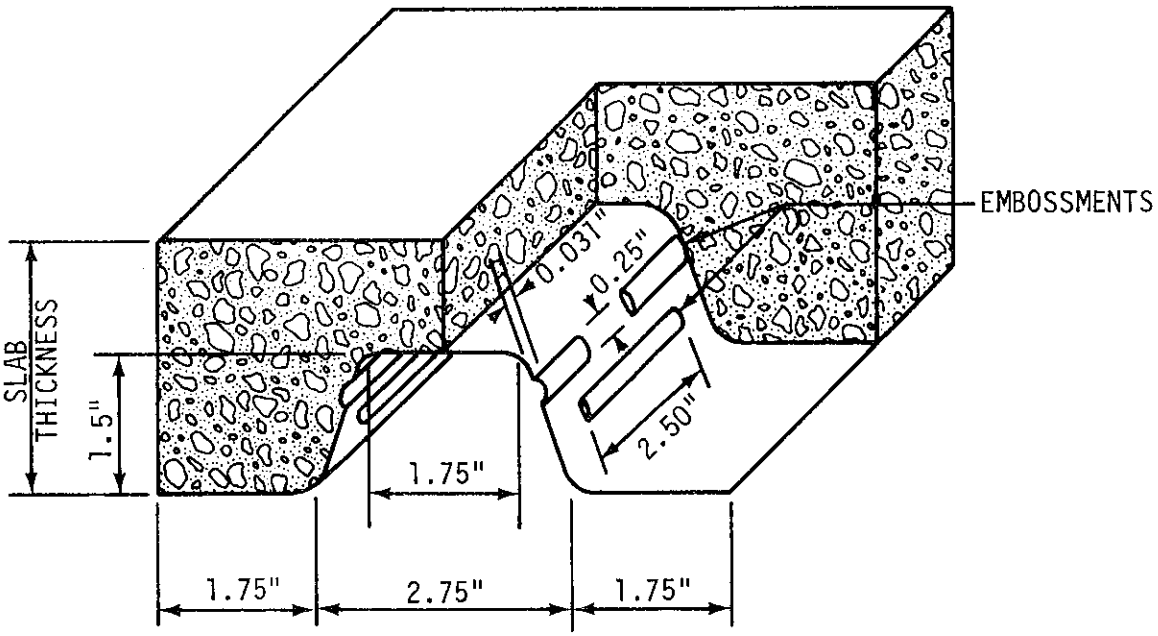

Fig. 9. Typical view of Deck Type 2.

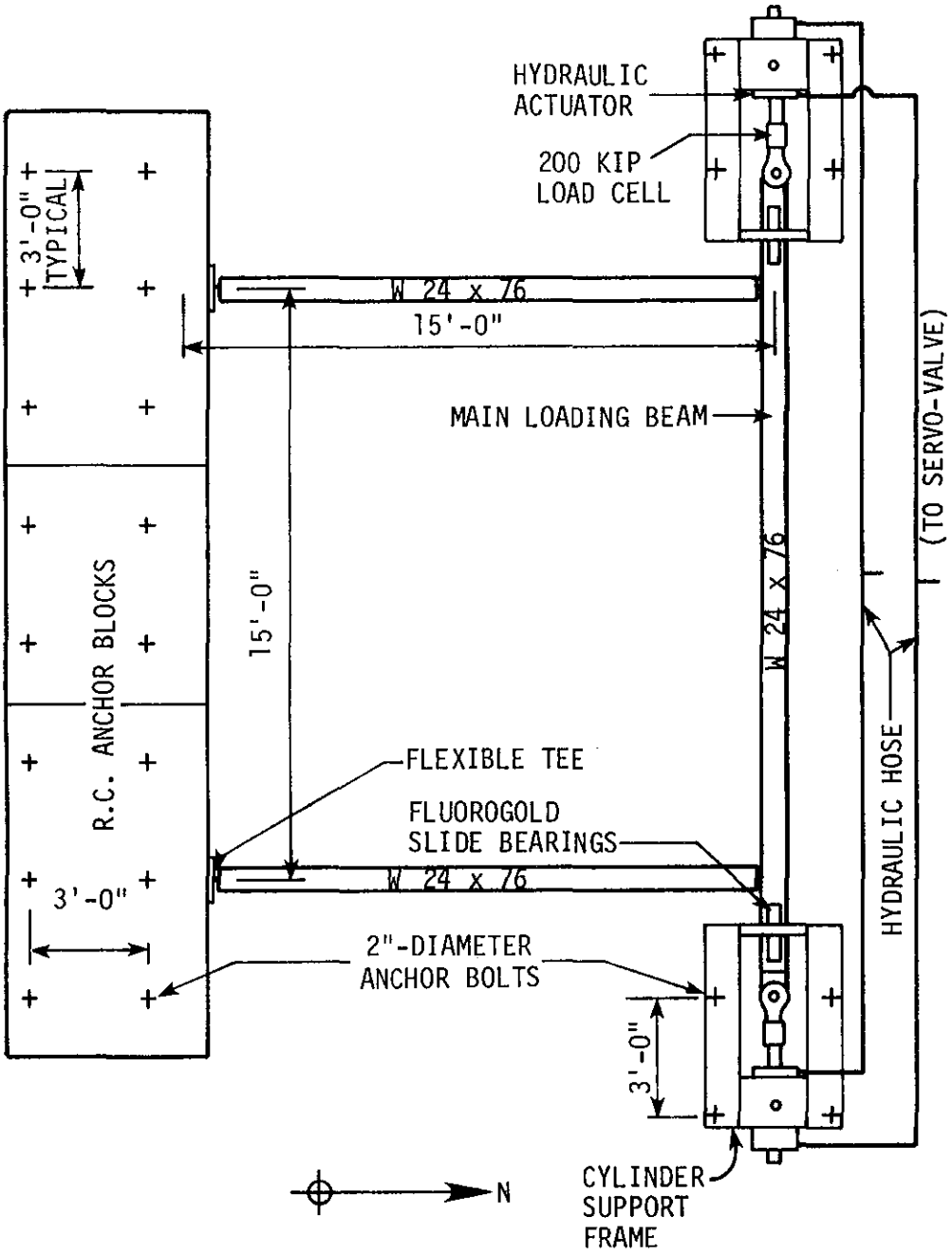

Fig. 10. Diaphragm test frame schematic.

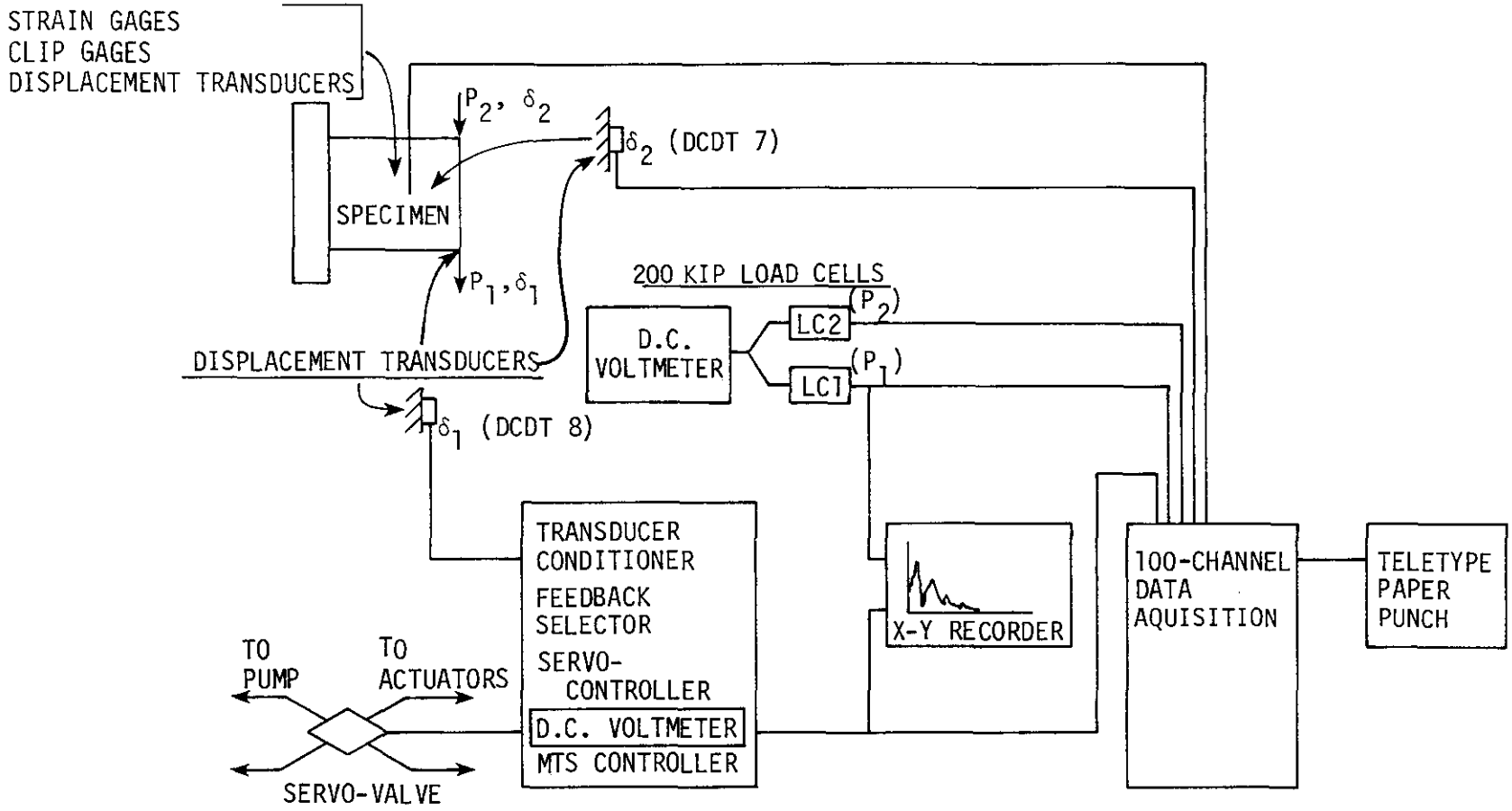

Fig. 11. Servo-hydraulic testing system.

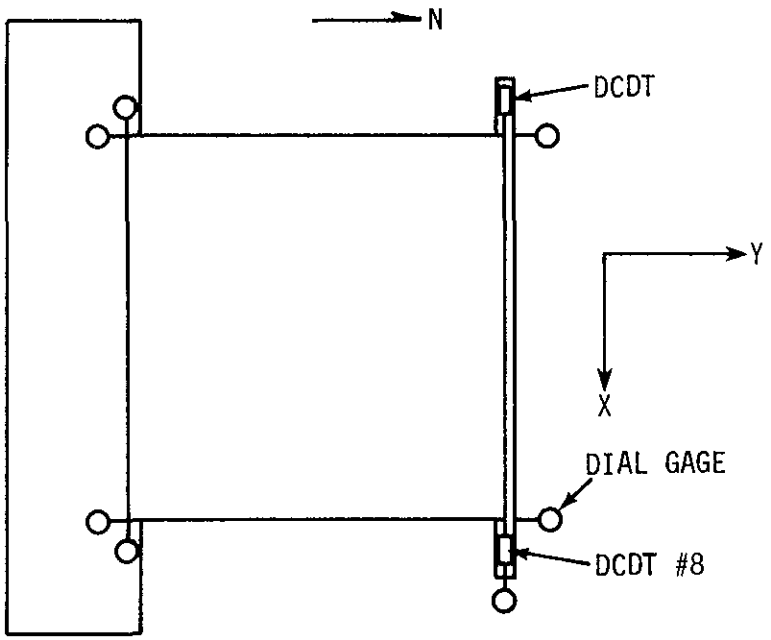

Fig. 12. Location of in-plane (horizontal) displacement gages for all slabs (excluding slip measurement gages).

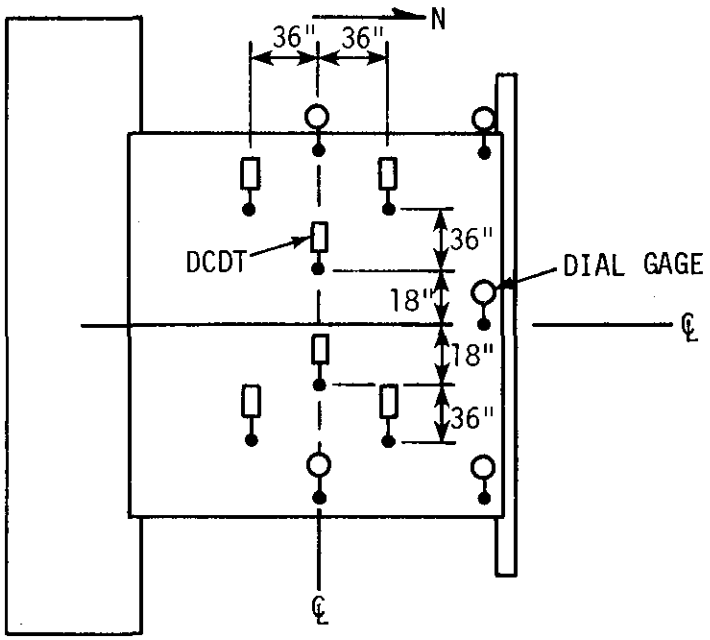

Fig. 13. Location of out-of-plane (vertical) displacement gages for all slabs.

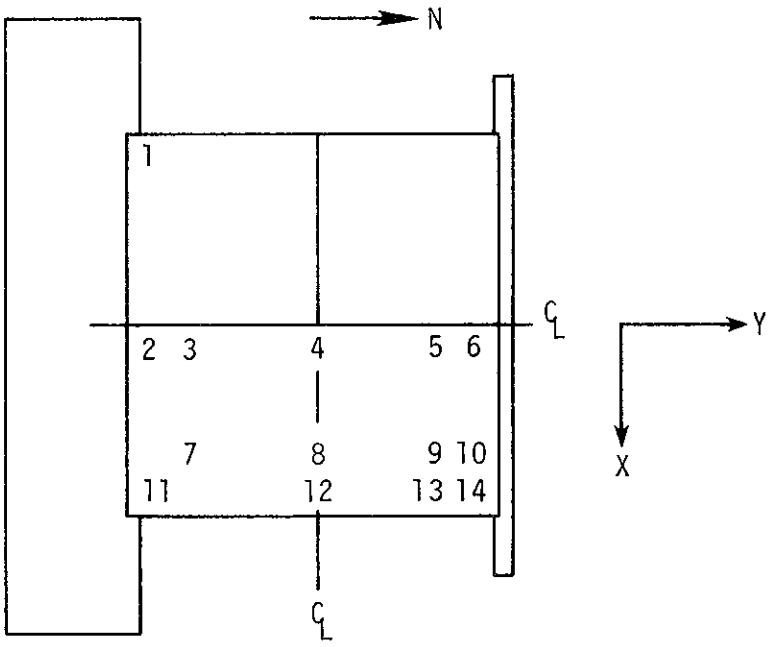

LOCATION / SLAB NUMBER	1	2	3	4	5	6	7	8	9	10	11	12	13	14
1	-	-	R,R'	R,R'	R,R'	-	R,R'	R,R'	R,R'	-	-	-	-	-
2	-	-	R,R'	R,R'	R,R'	-	R,R'	R,R'	R,R'	-	-	-	-	-
3	U	U,U'	-	R,R'	-	U'	-	-	-	-	U,R'	U,U'	-	U,R'
4	U	U,U'	-	R,R'	-	U'	-	-	-	-	U,R'	U,U'	-	U,R'
5	U,R'	U,U'	-	R,R'	-	U'	-	-	-	-	U,R'	U,U'	-	U,U'
6	U,R'	U,U'	-	R,R'	-	U'	-	-	-	-	U,R'	U,U'	-	U,U'
7	-	-	-	R,I,R'	U'	U,I,R'	-	U'	U'	U'	-	U,I,R'	U'	R'
8	-	-	-	R,I,R'	R,I,R'	-	-	R,I,R'	R,I,R'	-	-	-	-	-
9	-	-	-	R,R'	-	R,R'	-	-	R'	-	-	R,R'	-	R,R'

R = ROSETTE ON CONCRETE SURFACE.
R' = ROSETTE ON TOP AND BOTTOM OF STEEL THICKNESS (TOP ONLY ON SLABS 1 AND 2).
U = UNIAXIAL GAGE ON CONCRETE SURFACE.
U' = UNIAXIAL GAGE ON TOP AND BOTTOM OF STEEL THICKNESS.
I = IMBEDMENT GAGE.

Fig. 14. Deck and slab strain gage layout diagram and table.

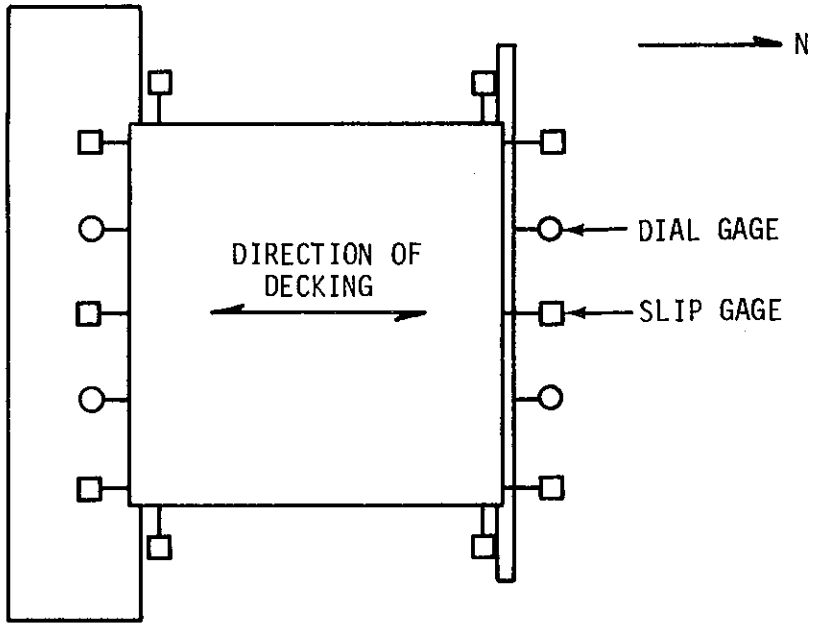

(a) TYPICAL LAYOUT FOR SLABS EXCEPT FOR SLAB 4.

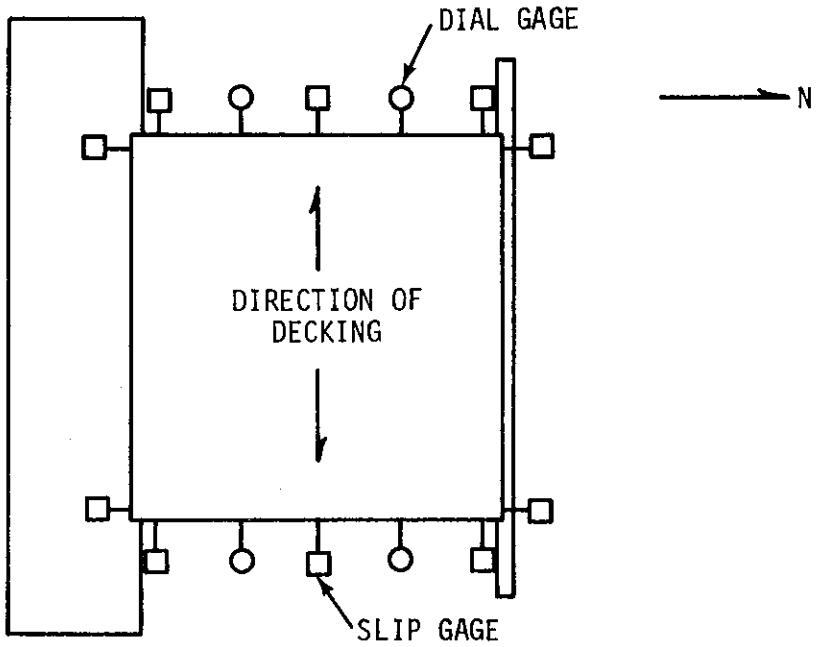

(b) SLAB 4

Fig. 15. Location of slip transducers.

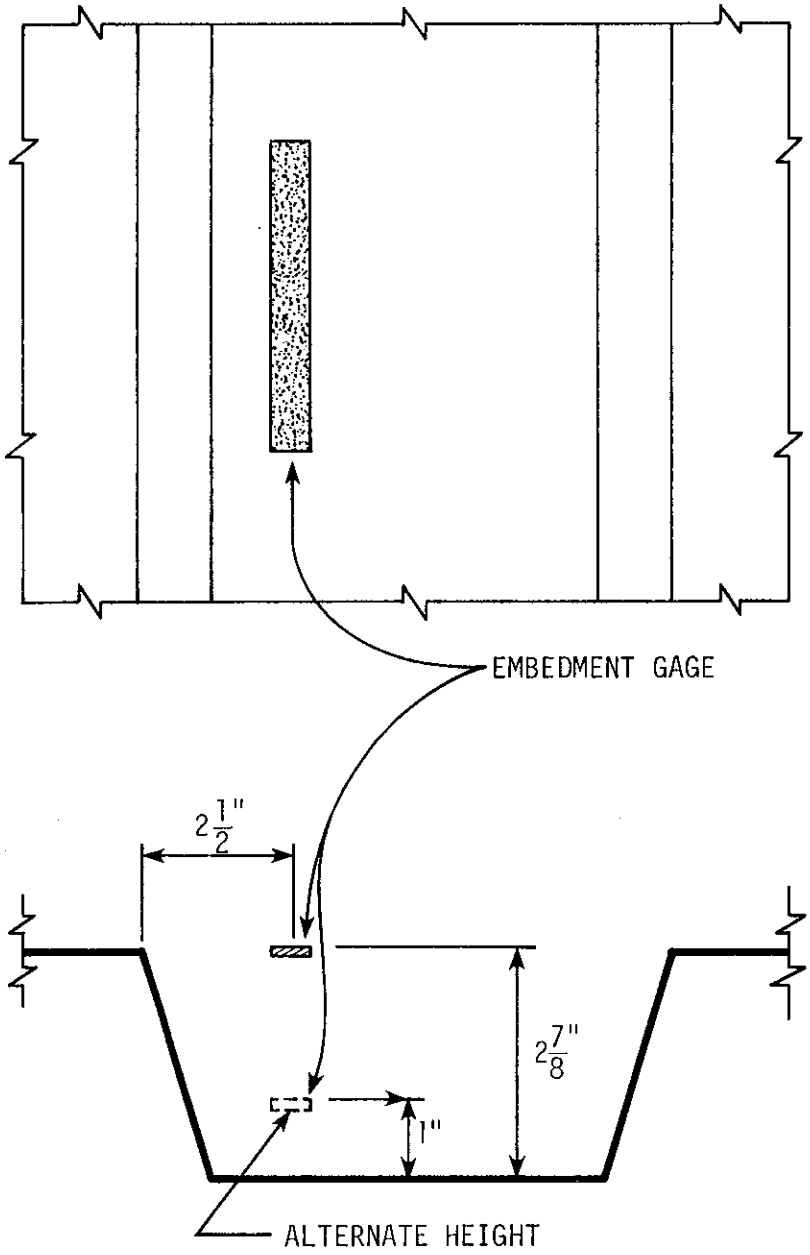

Fig. 16. Typical placement of embedment gages relative to deck cross section.

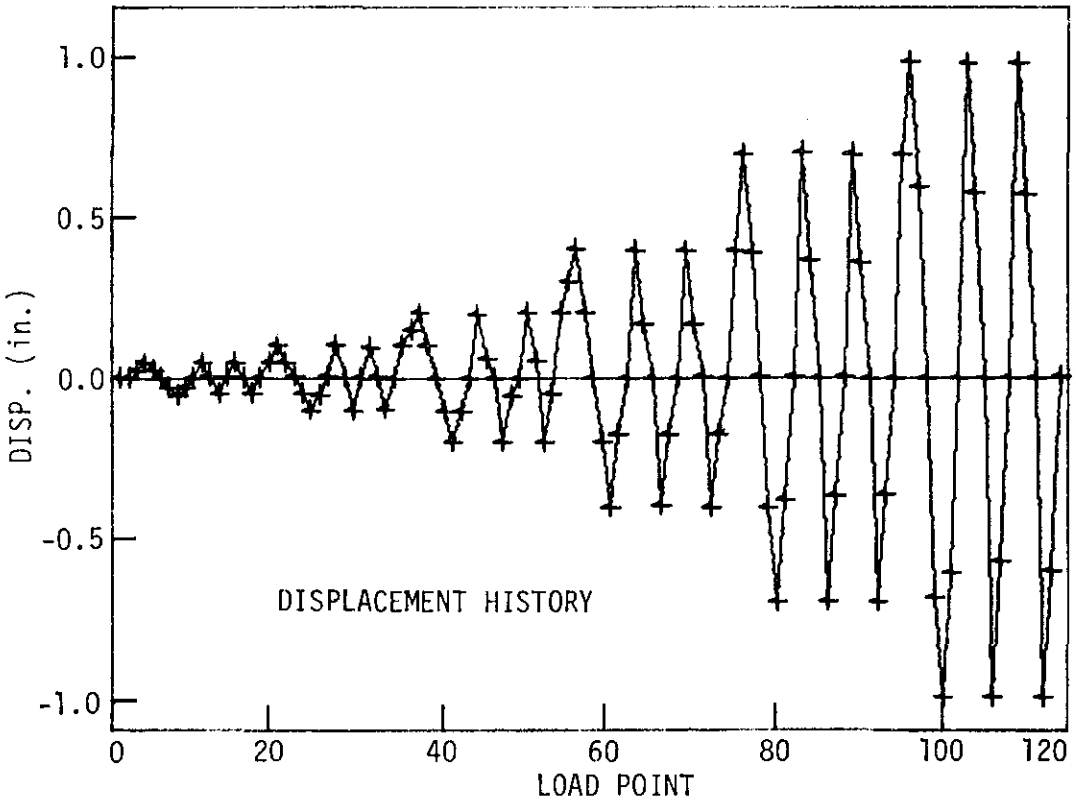

Fig. 17. Typical load-displacement history.

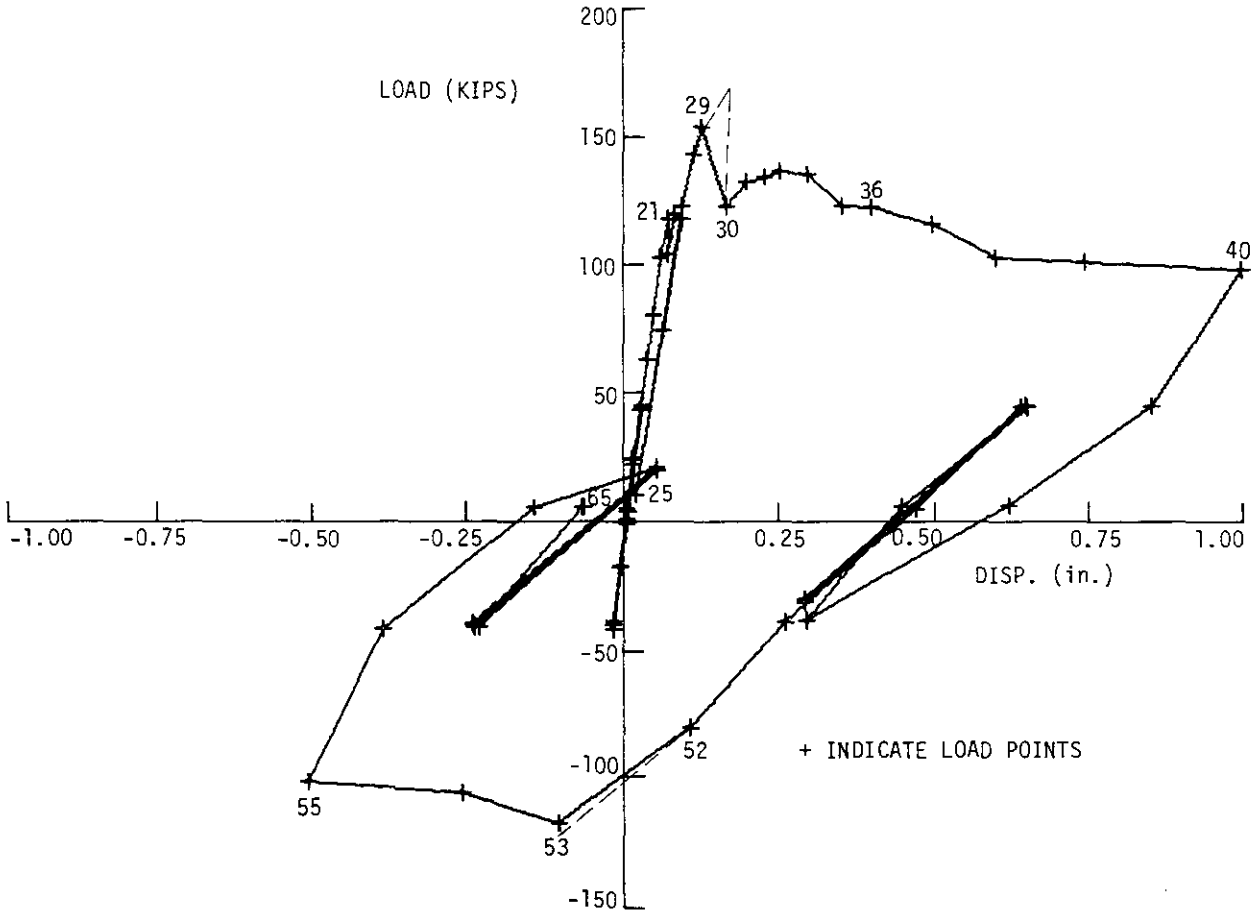

Fig. 18. Load-displacement diagram,Specimen 1.

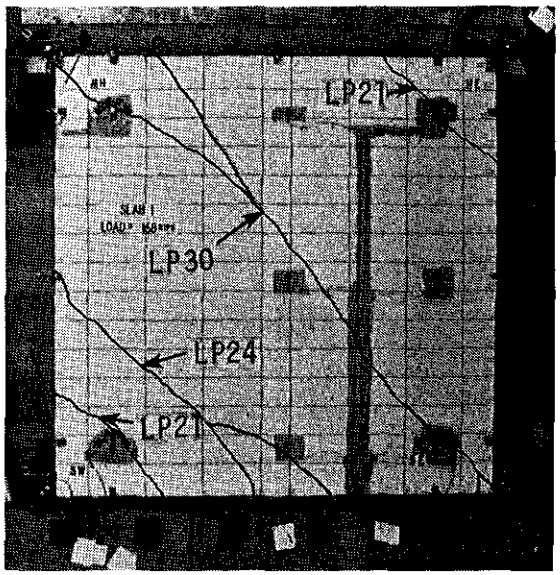

(a) MAXIMUM LOAD (LP 30).

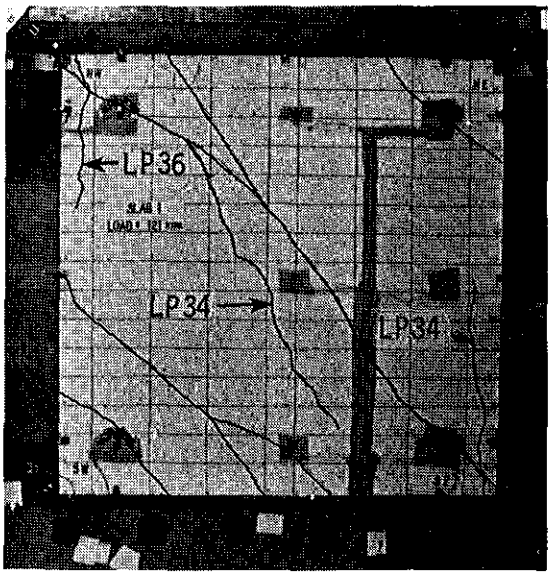

(b) CRACKS PARALLEL TO DECK CORRUGATIONS (LP 36).

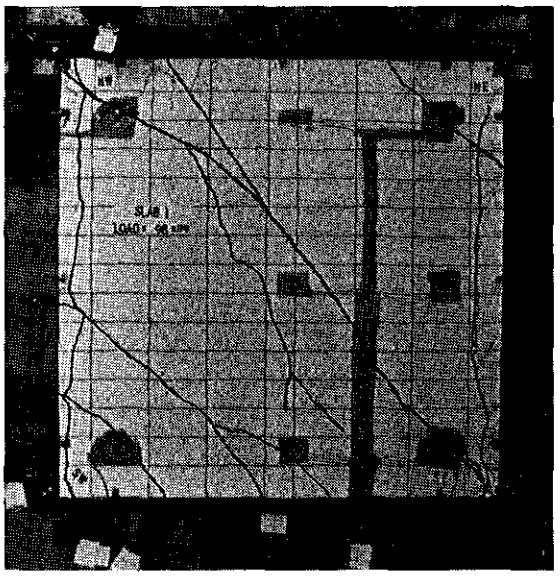

(c) MAXIMUM POSITIVE DISPLACEMENT (LP 40).

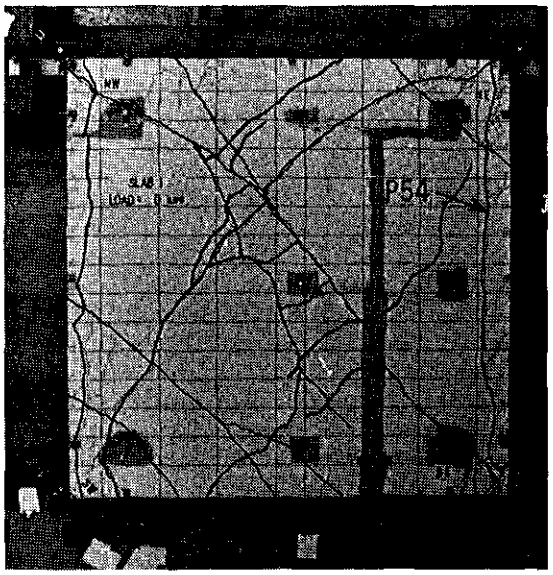

(d) END OF TEST (LP 65).

Fig. 19. Crack history for Specimen 1.

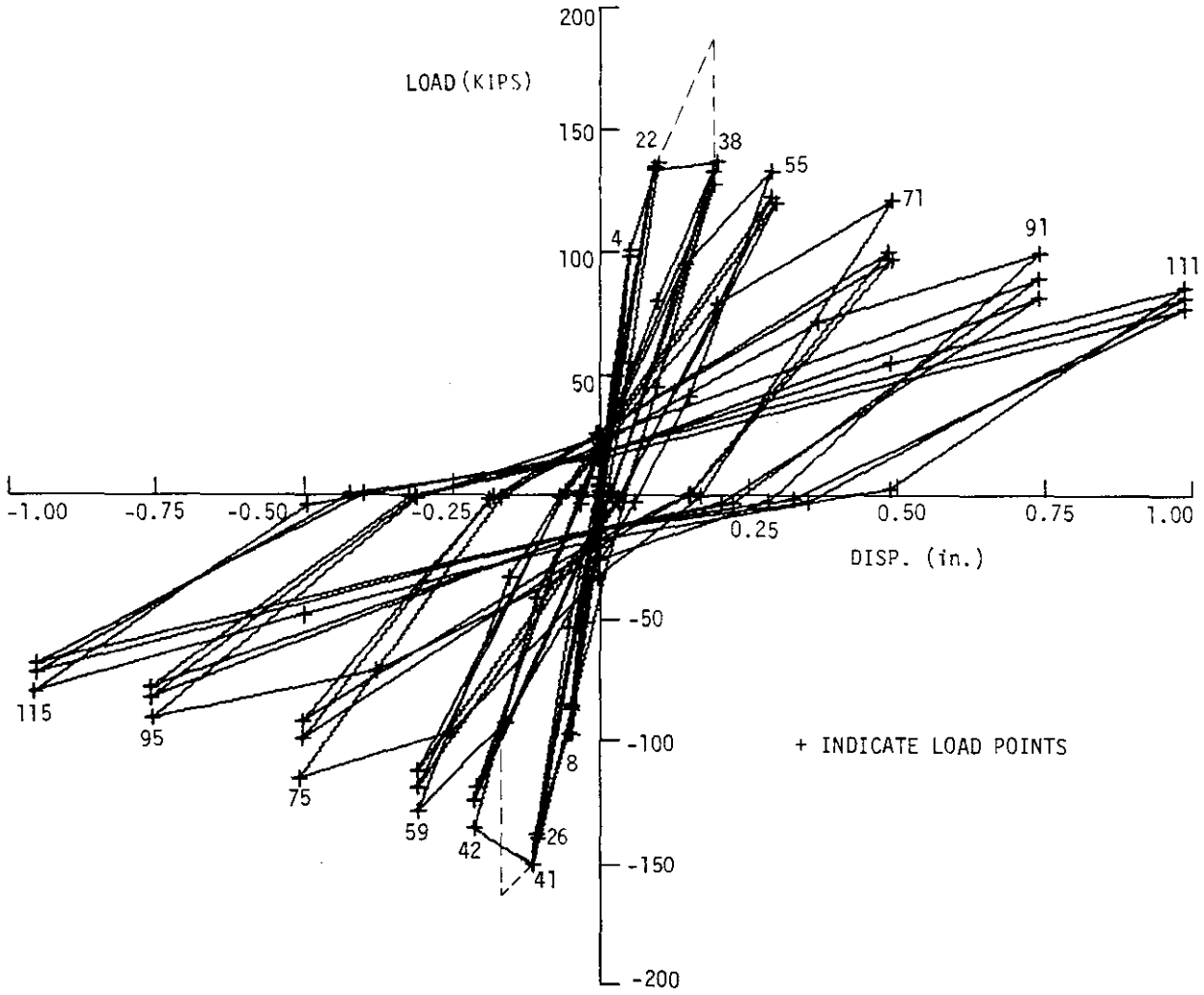

Fig. 20. Load-displacement diagram, Specimen 2.

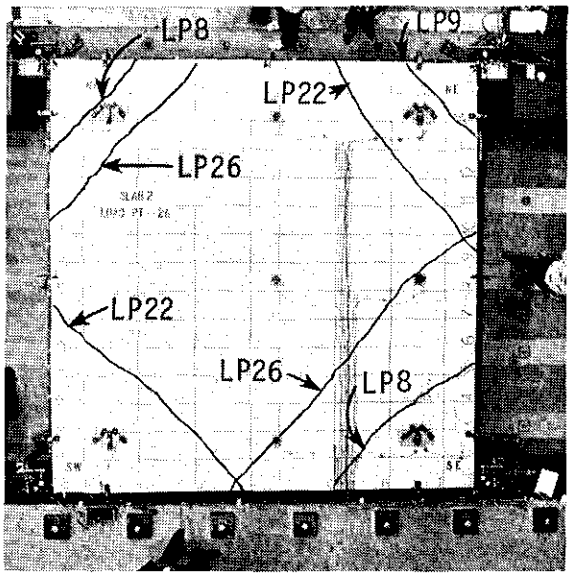

(a) LOAD EQUAL 138 KIPs (LP 26).

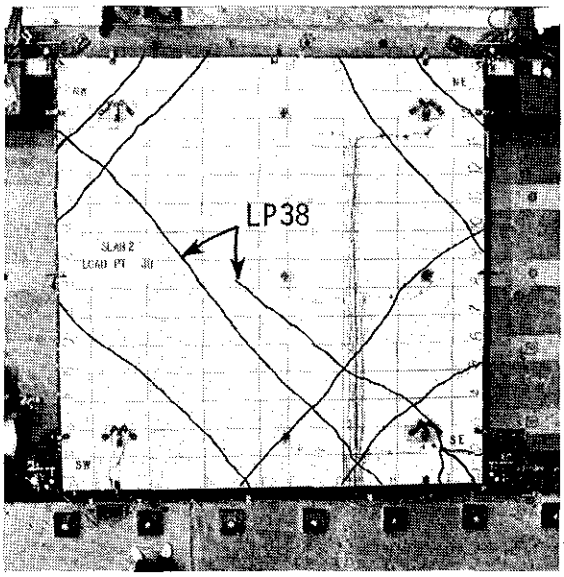

(b) LOAD EQUAL 136 KIPs (LP 38).

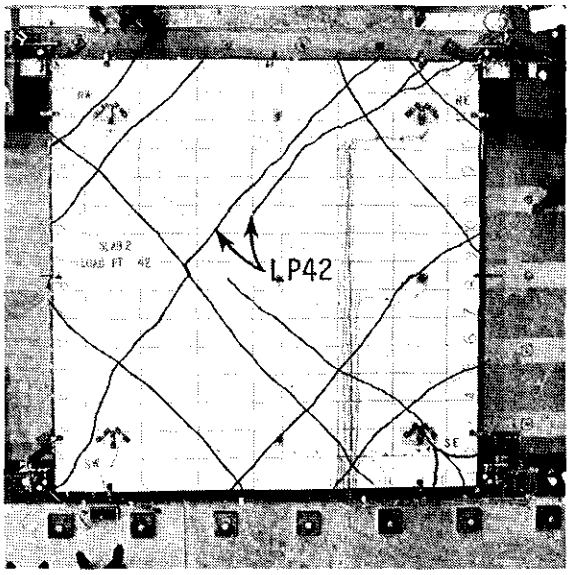

(c) LOAD EQUAL 136 KIPs (LP 42).

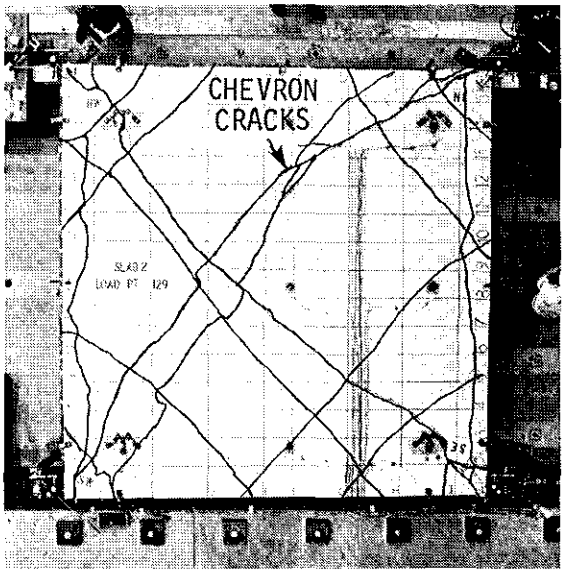

(d) END OF TEST (LP 129).

Fig. 21. Crack history for Specimen 2.

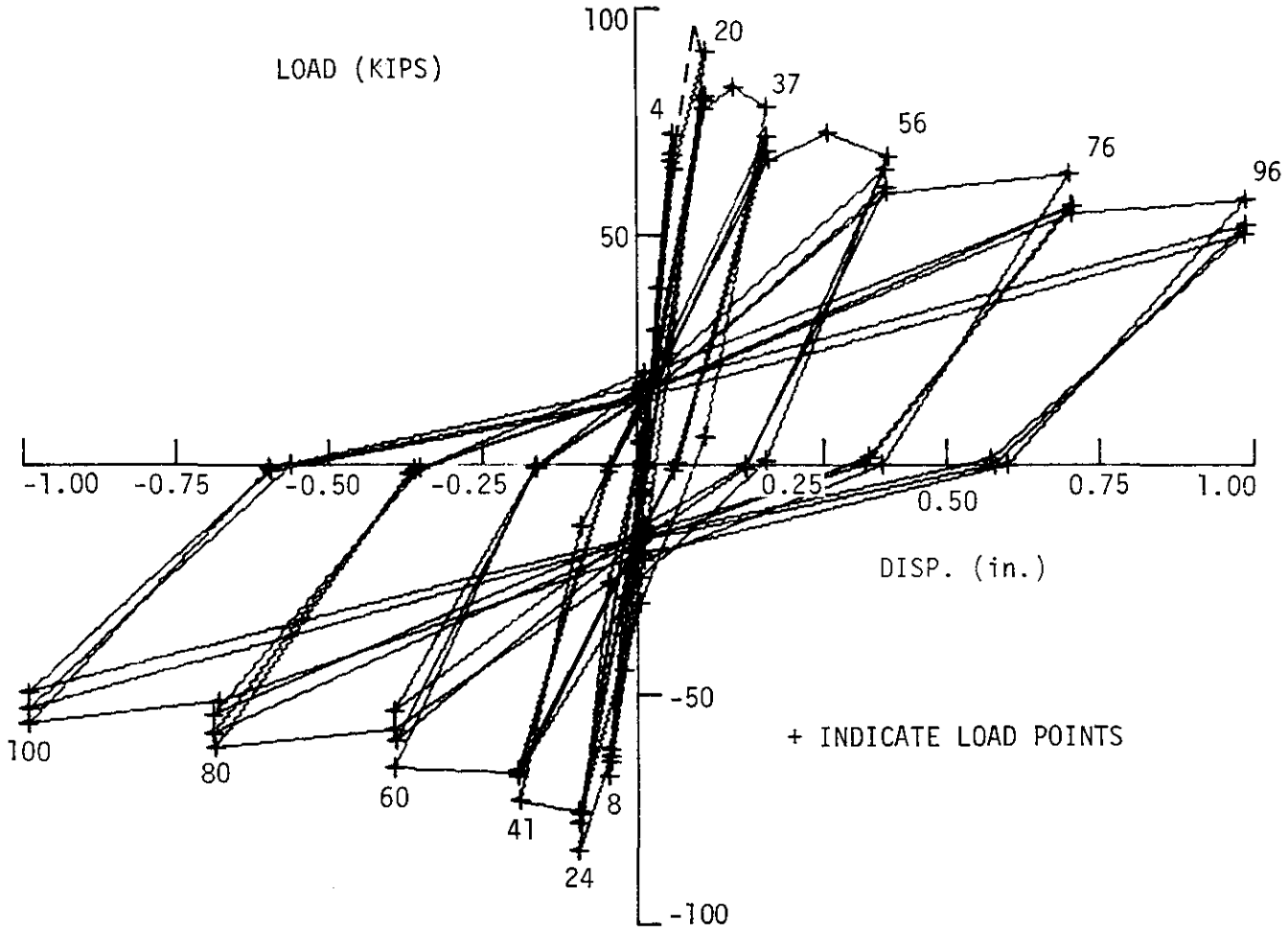

Fig. 22. Load-displacement diagram for Slab 3.

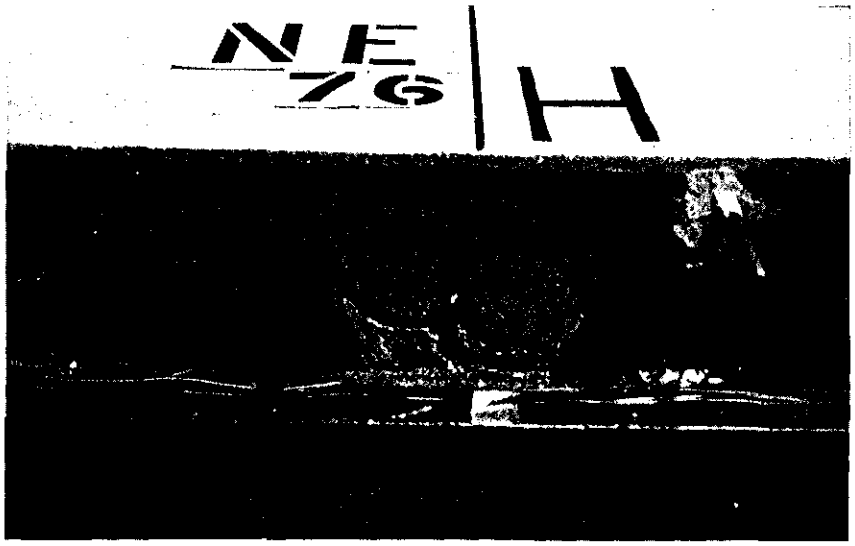

(a) PHOTO TAKEN AT A 0.7"-DISPLACEMENT.

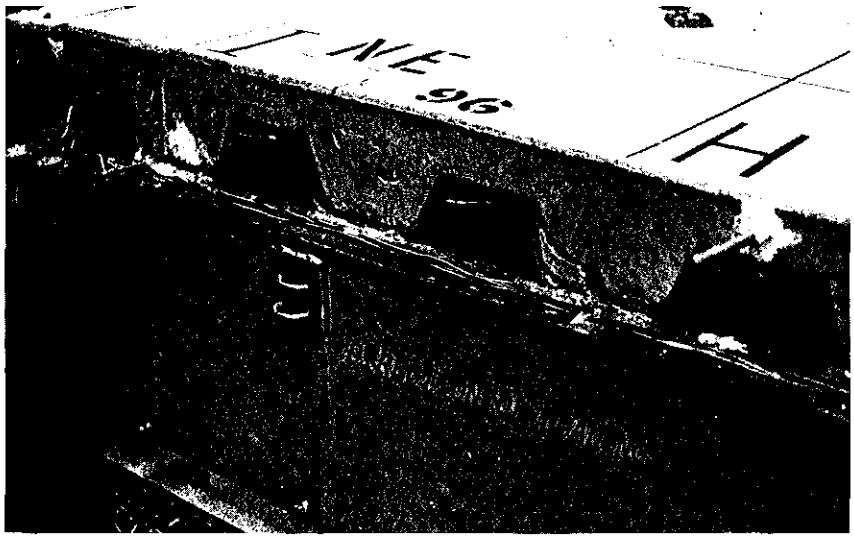

(b) PHOTO TAKEN AT A 1.0"-DISPLACEMENT.

Fig. 23. Steel deck fold-over.

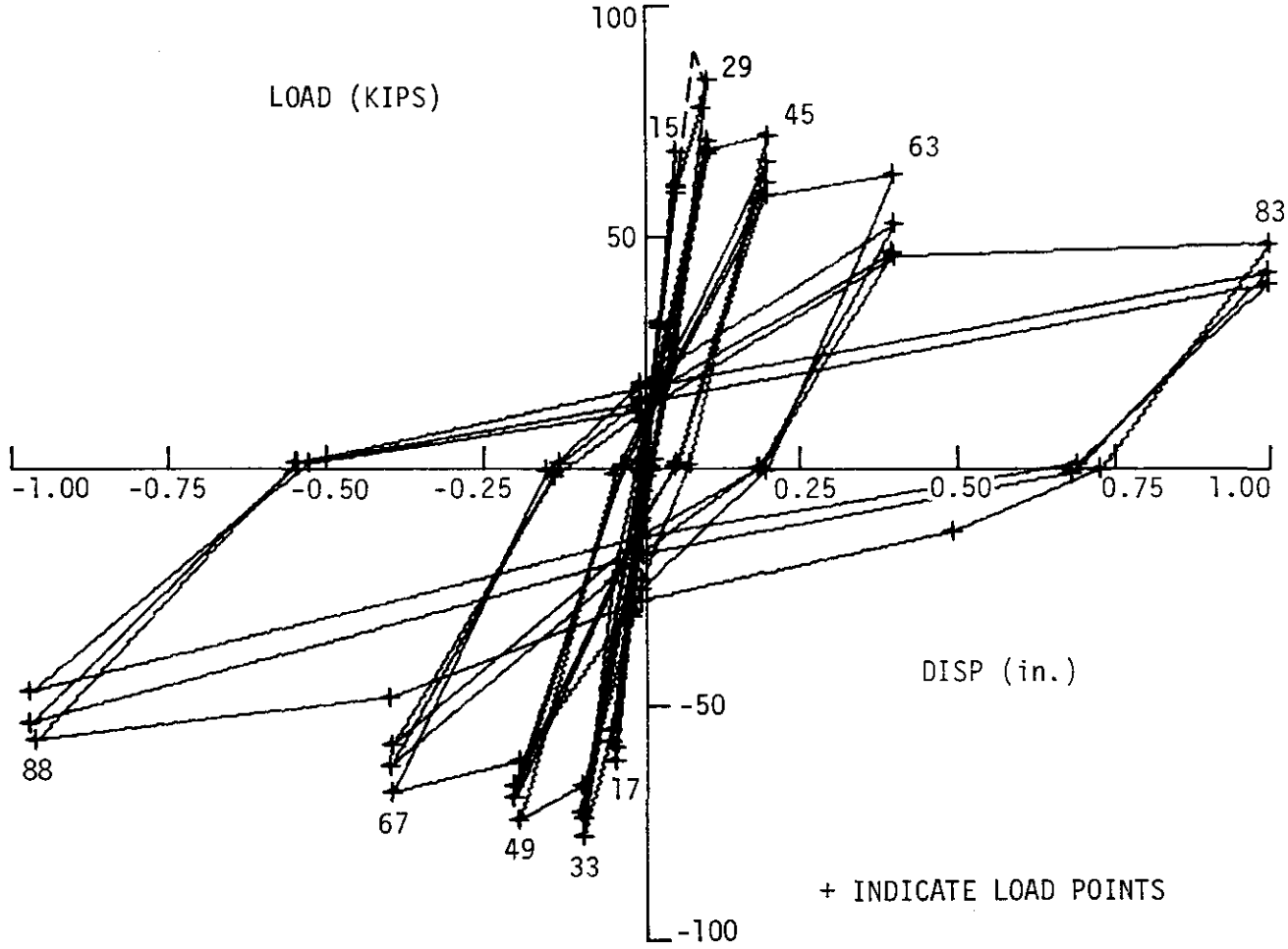

Fig. 24. Load-displacement diagram for Slab 4.

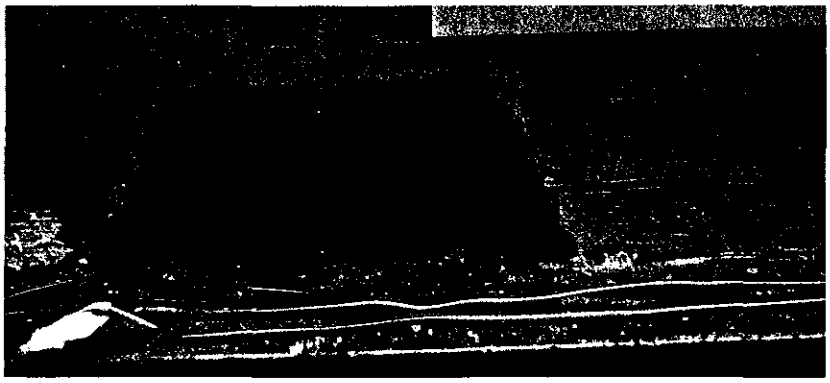

Fig. 25. Diagonal seam crack.

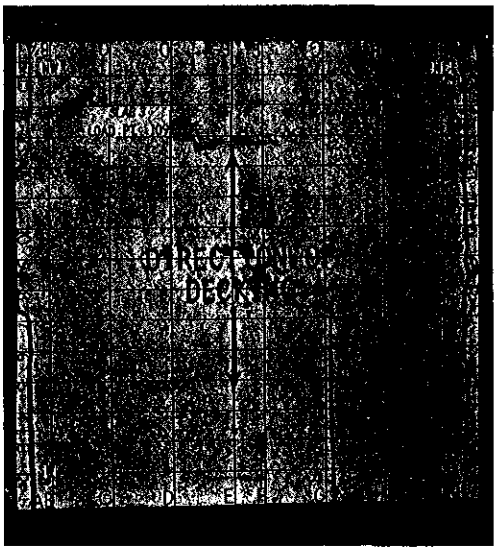

(a) SLAB 3.

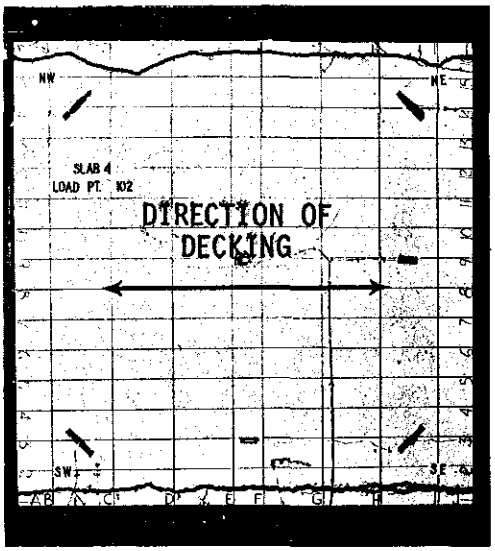

(b) SLAB 4.

Fig. 26. Top surface cracking for Slabs 3 and 4.

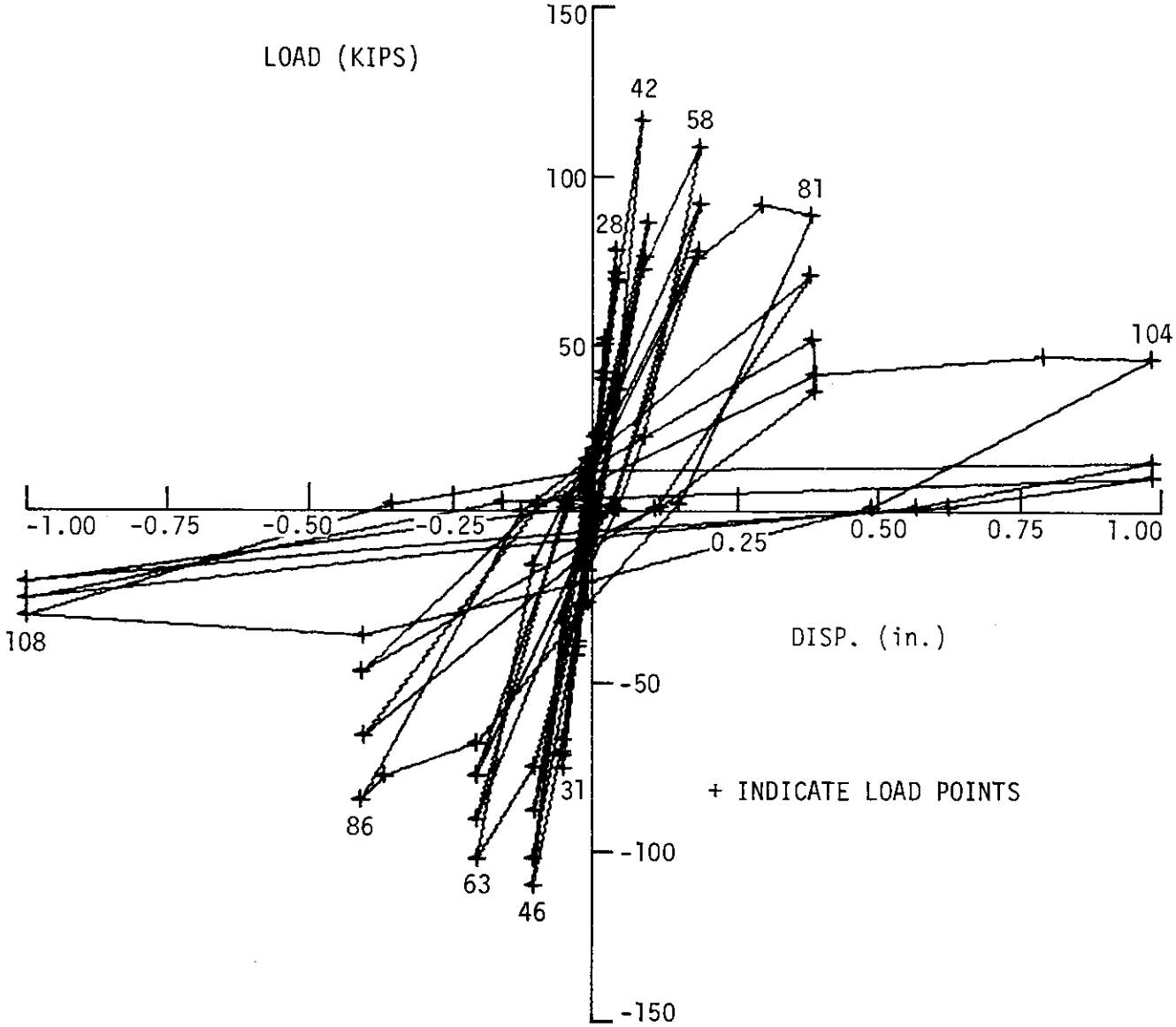

Fig. 27. Load-displacement diagram for Slab 5.

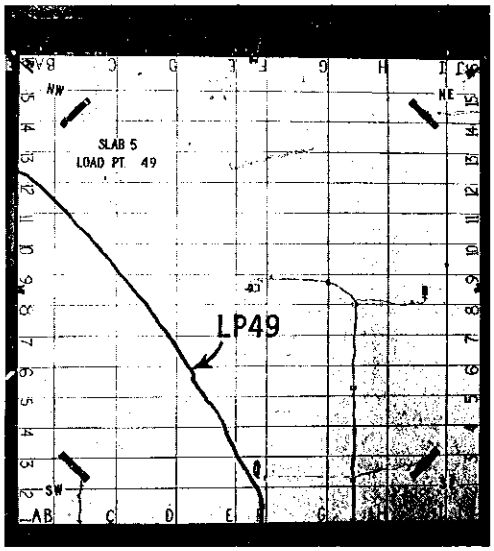

(a) FIRST MAJOR CRACK.

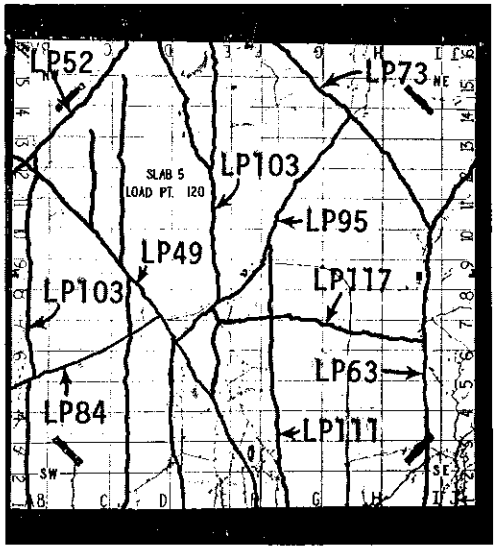

(b) FINAL CRACK PATTERN.

Fig. 28. Top surface cracking for Slab 5.

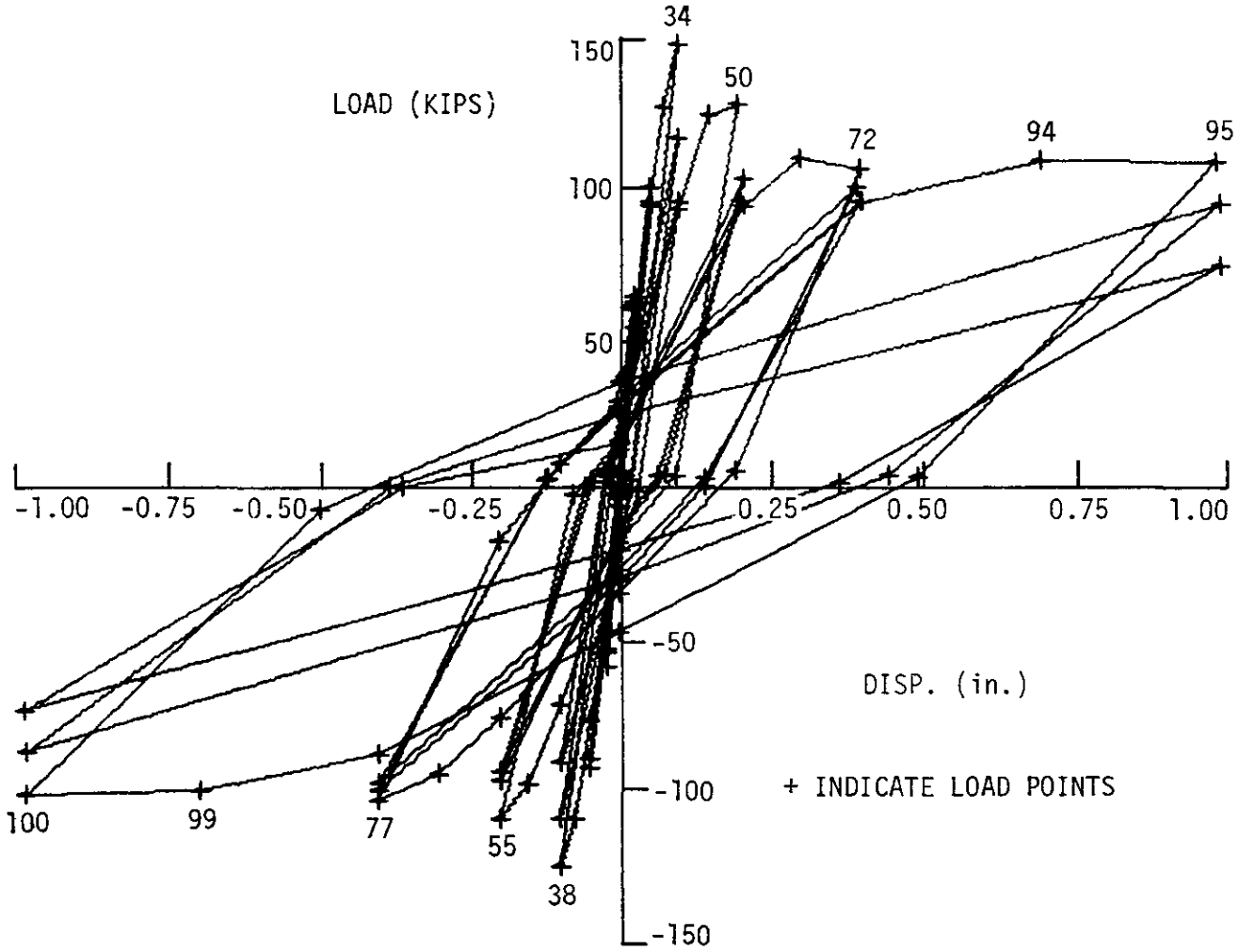

Fig. 29. Load-displacement diagram for Slab 6.

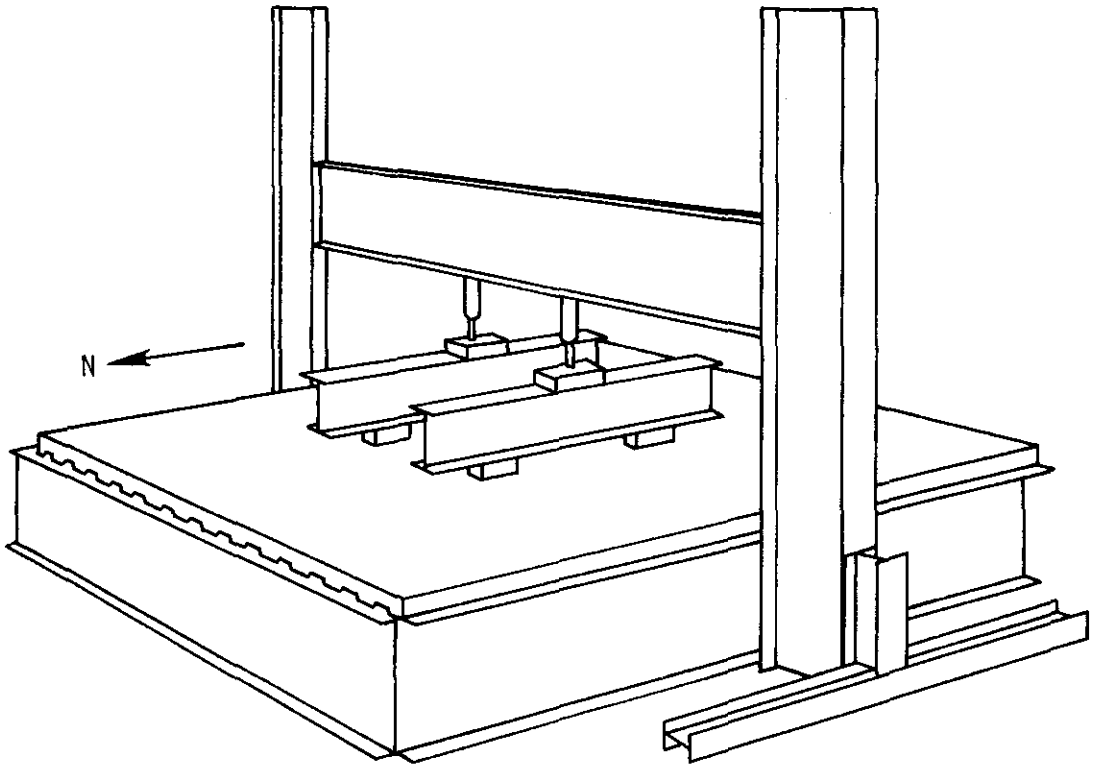

Fig. 30. Vertical load test setup.

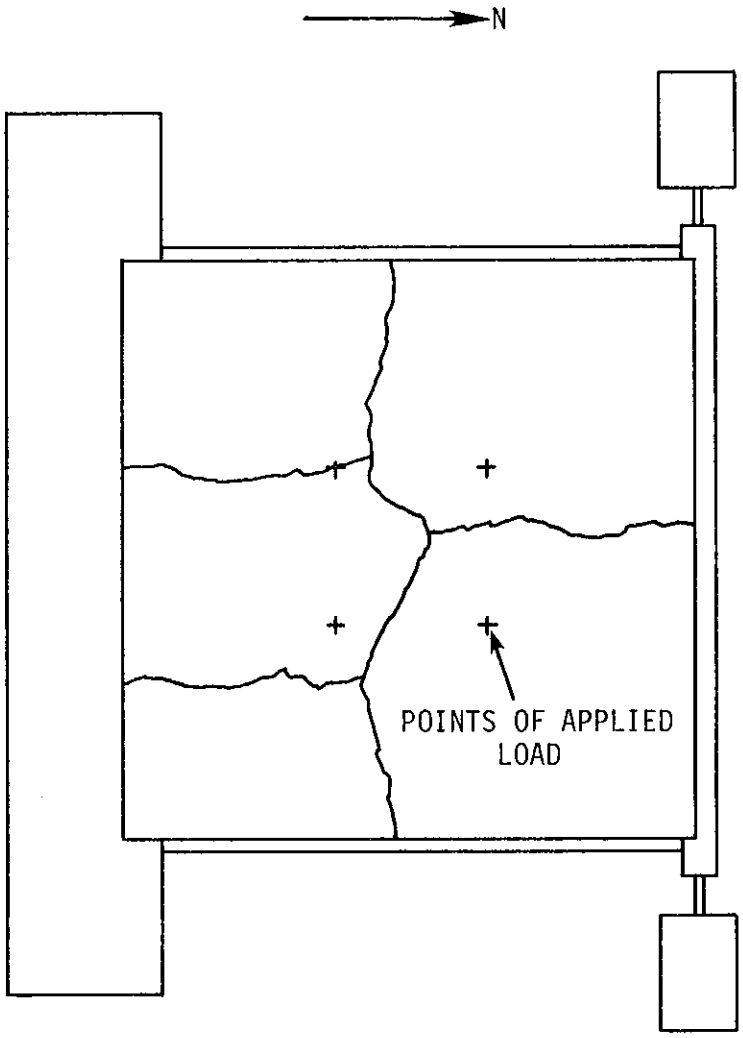

Fig. 31. Slab 6 final crack pattern after application of vertical load.

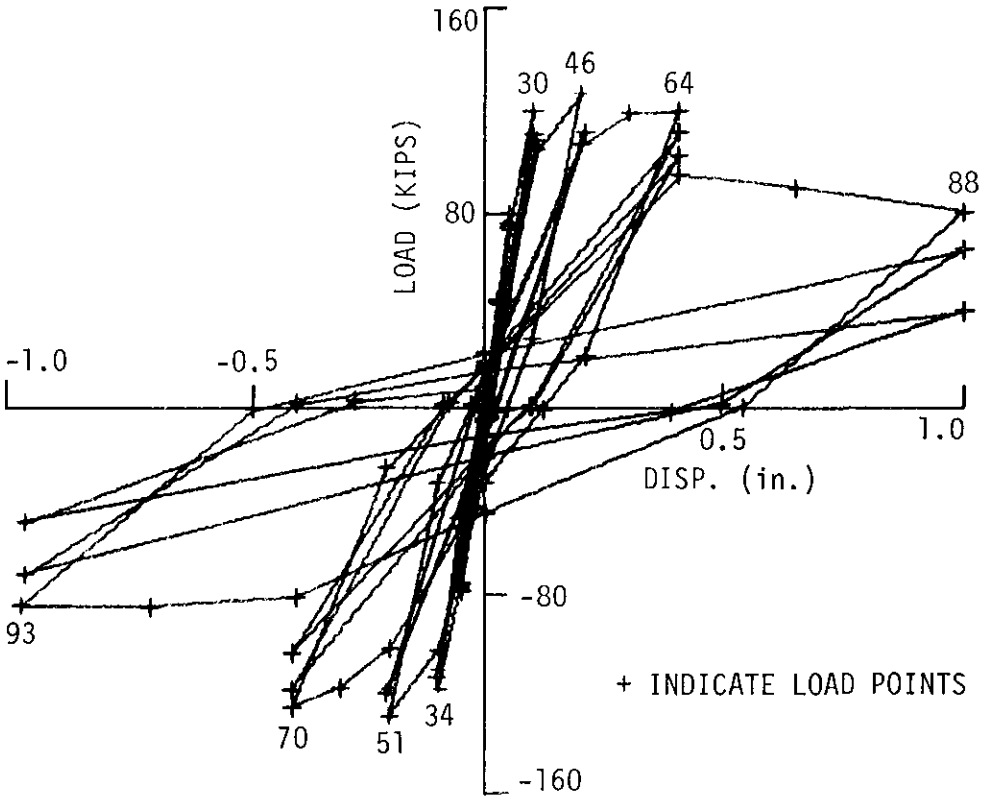

Fig. 32. Load-displacement diagram for Slab 7.

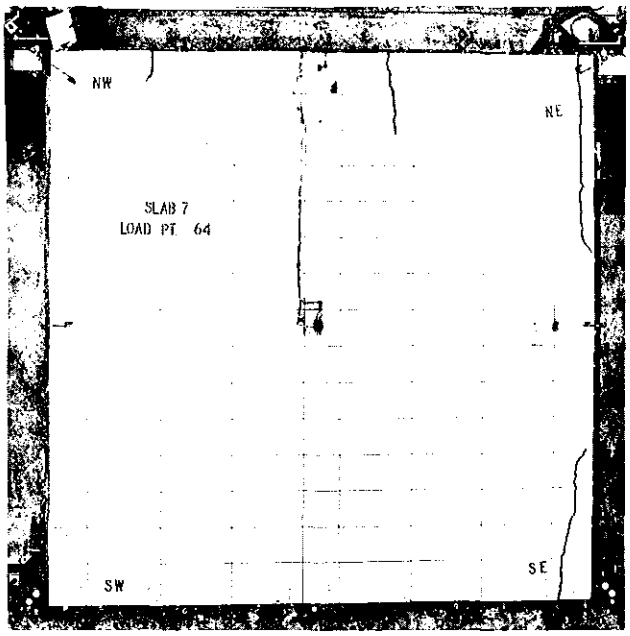

(a) CONCRETE FAILURE AT NE CORNER (LP 64).

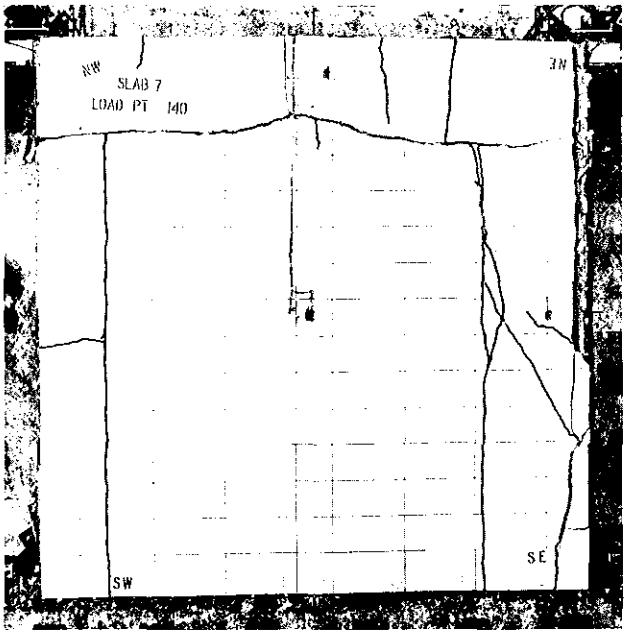

(b) FINAL CRACK PATTERN

Fig. 33. Top surface cracking for Slab 7.

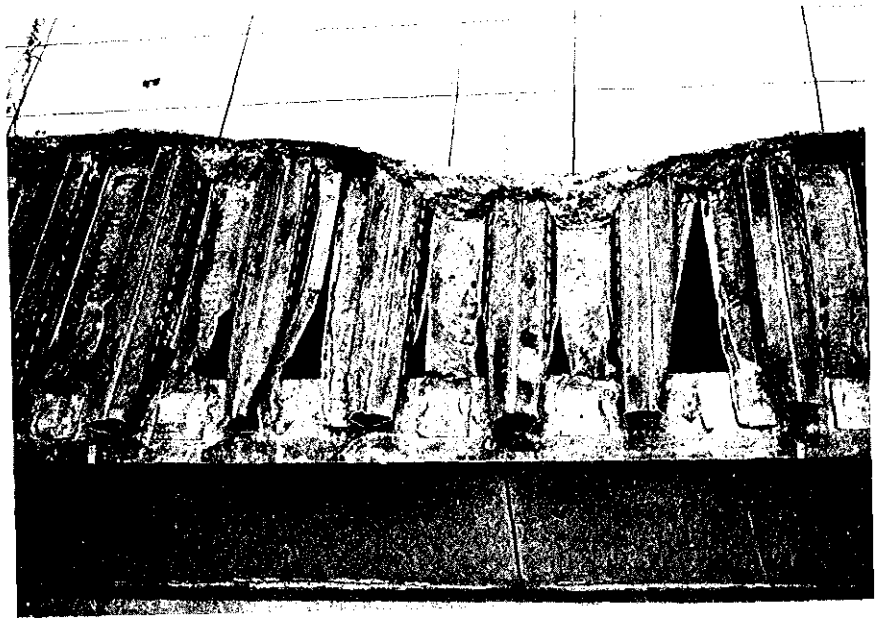

Fig. 34. Tearing of deck along north support beam.

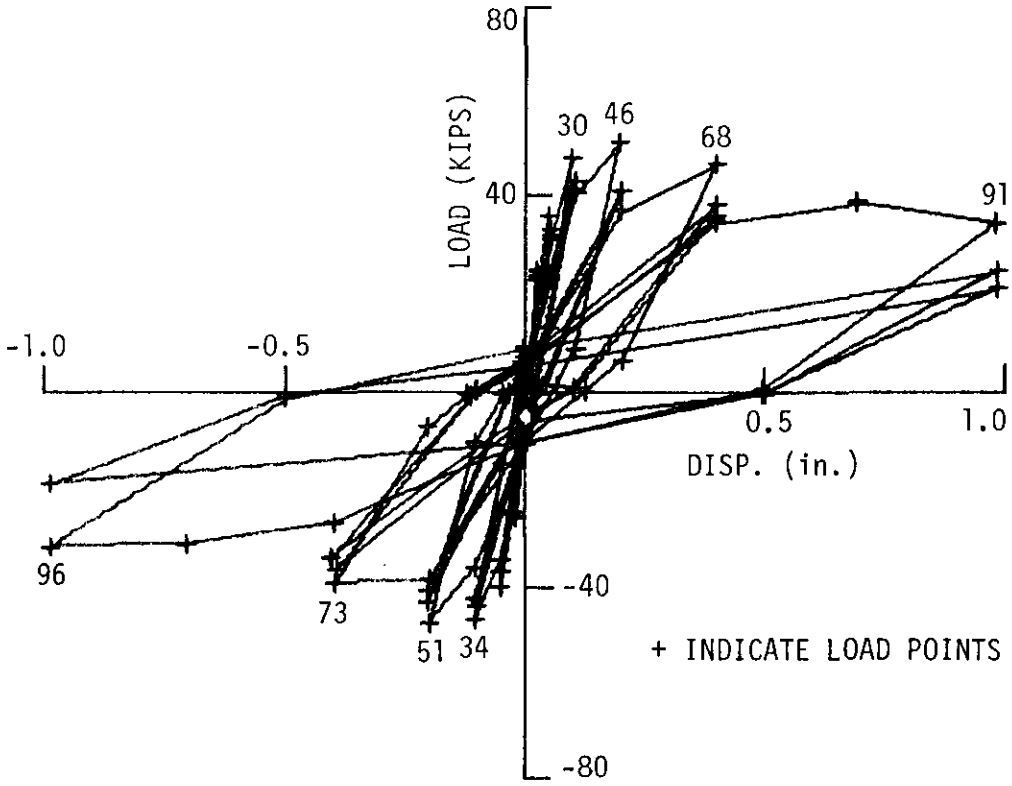

Fig. 35. Load-displacement diagram for Slab 8.

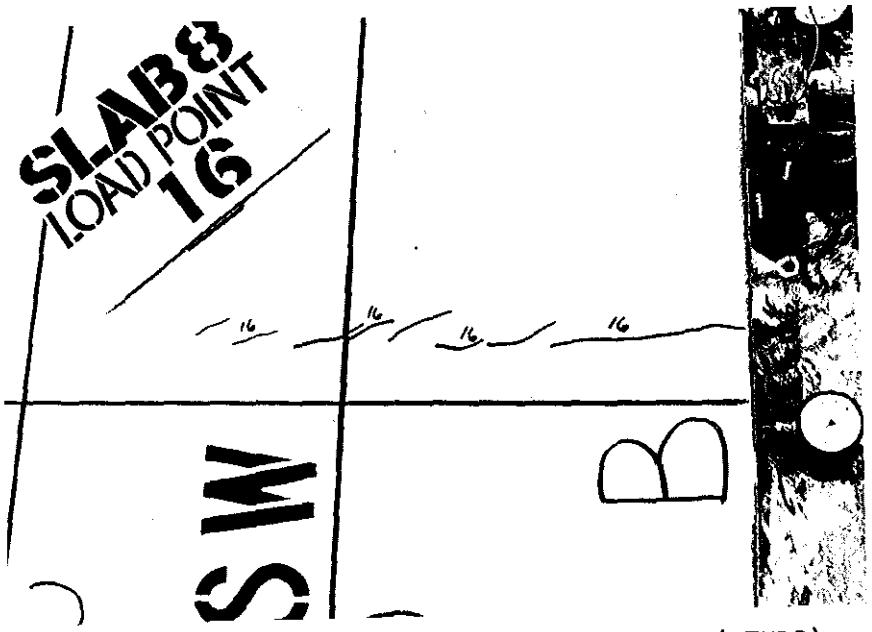

(a) INITIAL CRACKING AROUND EDGE CONNECTORS (STUDS).

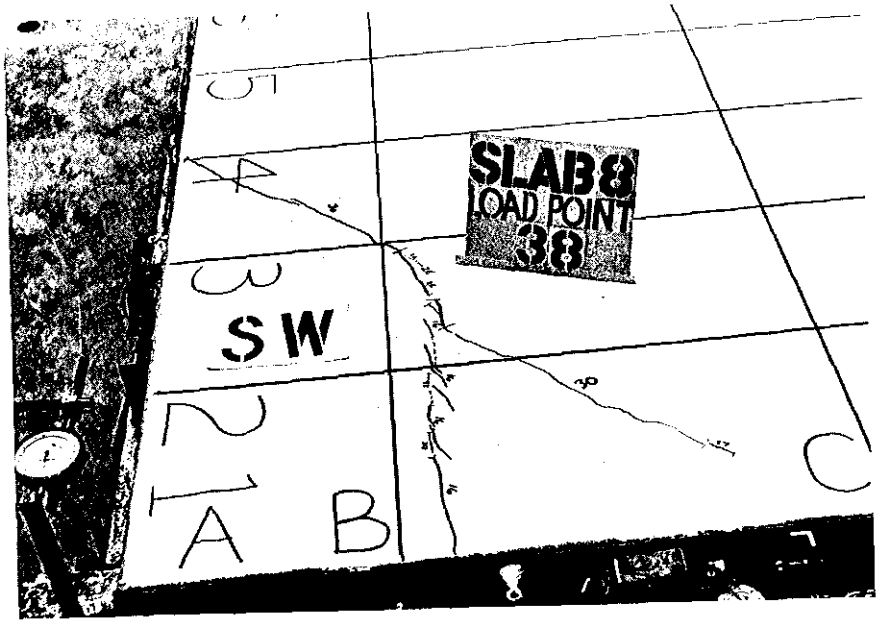

(b) DIAGONAL CRACKING TYPICAL AT CORNERS.

Fig. 36. Early crack patterns for Slab 8.

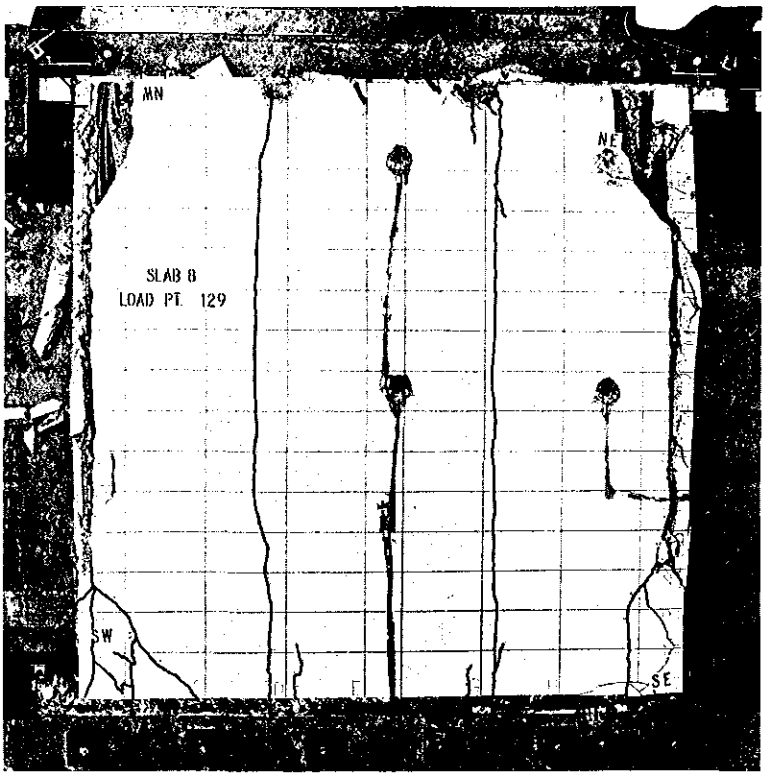

Fig. 37. Final crack pattern for Slab 8.

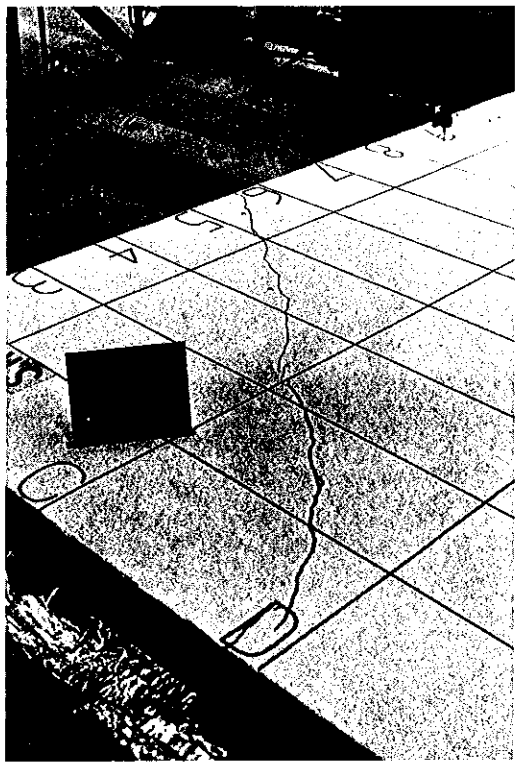

(a) DIAGONAL CRACK AT SW CORNER (LP 16).

(b) DIAGONAL CRACK AT NE CORNER (LP 46).

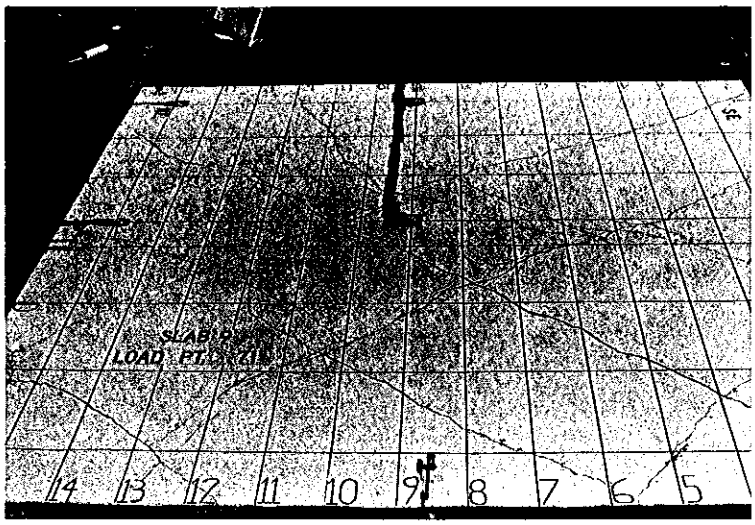

(c) CONTINUING PATTERN OF DIAGONAL CRACKING.

Fig. 38. Concrete cracking for Slab 9.

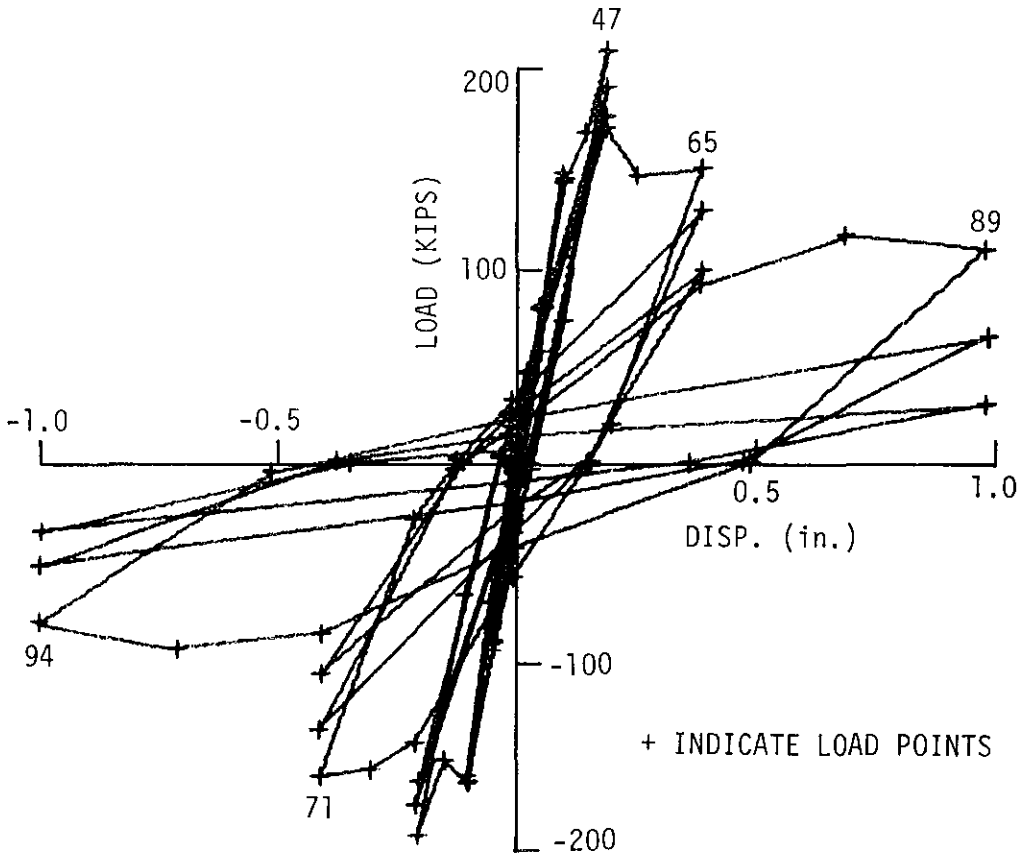

Fig. 39. Load-displacement diagram for Slab 9.

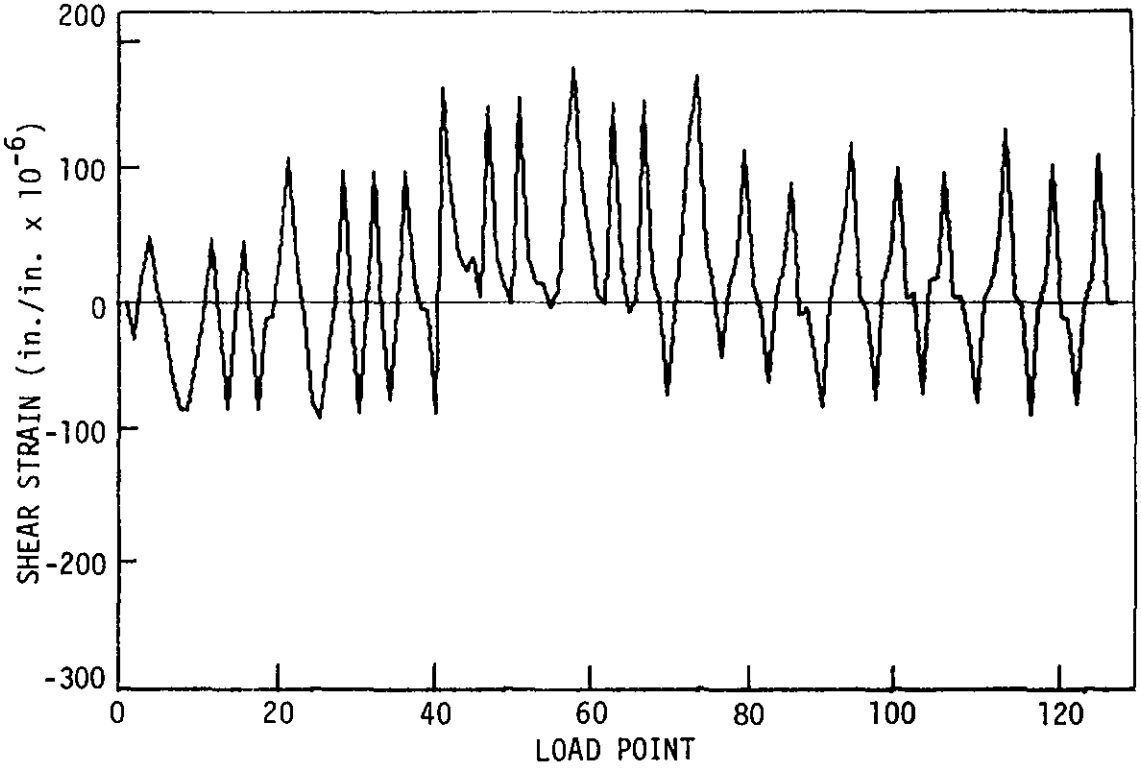

Fig. 40. Typical slab surface strains.

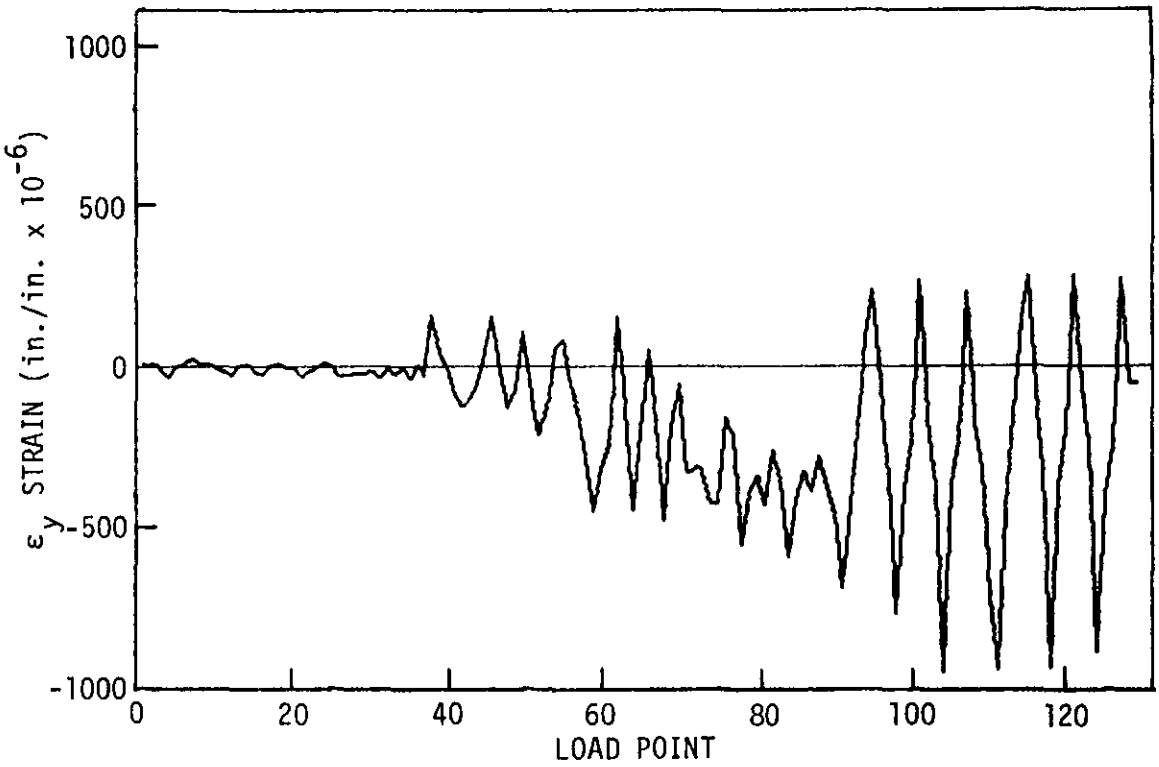

Fig. 41. Typical deck strains.

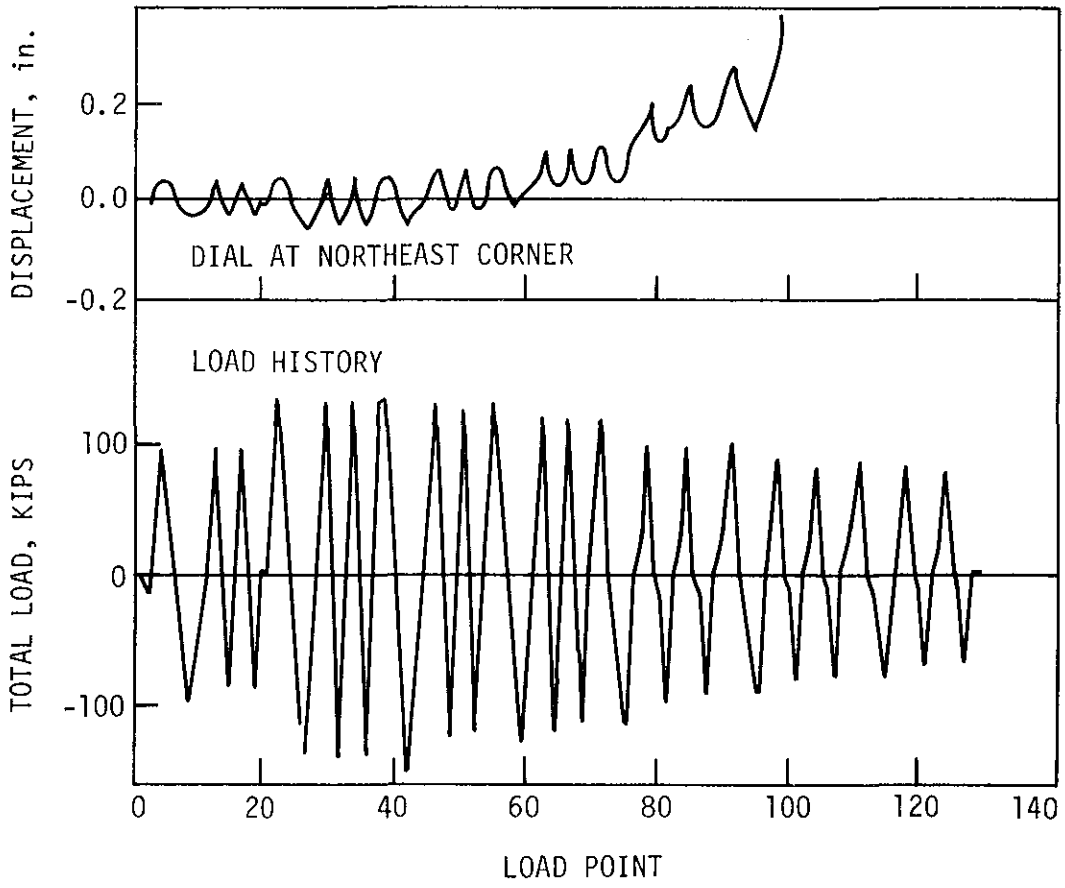

Fig. 42. Typical cyclic pattern of vertical displacement along main load beam.

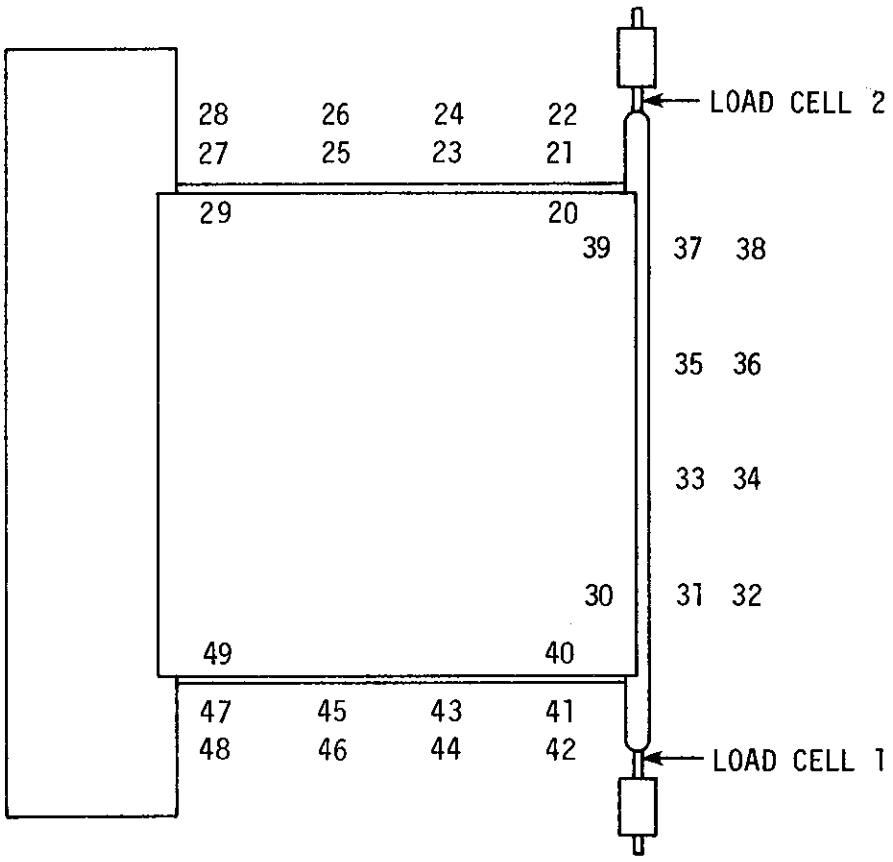

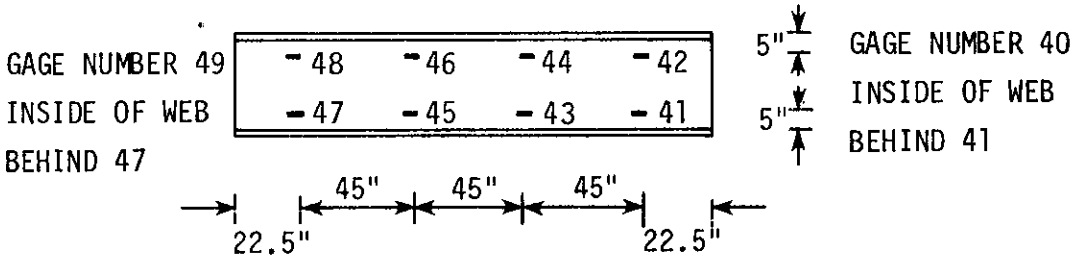

ELEVATION VIEW OF W24 x 76 FRAME BEAM
(TYPICAL)

Fig. 43. Edge-beam strain gage locations.

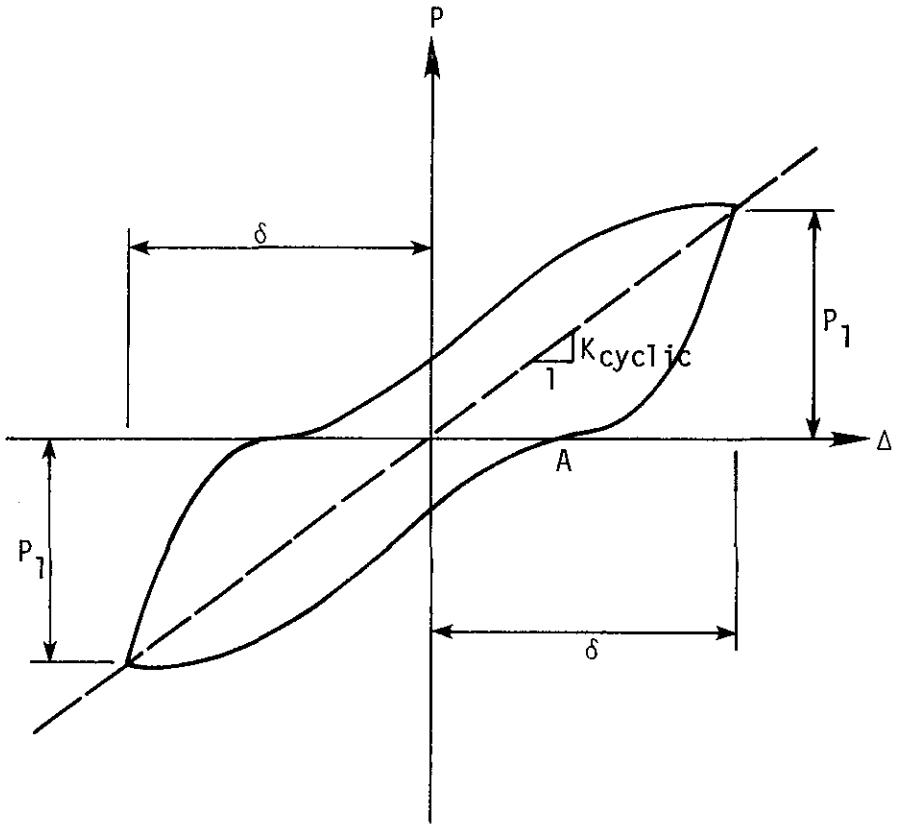

Fig. 44. Calculation of average cyclic stiffness, K_{cyclic}, from force-deflection hysteresis loop.

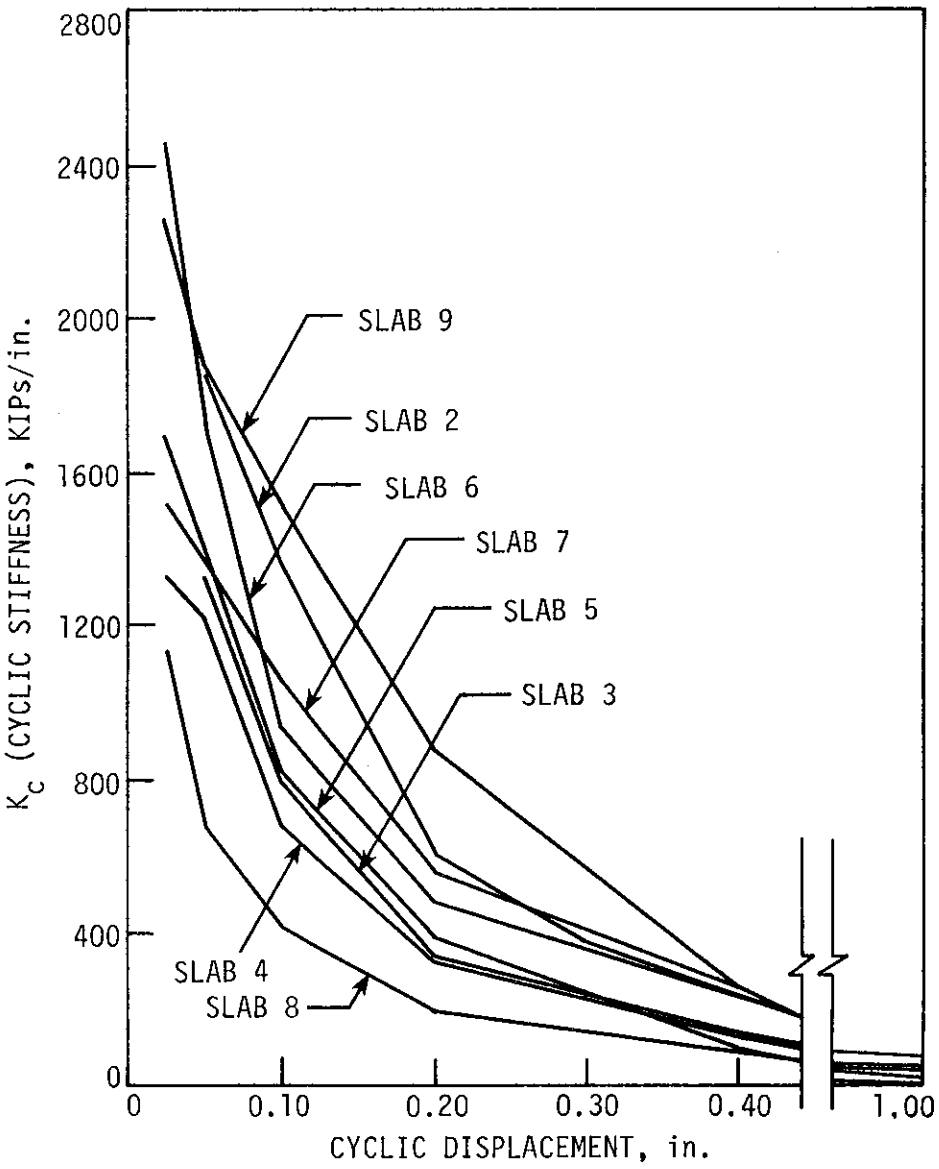

Fig. 45. Stiffness degradation following three cycles of reversed loading at each displacement increment.

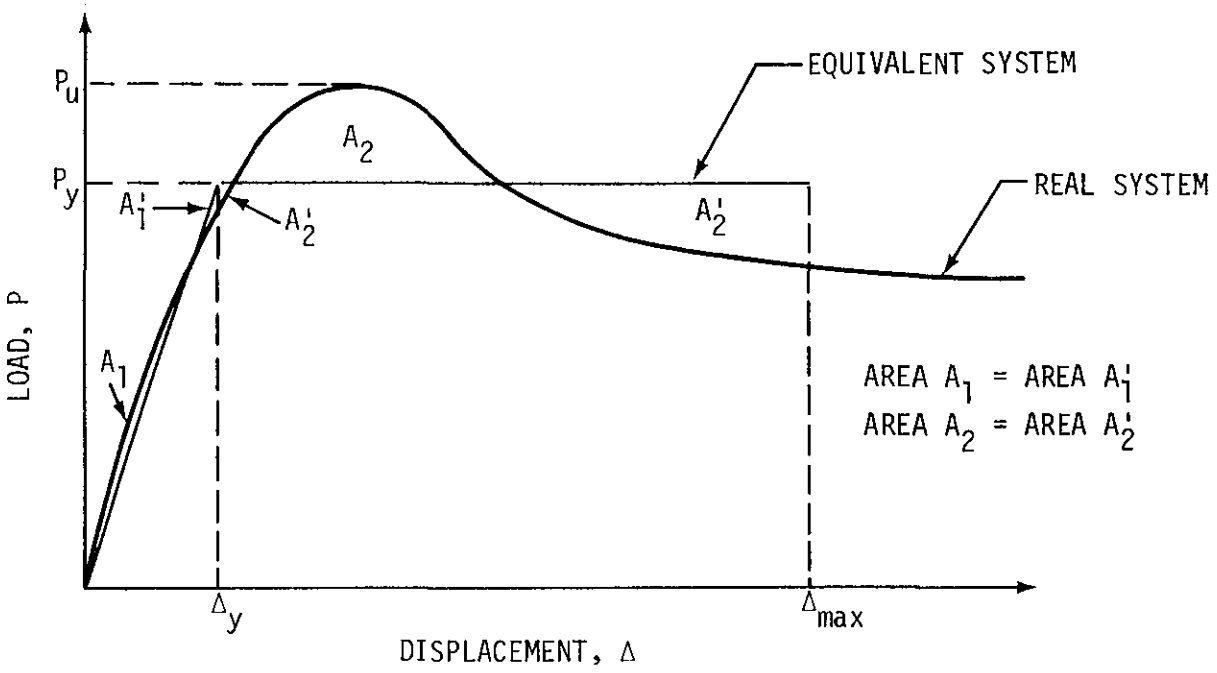

Fig. 46. Equivalent elastic-perfectly-plastic system.

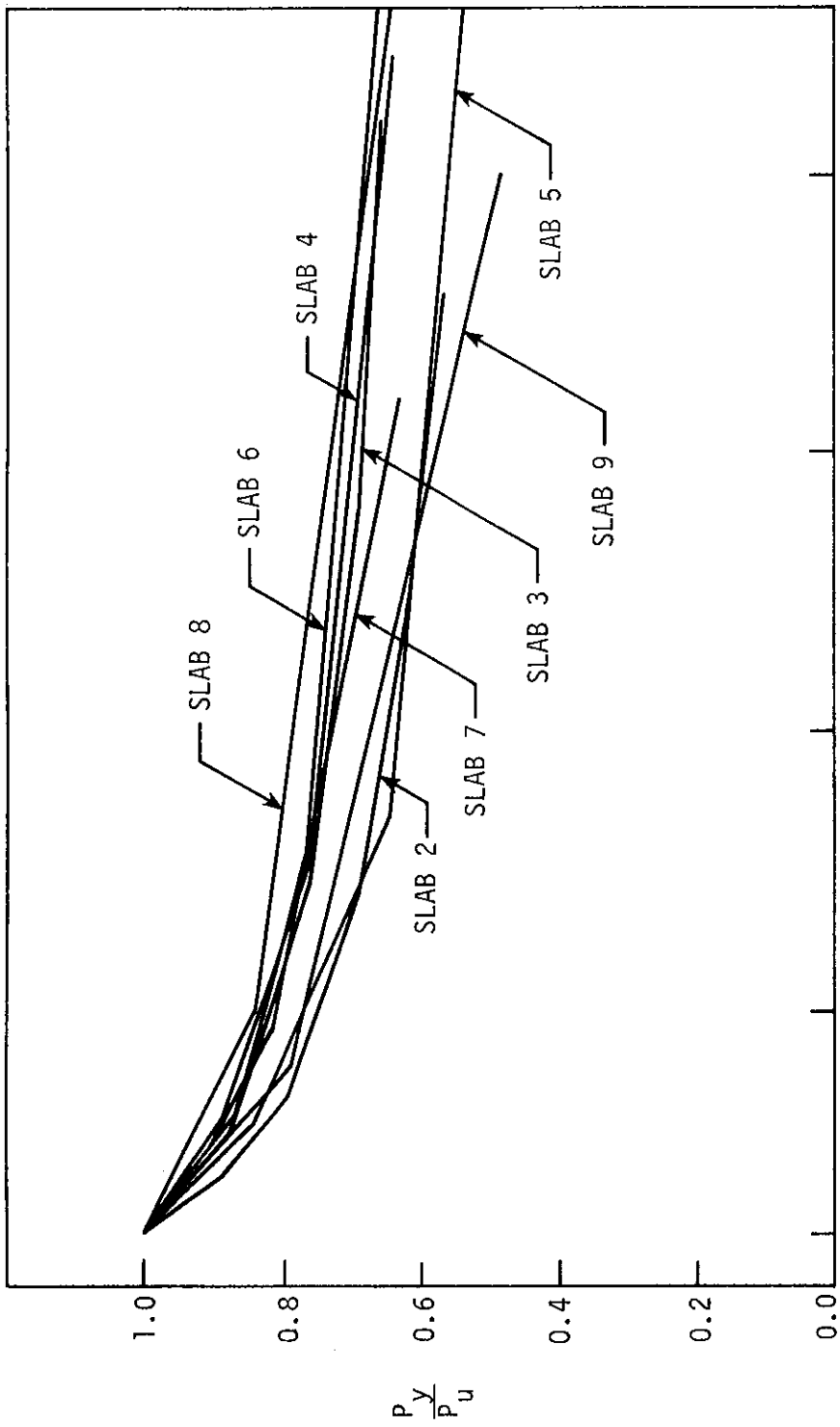

Fig. 47. Ductility capacity.

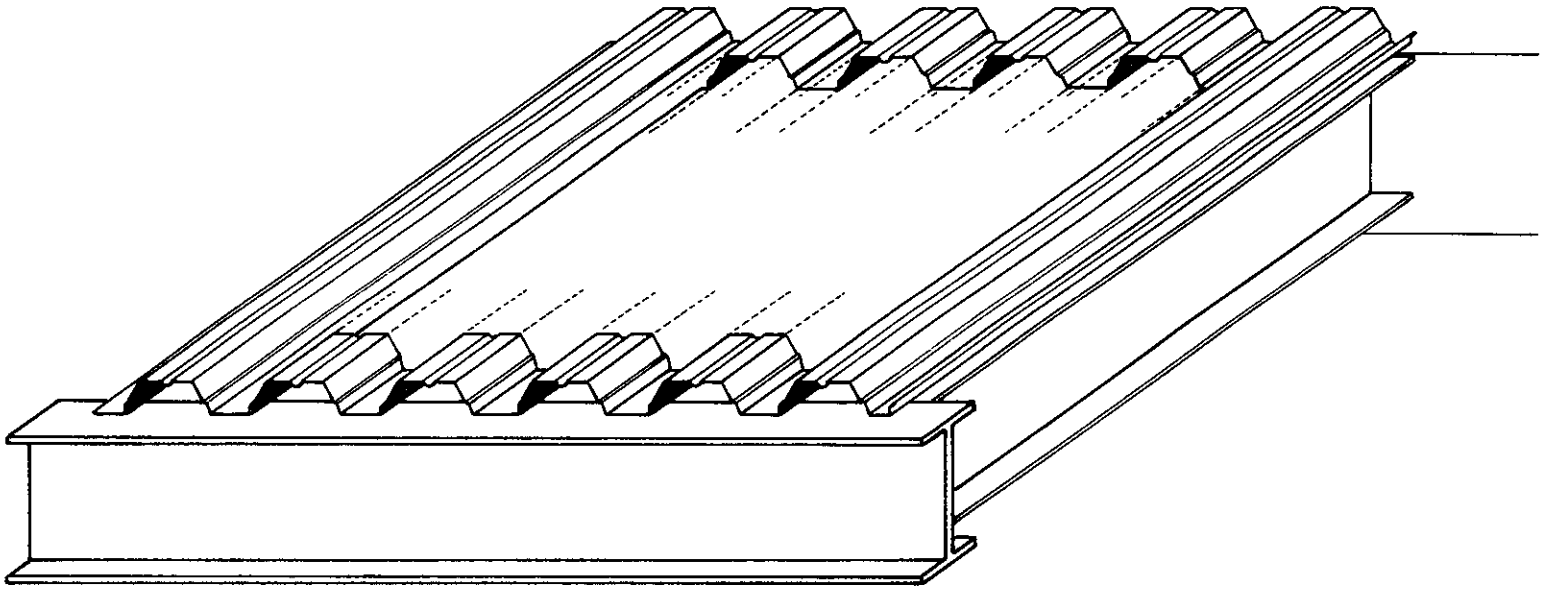

Fig. 48. Edge zone of deck effective in transferring forces from frame to concrete slab.

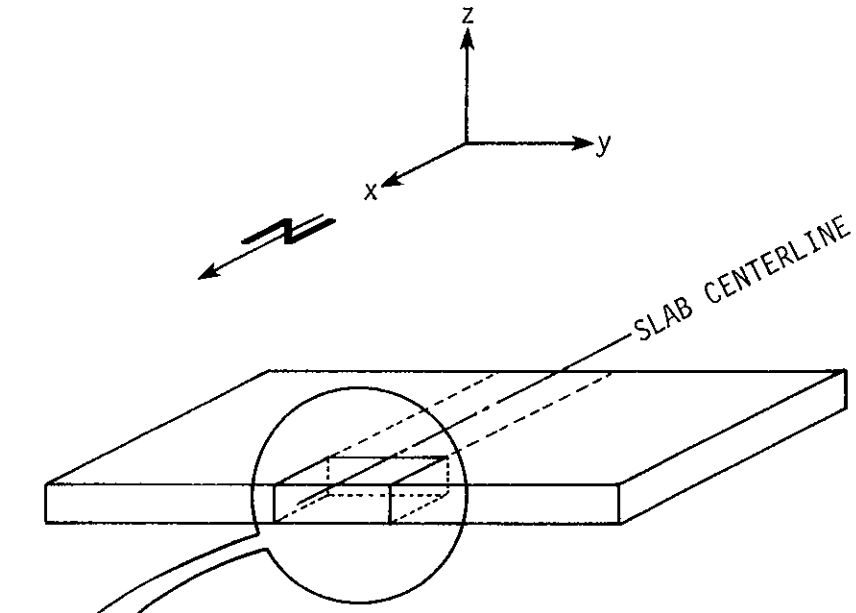

Fig. 49. Istotropic slab for finite-element analysis.

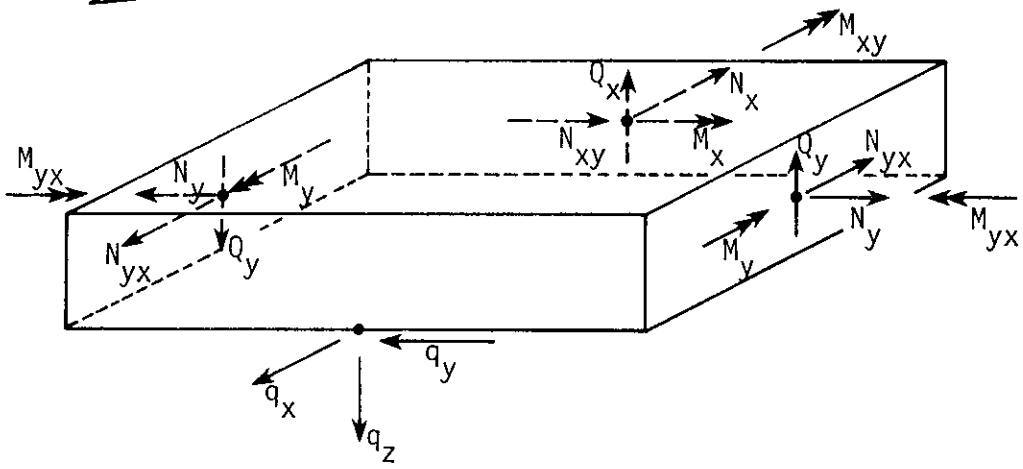

Fig. 50. Potential stress resultants on segment of edge zone on slab centerline.

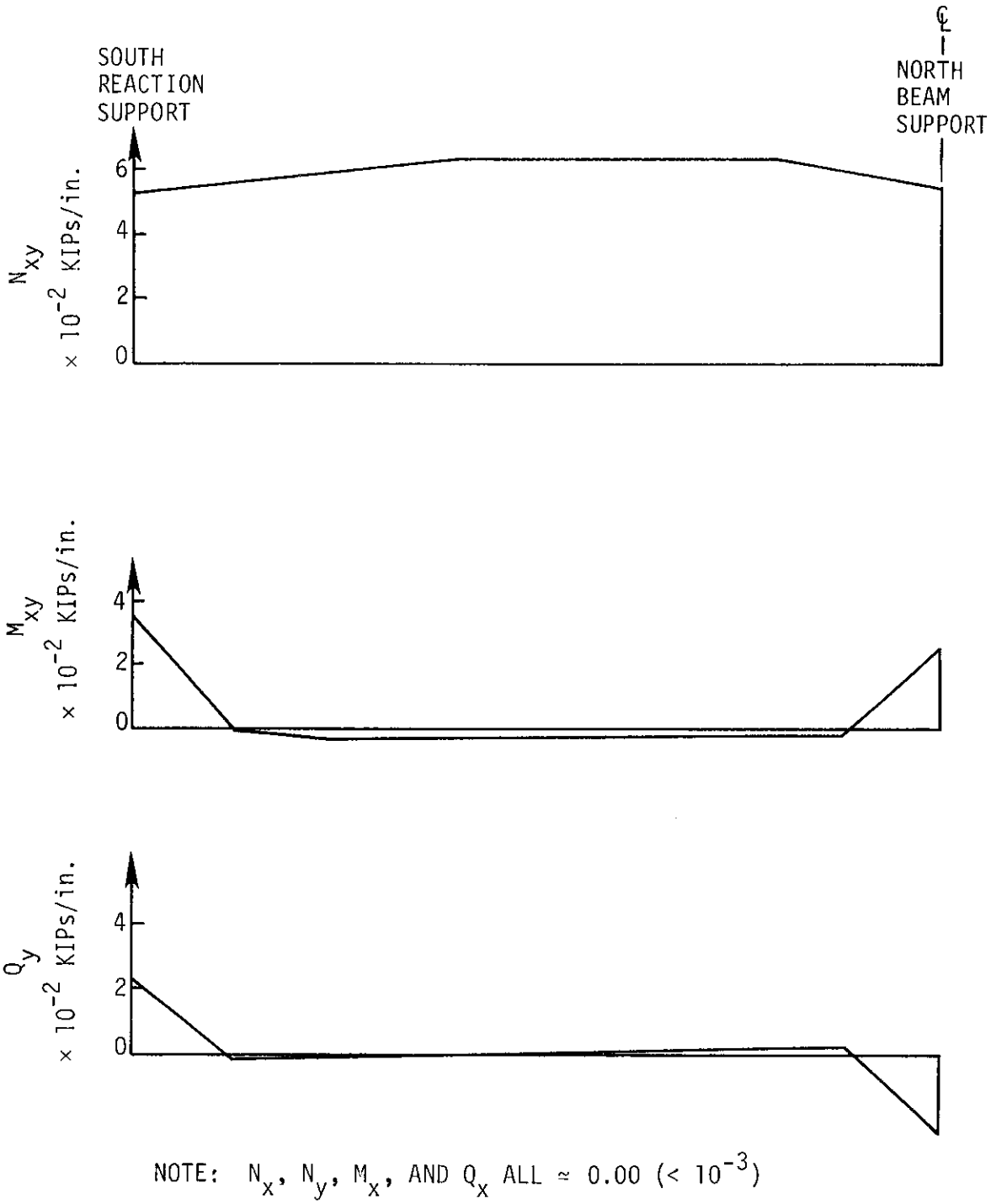

Fig. 51. Variation of stress resultants on element along N-S centerline based on finite-element analysis.

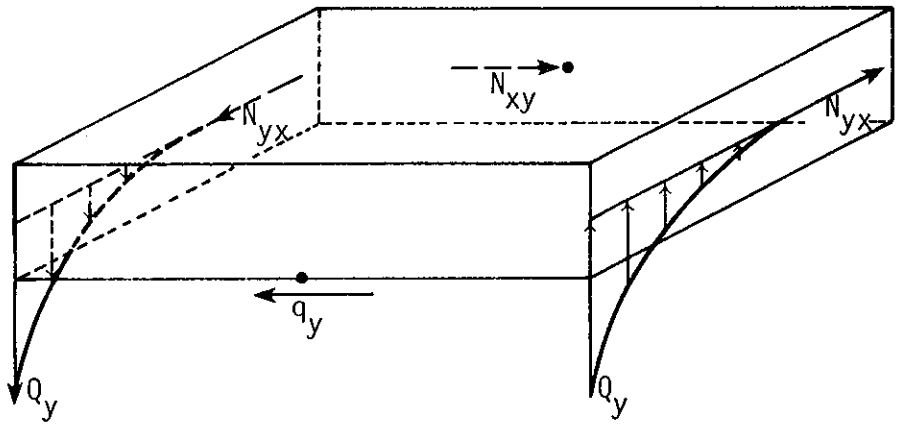

Fig. 52. Nonzero forces on segment of edge zone on slab centerline.

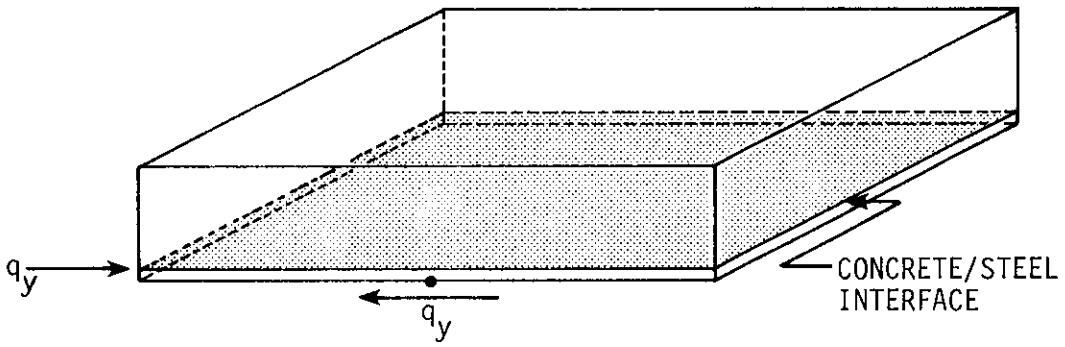

Fig. 53. Equivalent force system within edge zone.

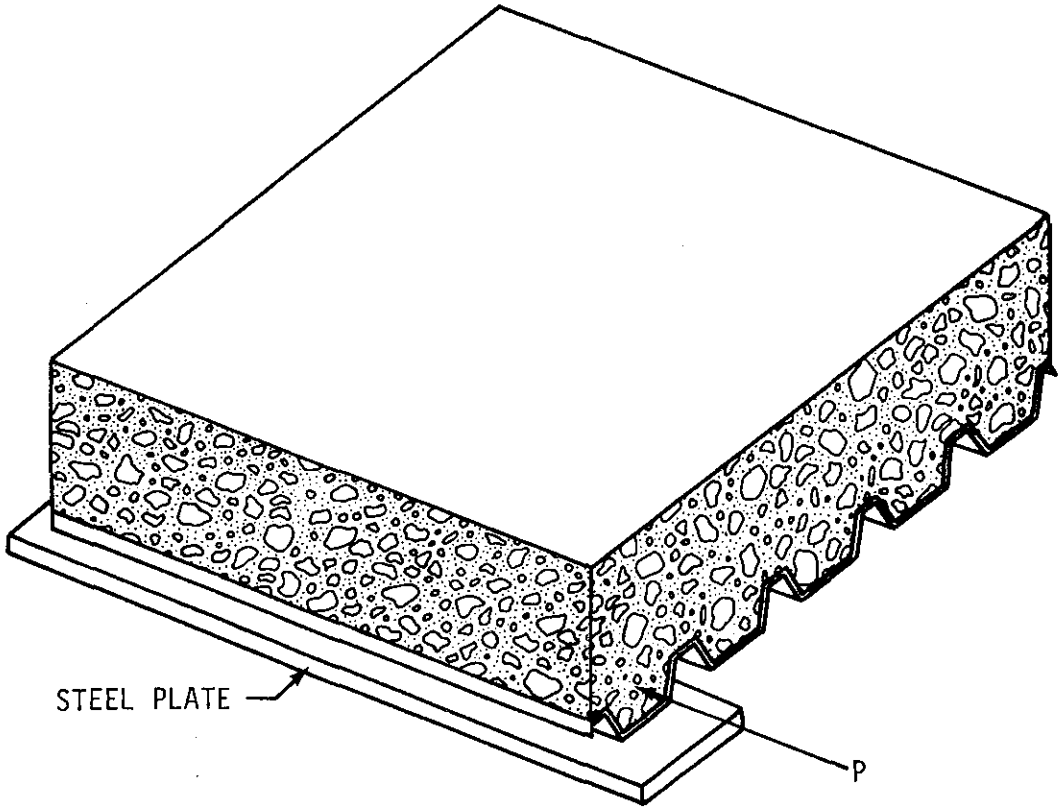

Fig. 54. Schematic of longitudinal pushout specimen (Deck Type 2).

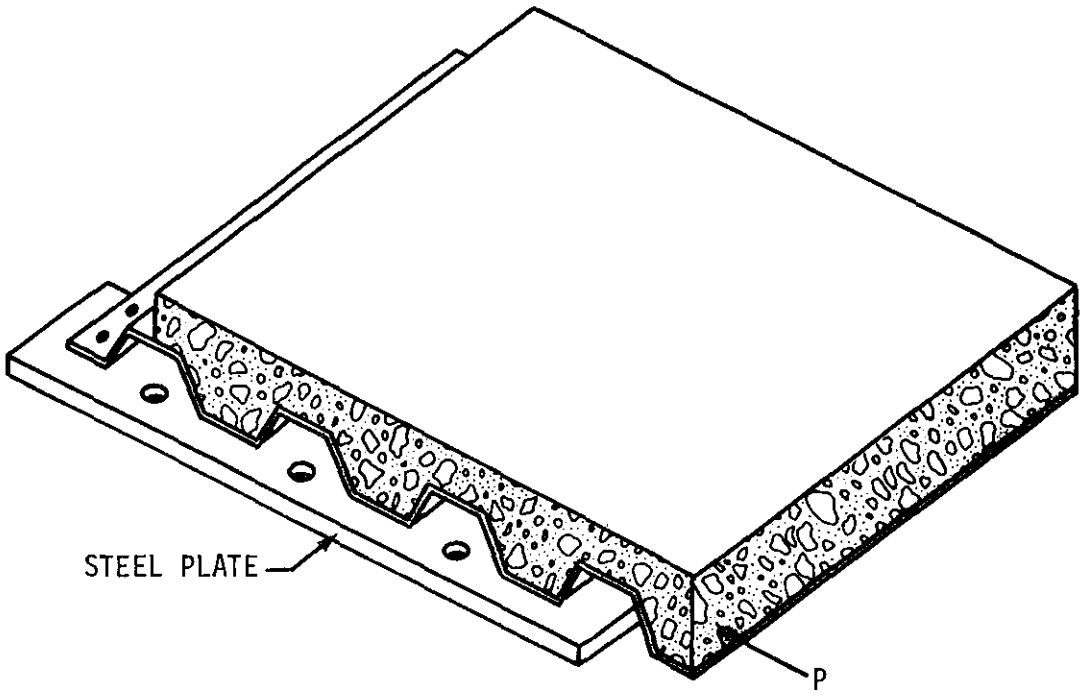

Fig. 55. Schematic of transverse pushout specimen (Deck Type 1).

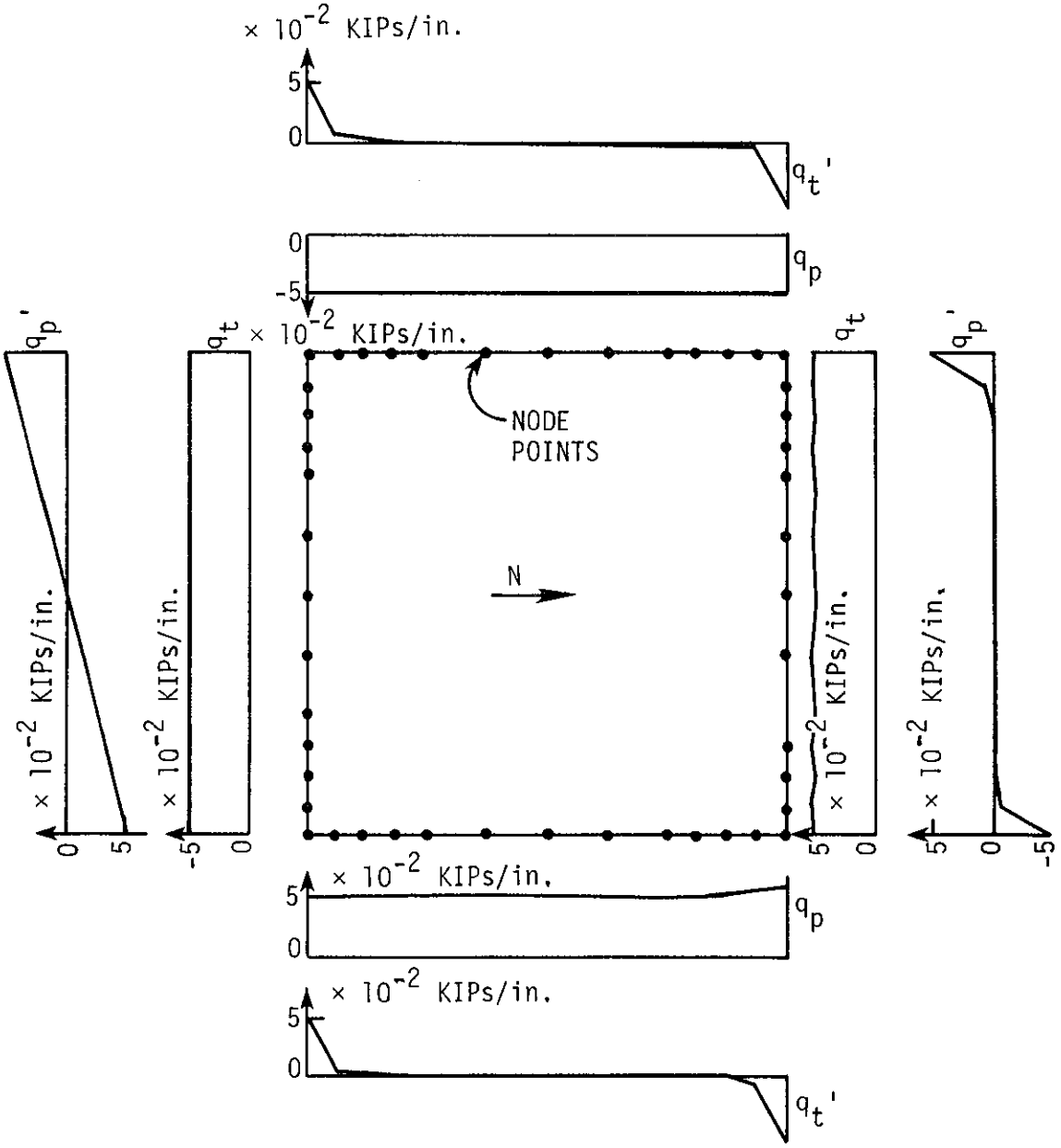

Fig. 56. Edge zone force distribution from finite-element analysis.

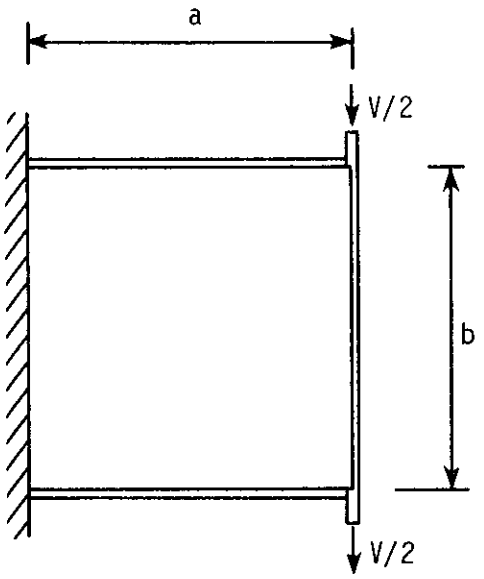

Fig. 57. Cantilever test frame.

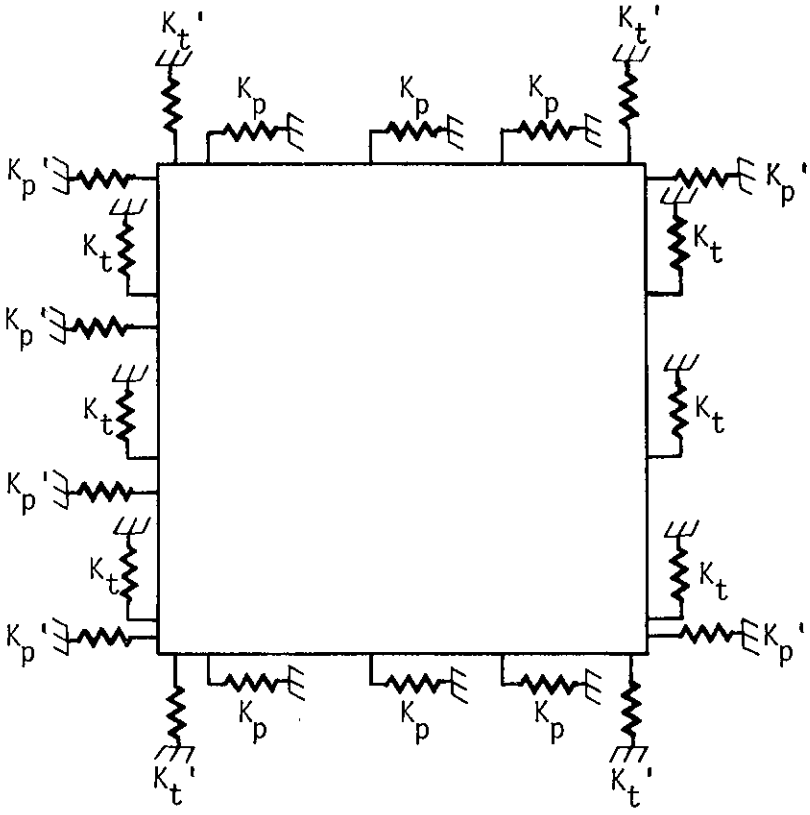

Fig. 58. Idealized spring stiffness of edge zone.

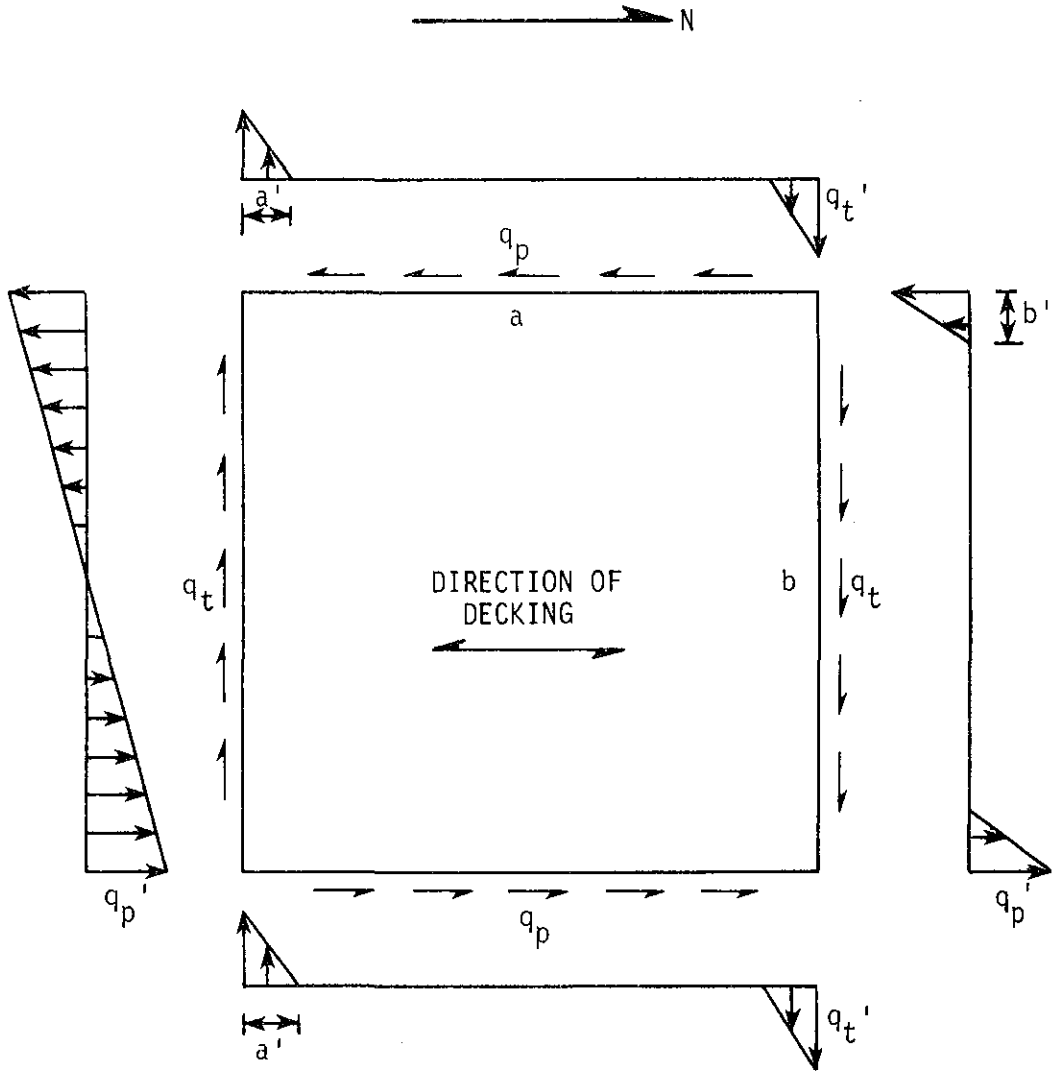

Fig. 59. Interfacial edge zone forces (idealized).

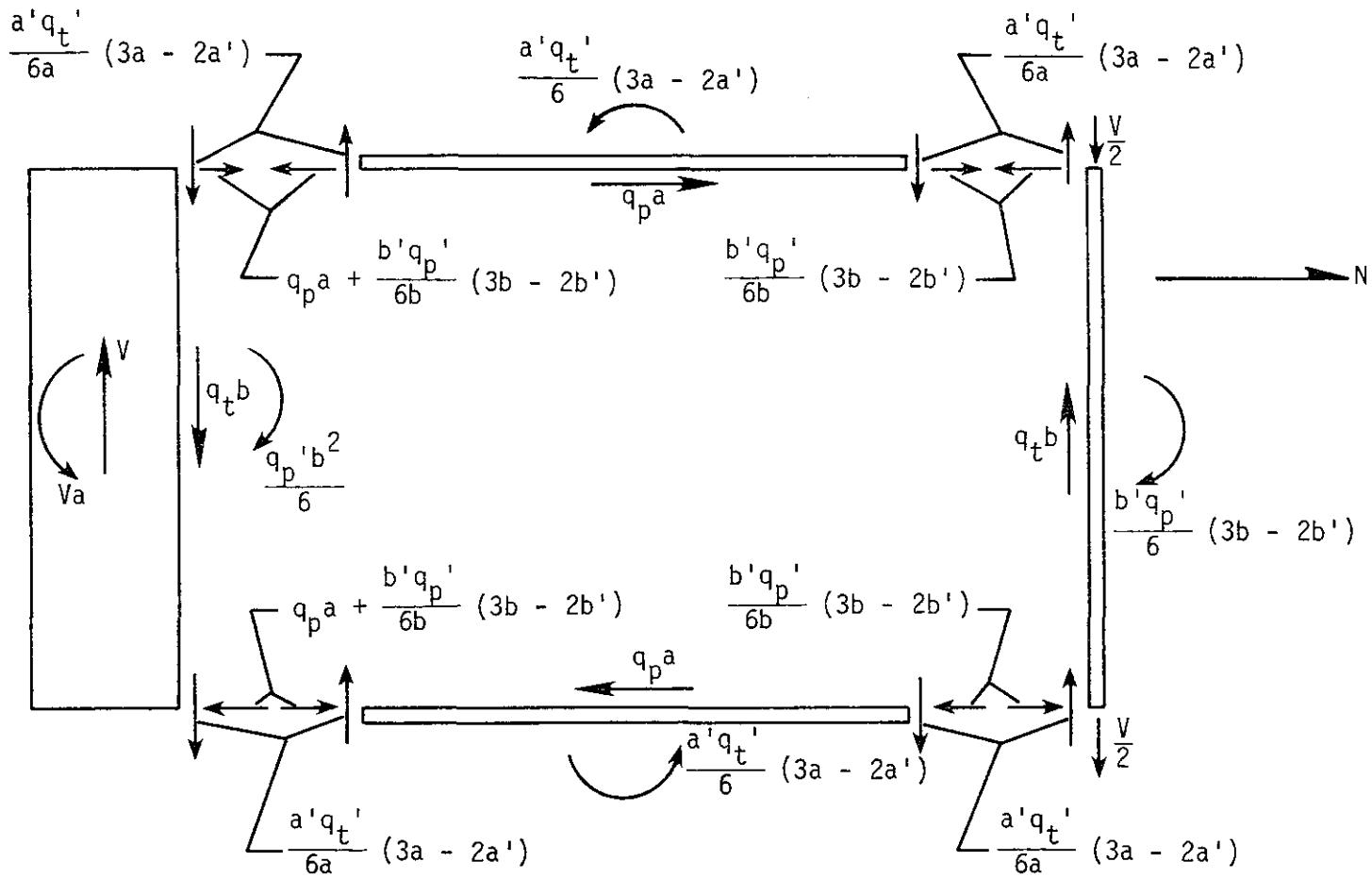

Fig. 60. Framing member forces (linear range).

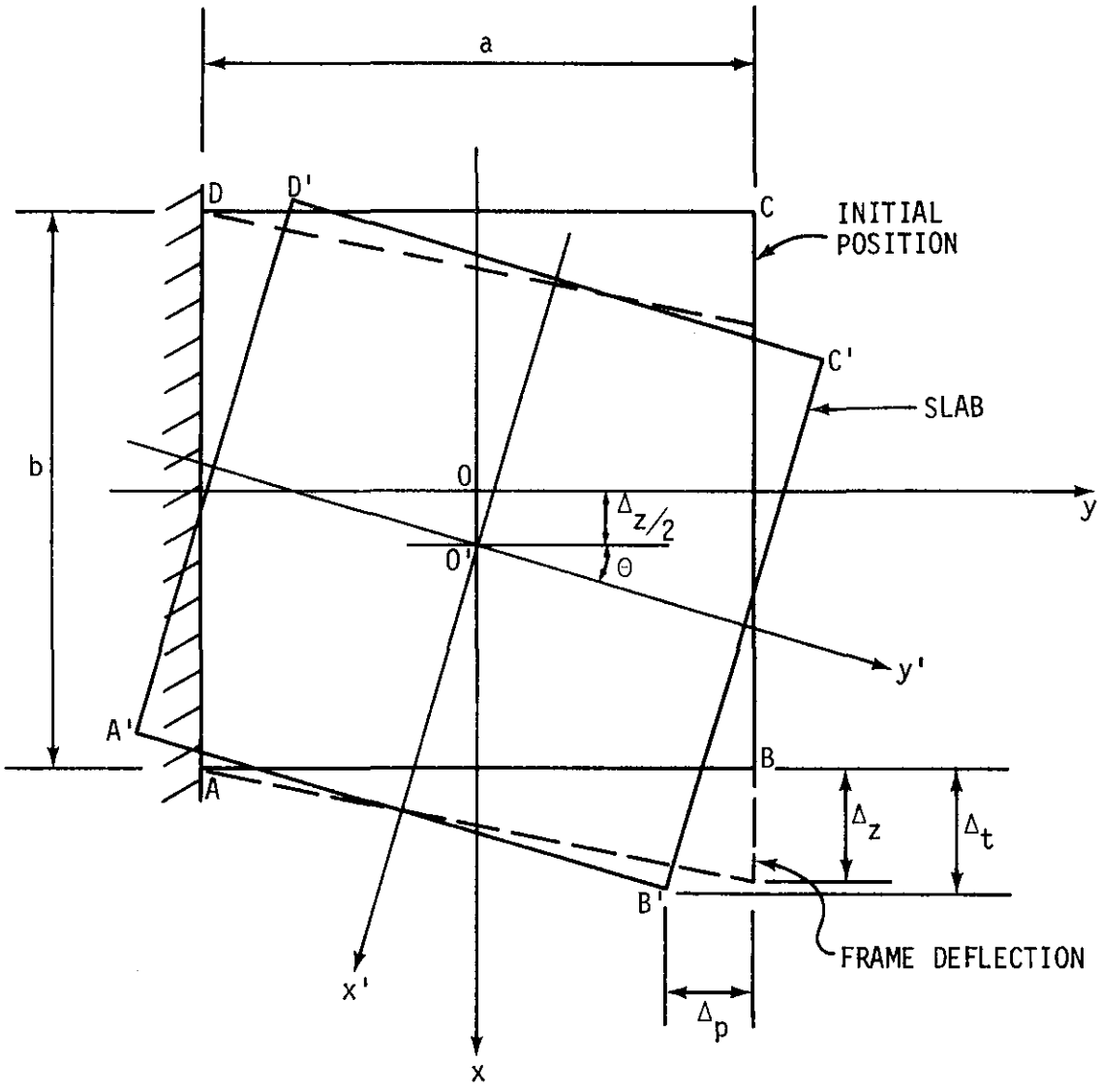

Fig. 61. Displacement of slab with respect to frame.

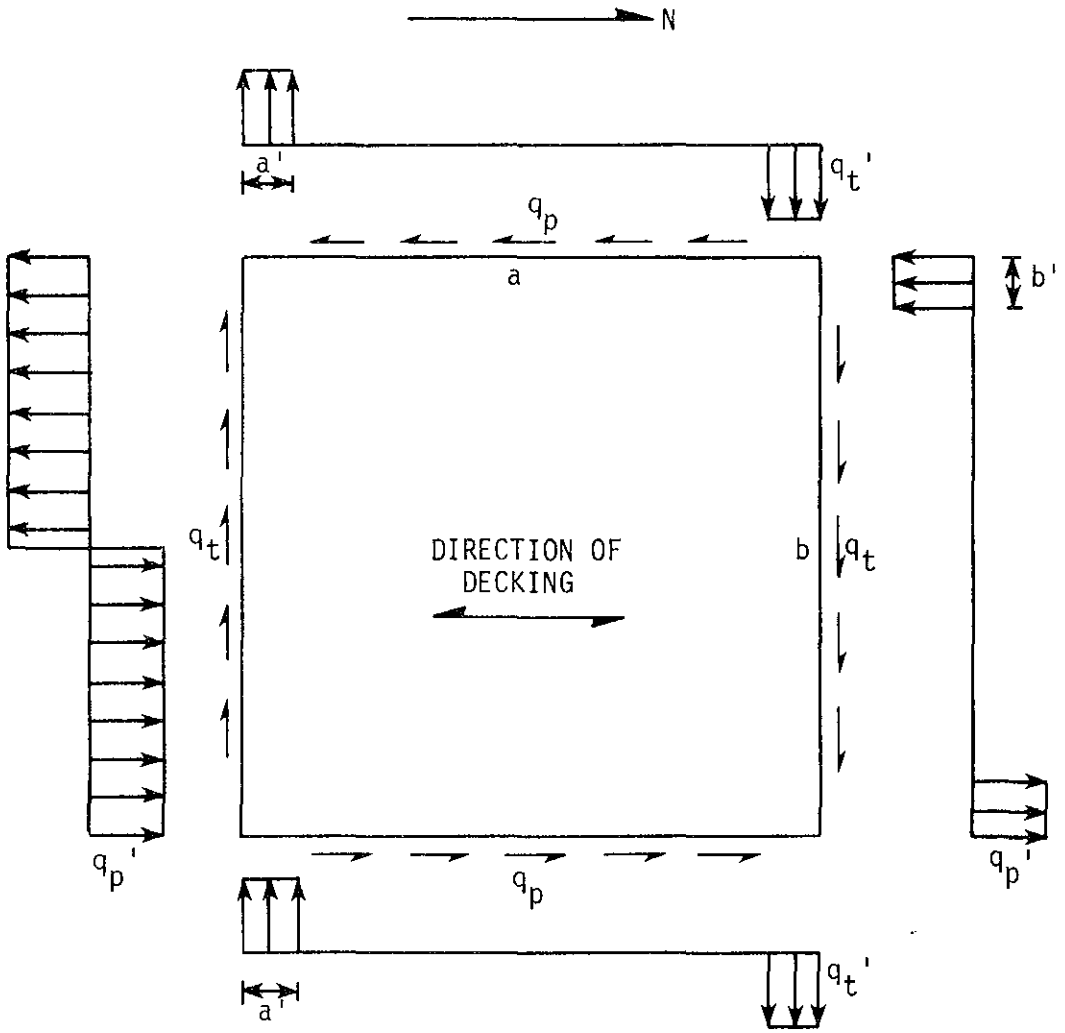

Fig. 62. Assumed edge zone force distribution at ultimate.

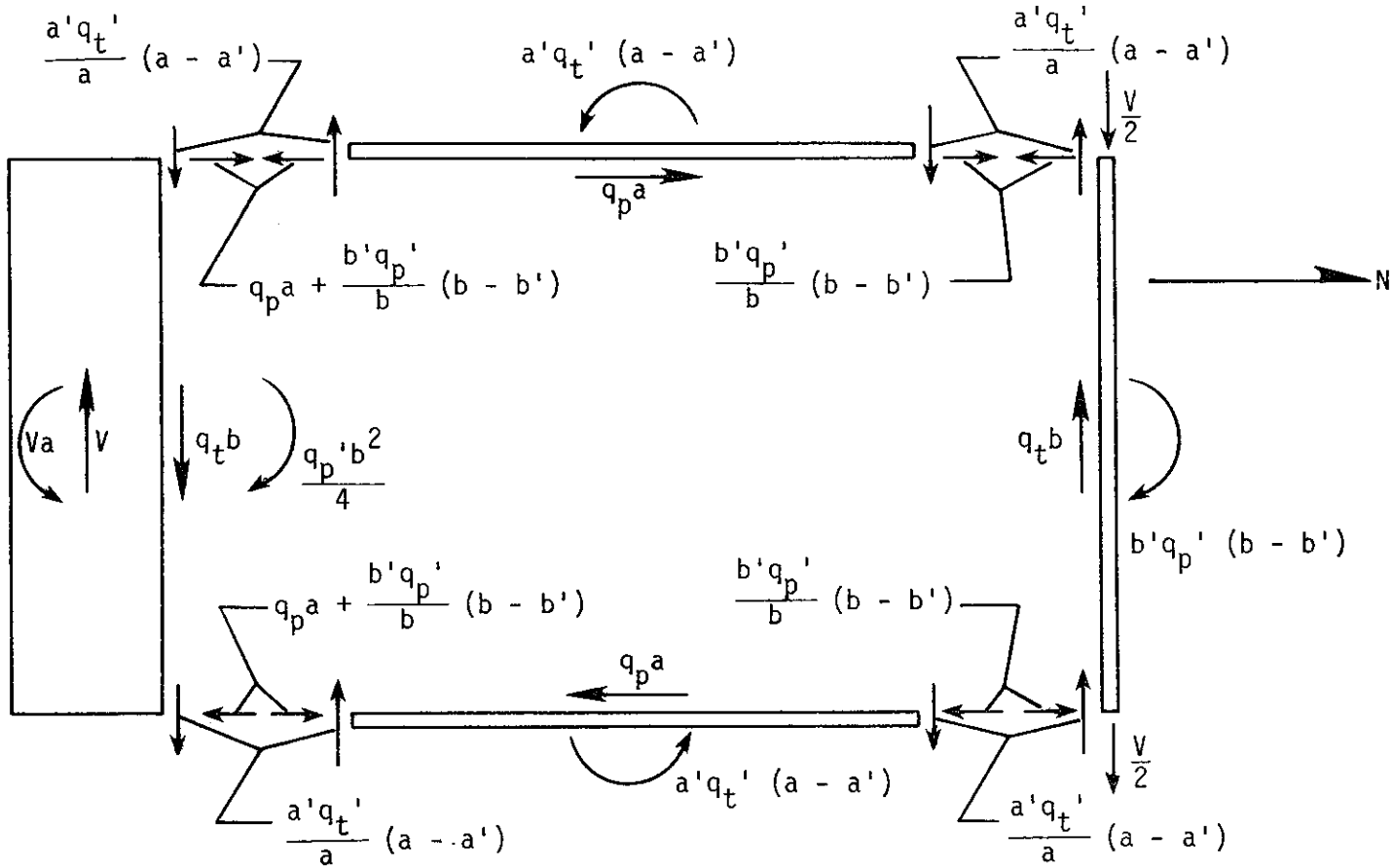

Fig. 63. Forces on framing members at ultimate.

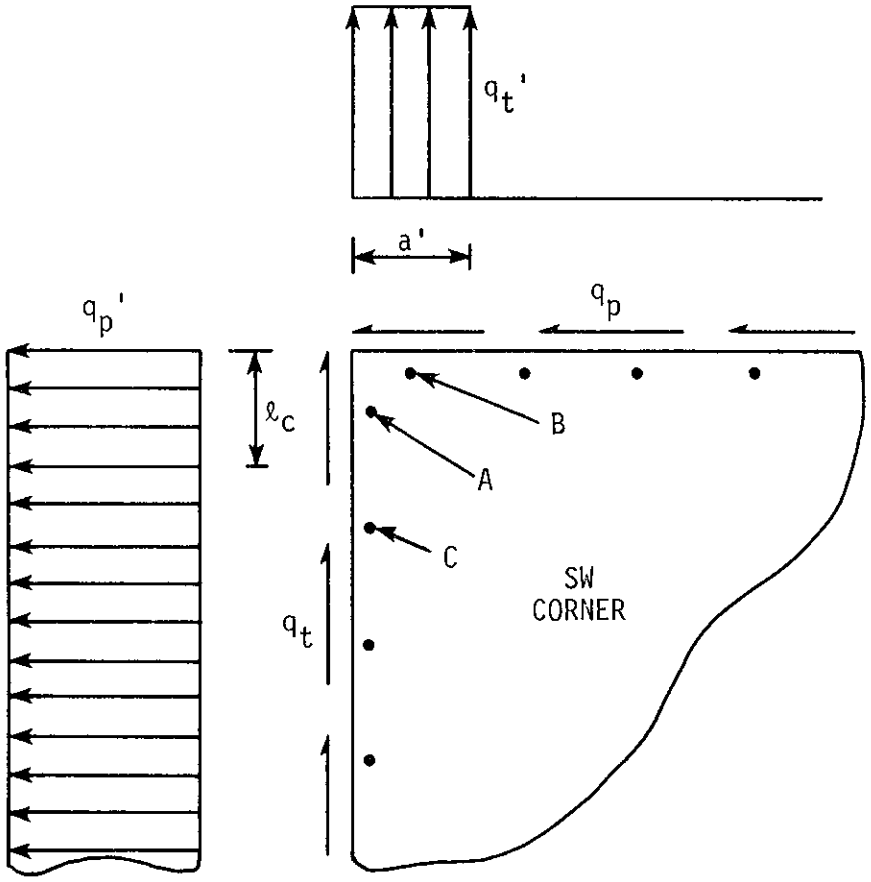

Fig. 64. Assumed forces acting on edge connections at corner of diaphragm.

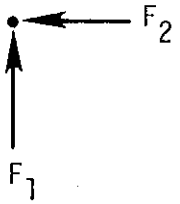

Fig. 65. Component forces acting on typical corner connection "A".

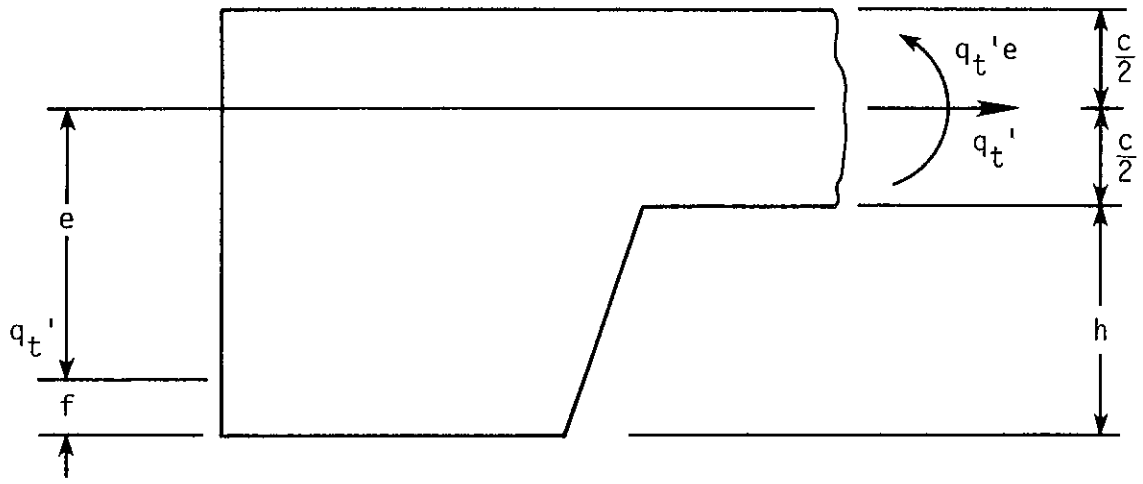

Fig. 66. Force system on cross section of Slab 4 at south edge.

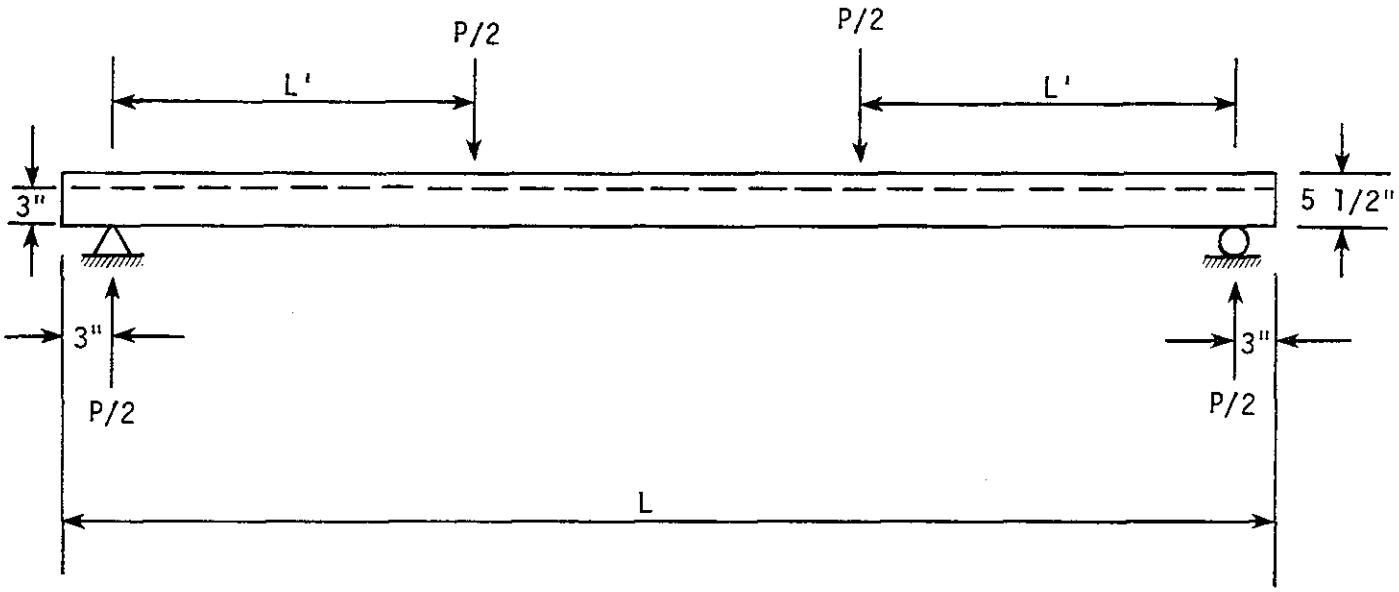

Fig. 67. Schematic of two-point simply supported test specimen.

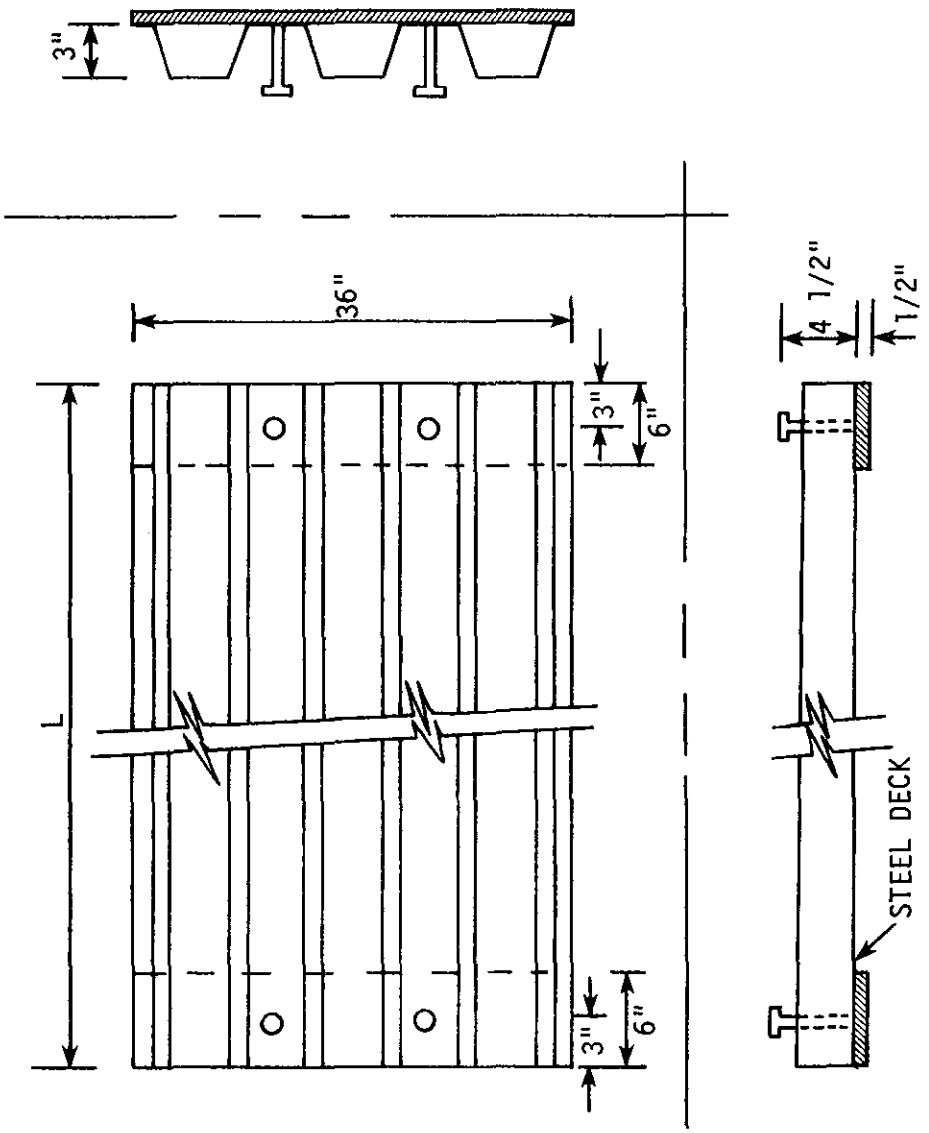

Fig. 68. Studded specimen details prior to casting.

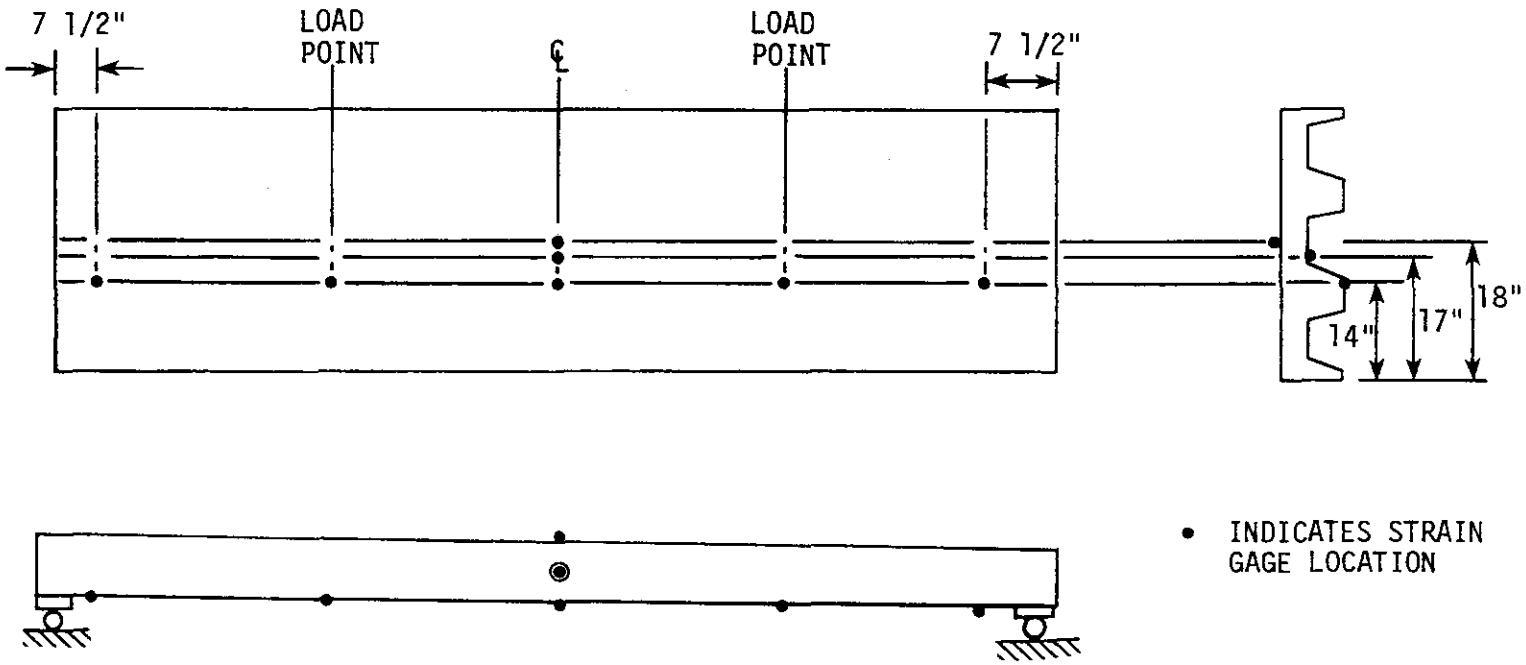

Fig. 69. Strain gage locations.

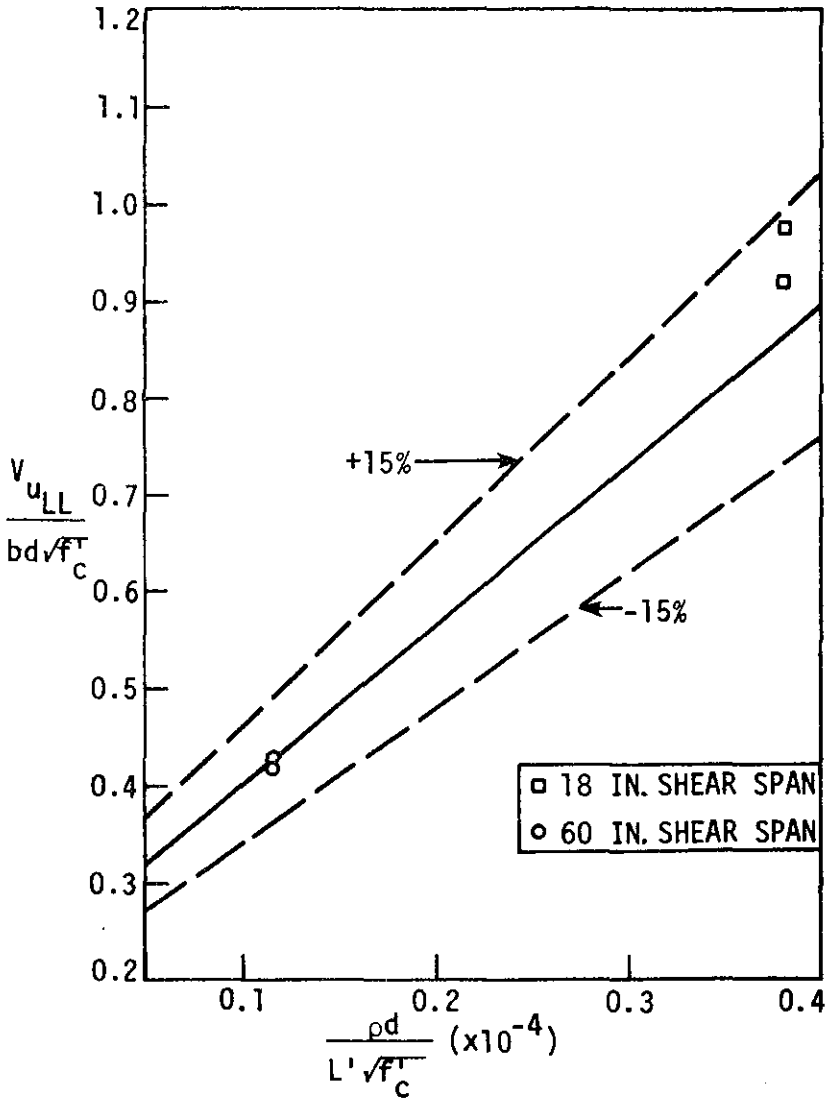

Fig. 70. Nonstudded specimen regression curve, 20-gage.

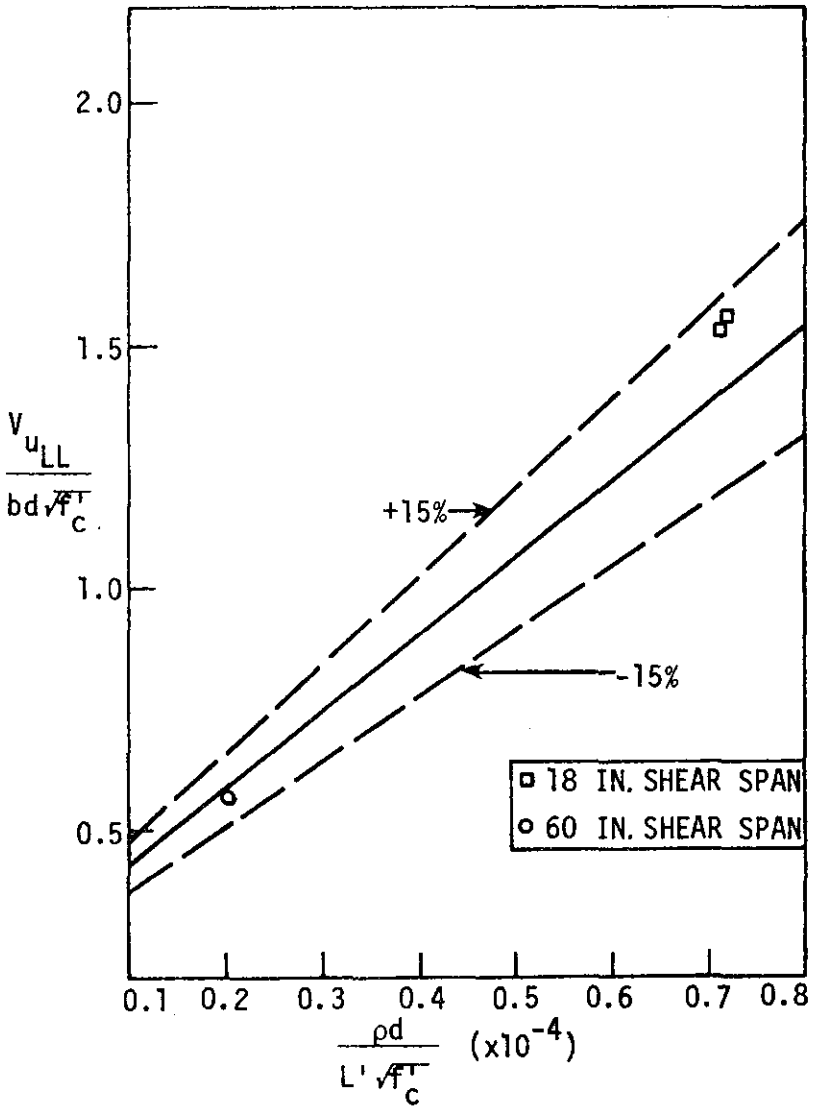

Fig. 71. Nonstudded specimen regression curve, 16-gage.

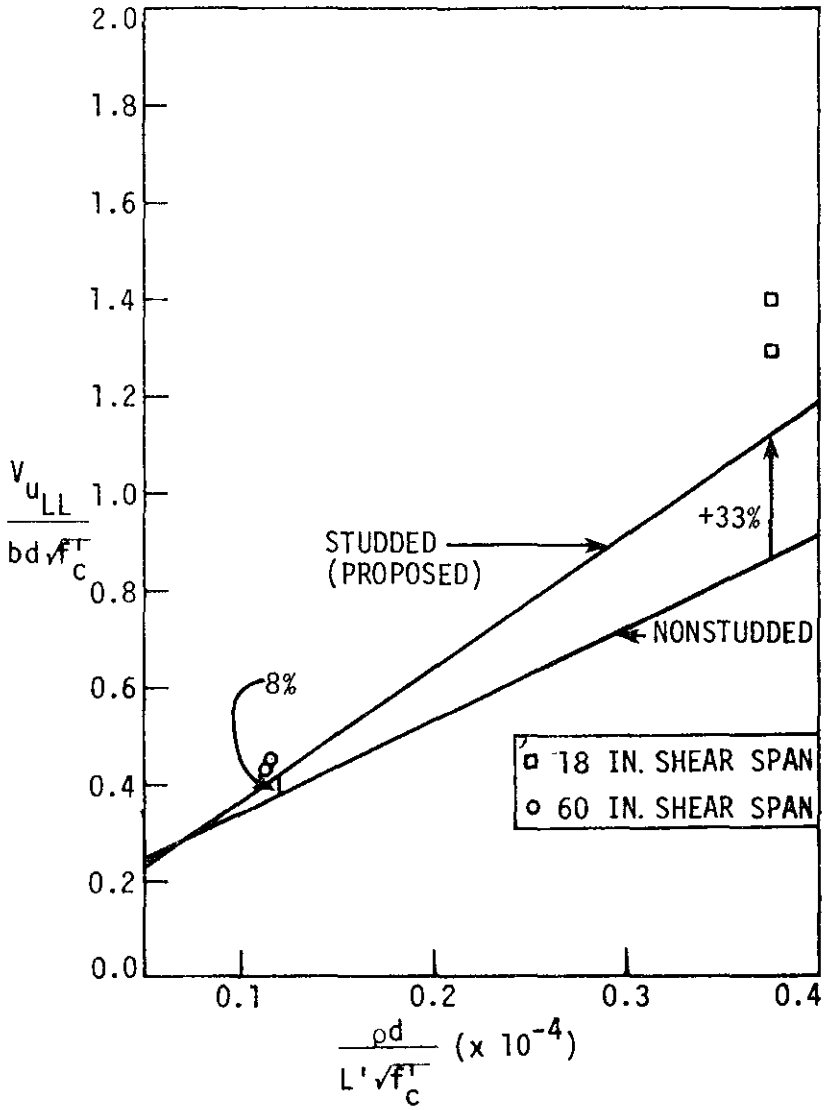

Fig. 72. Proposed studded specimen curve, 20-gage.

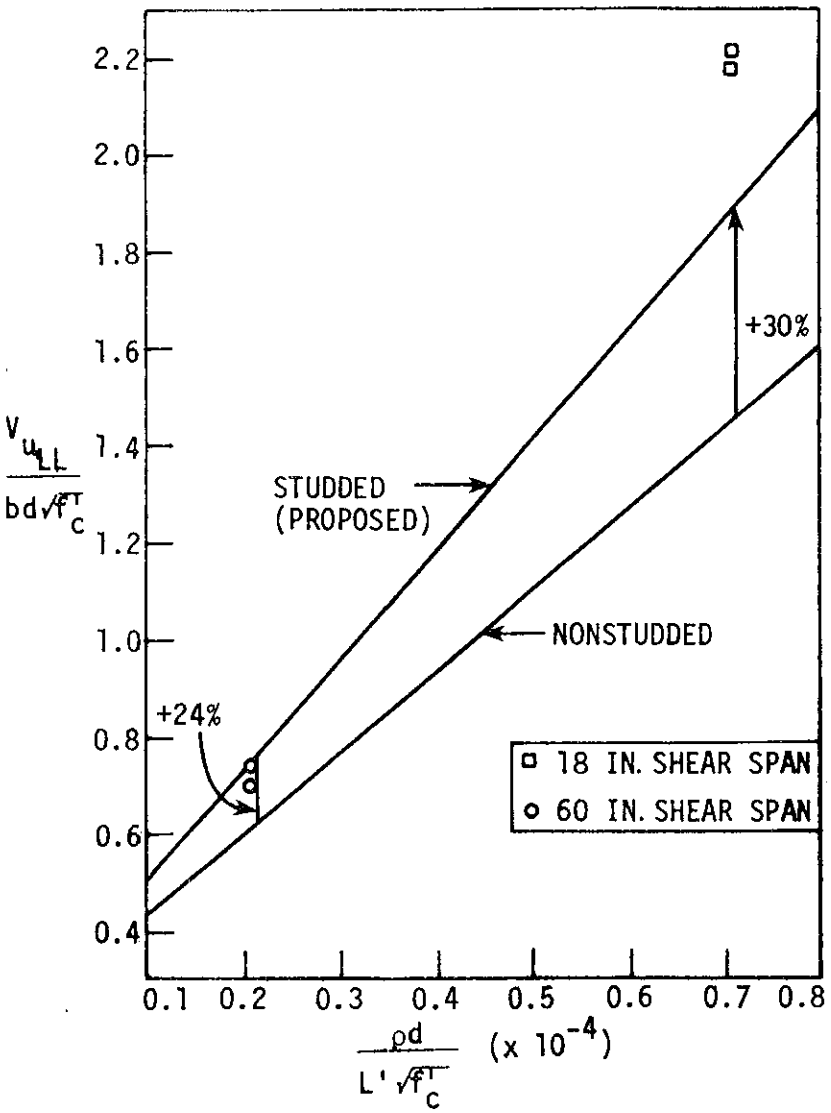

Fig. 73. Proposed studded specimen curve, 16-gage.

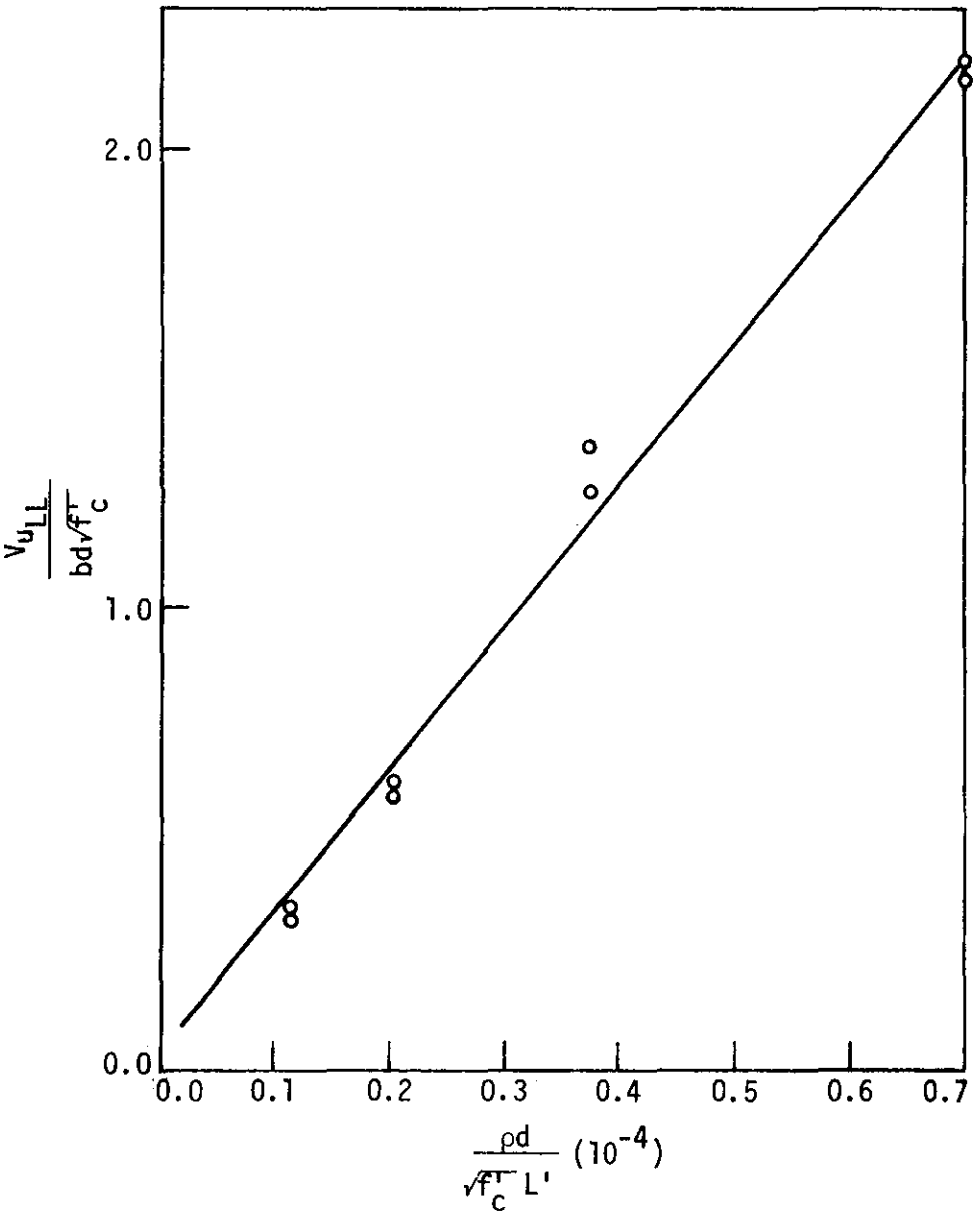

Fig. 74. Plot of studded specimen results, gages combined.

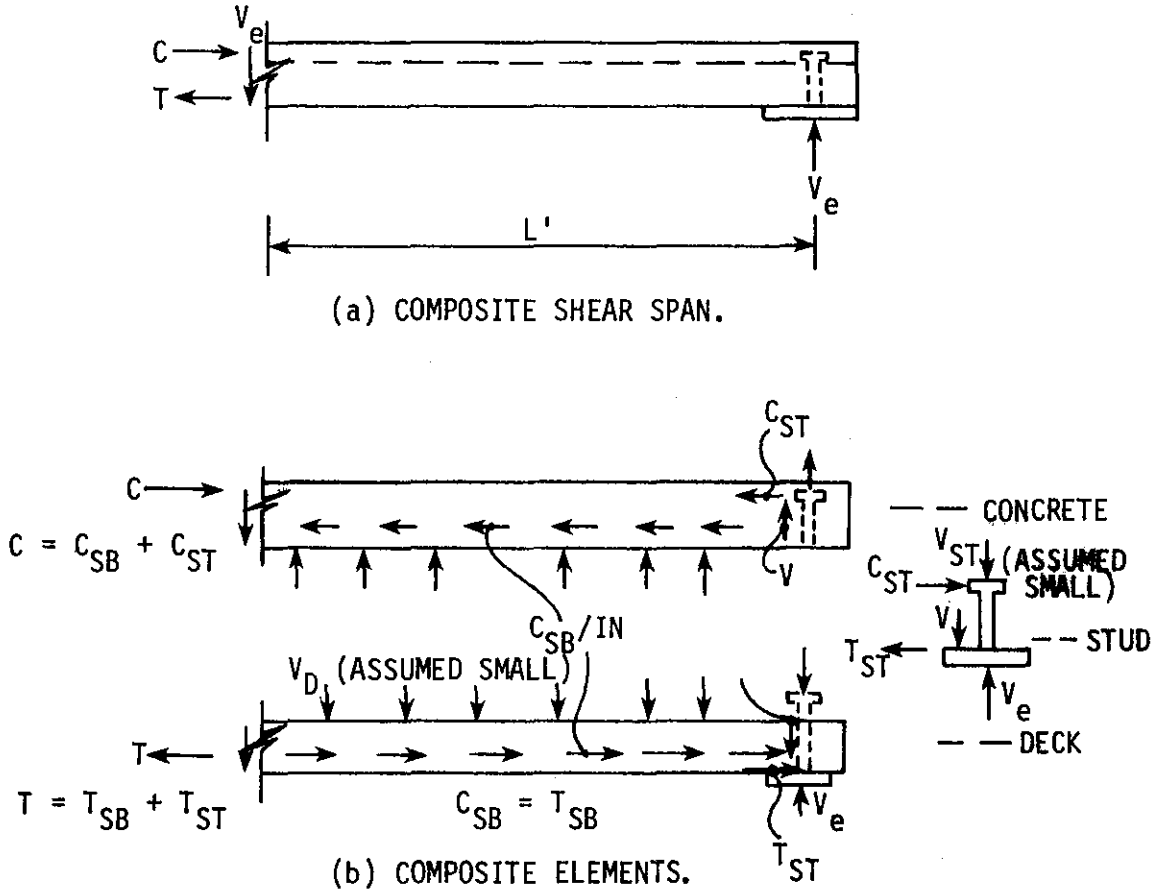

Fig. 75. Forces and displacements for the contributing forces approach.

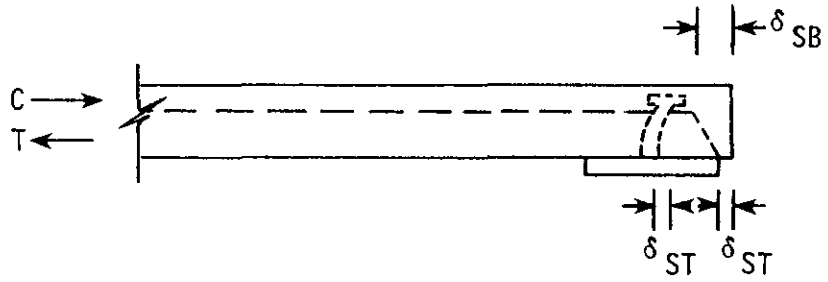

(c) END-SLIP DISPLACEMENTS.

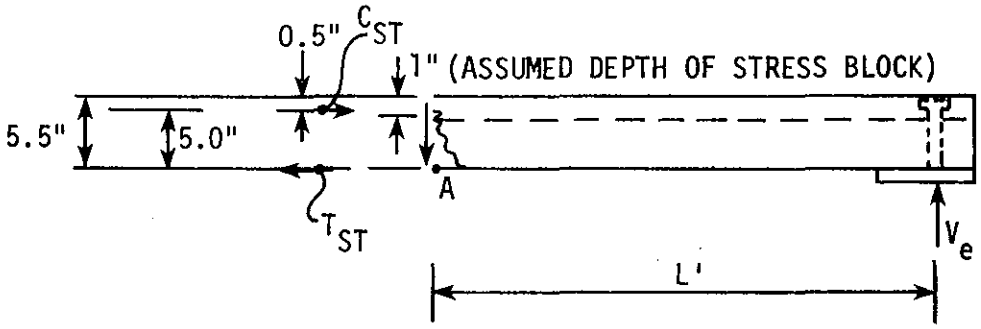

(d) STUD FORCE CONTRIBUTION.

Fig. 75. Continued.

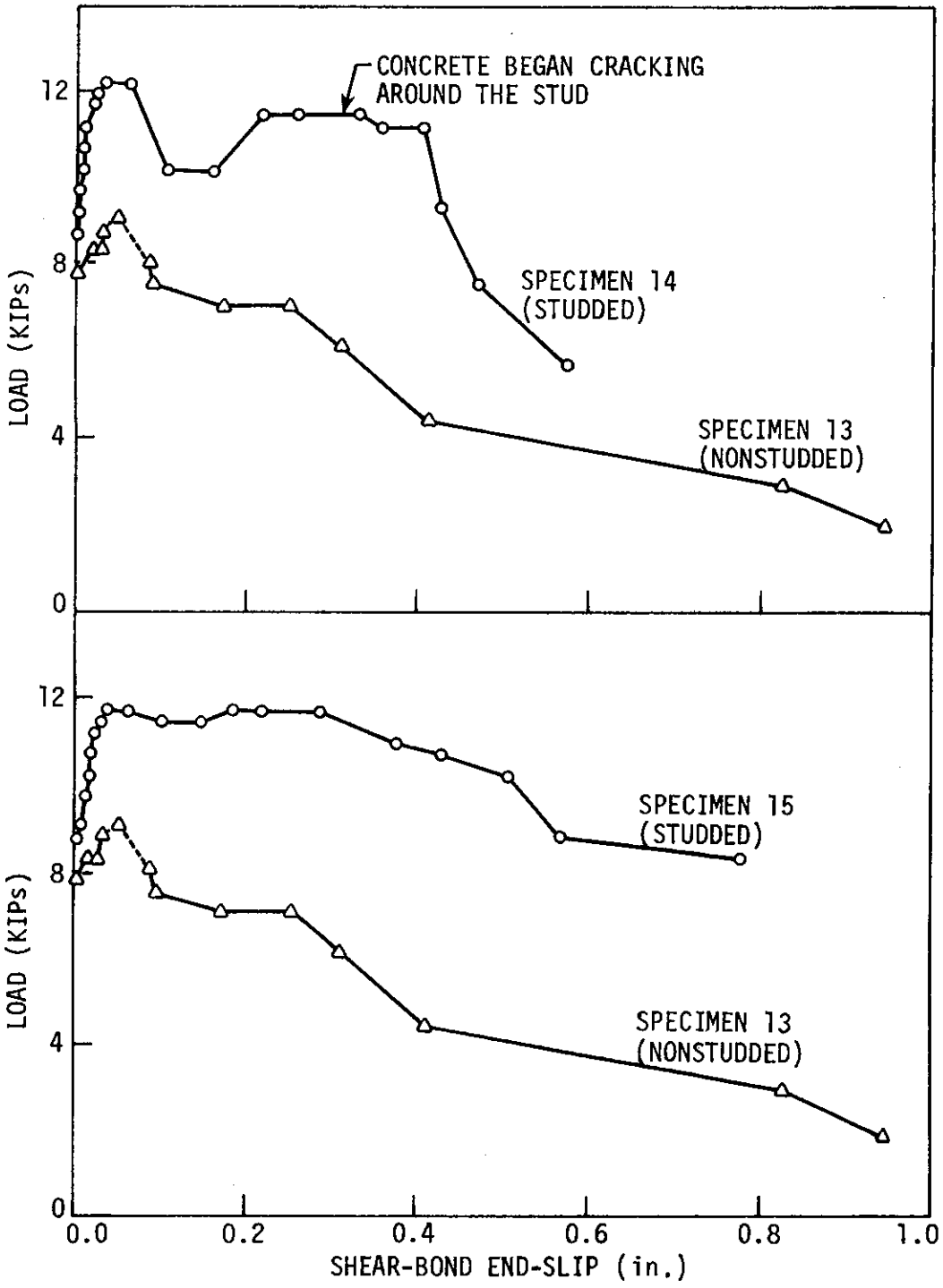

Fig. 76. Load vs. shear-bond end-slip, Group IV.

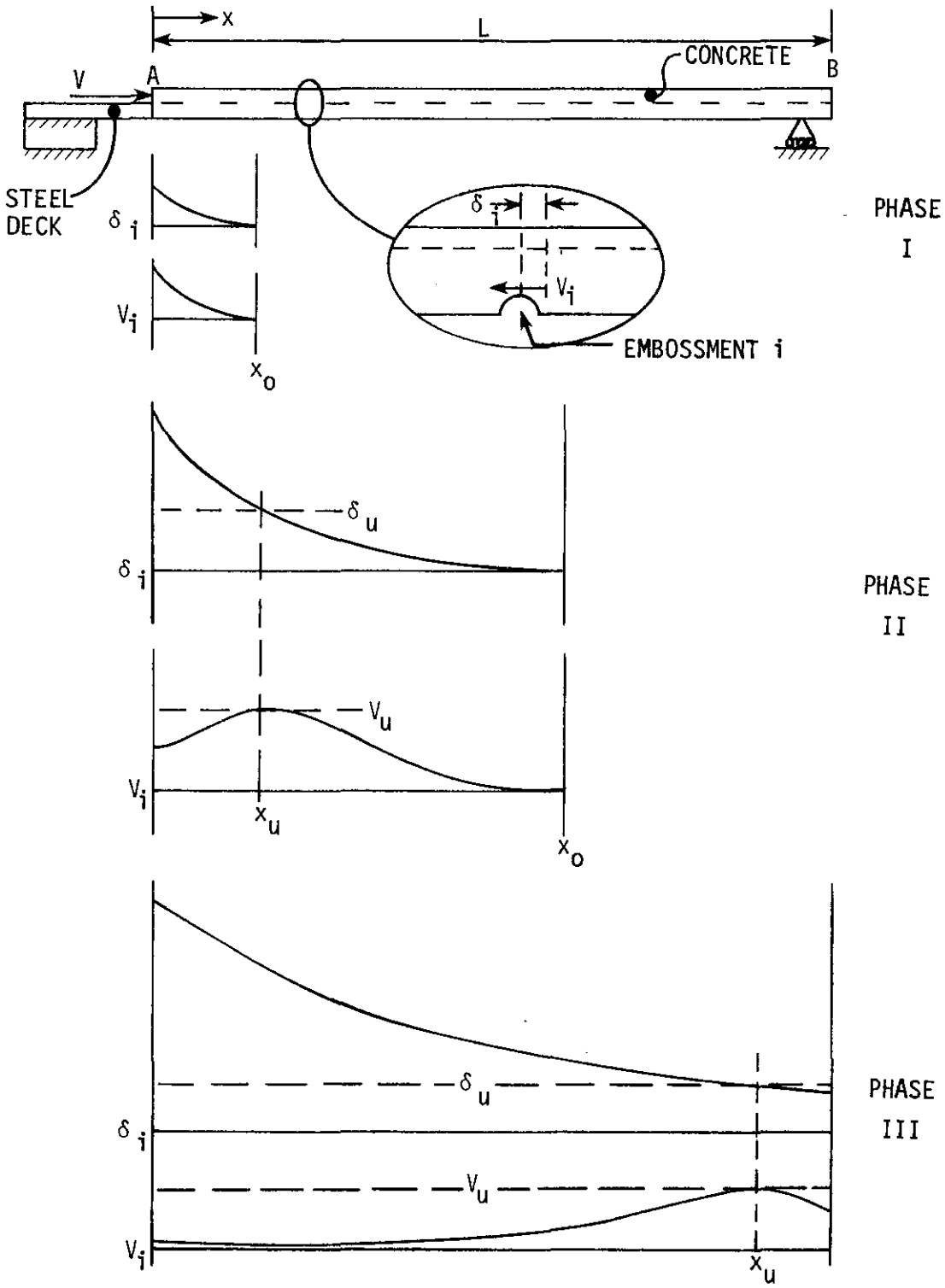

Fig. 77. Schematic of pushout specimen.

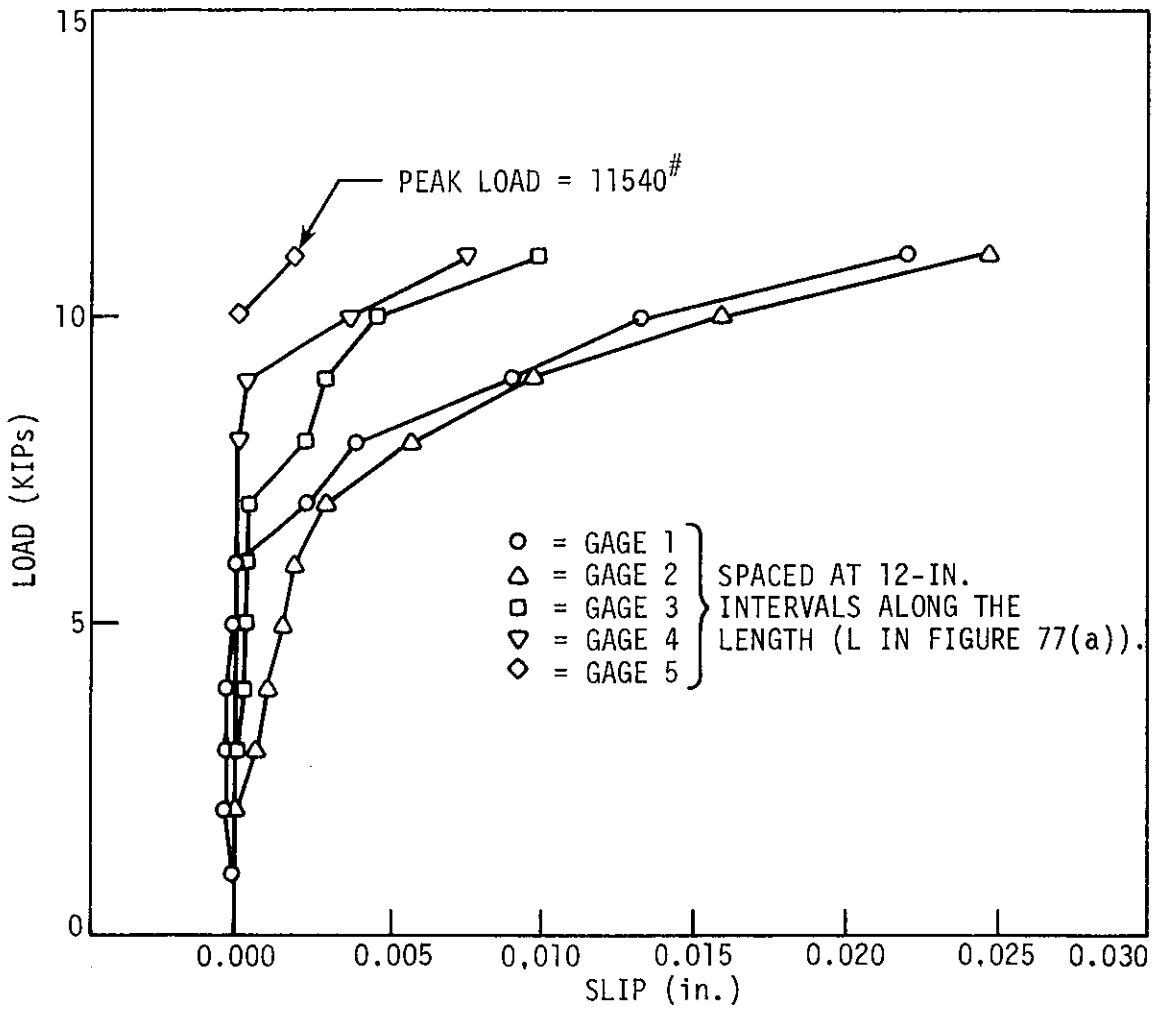

Fig. 78. Typical load vs. deflection curve showing wave propagation.

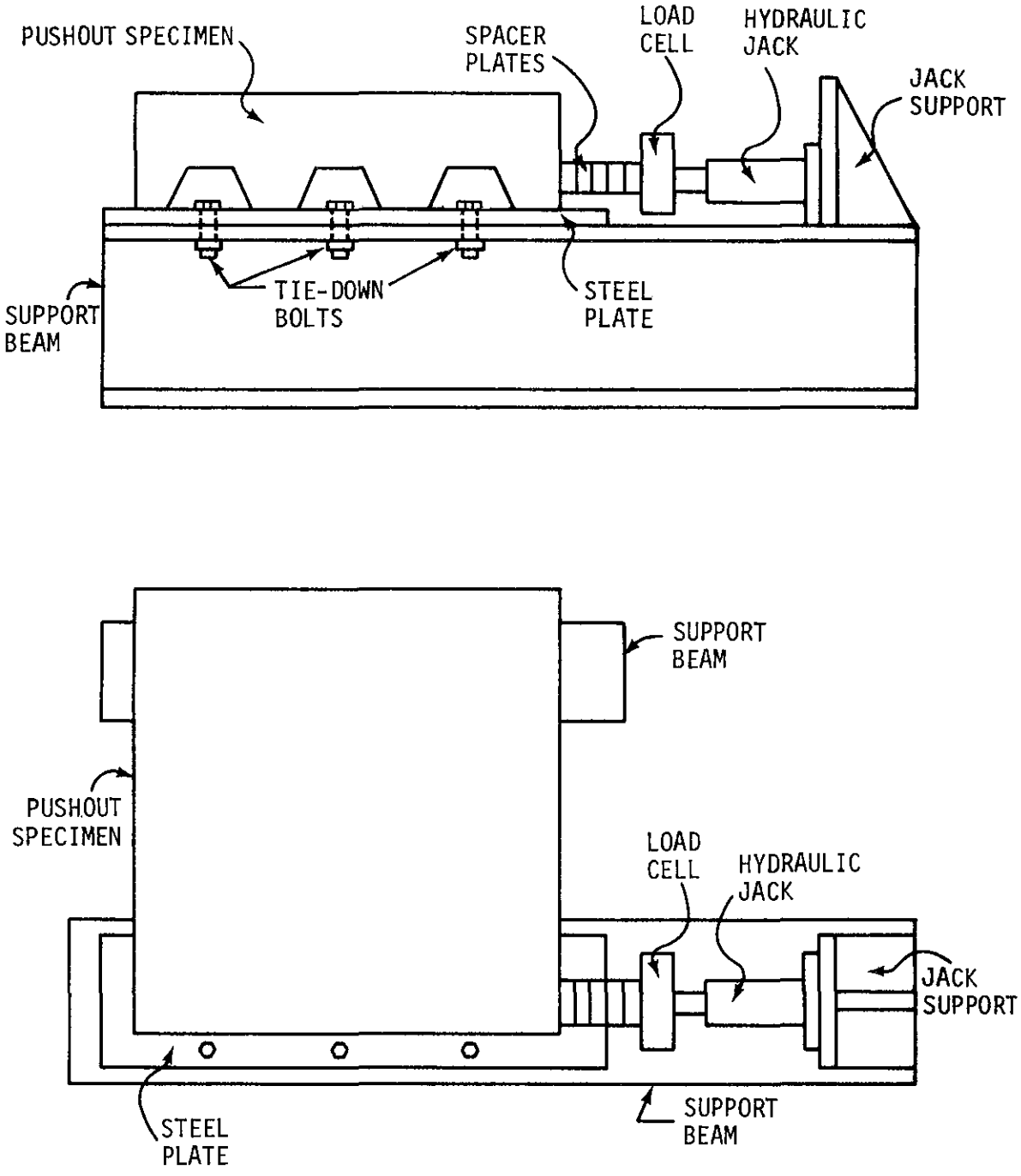

Fig. 79. Schematic of pushout test.